Disorder effects and non-equilibrium dynamics on the electronic orders of strongly correlated materials

A DISSERTATION
SUBMITTED TO THE FACULTY OF THE GRADUATE SCHOOL
OF THE UNIVERSITY OF MINNESOTA
BY

Tianbai Cui

IN PARTIAL FULFILLMENT OF THE REQUIREMENTS
FOR THE DEGREE OF
DOCTOR OF PHILOSOPHY

Rafael M. Fernandes

August, 2019

Acknowledgements

Graduate school is a long journey with a lot of ups and downs. I am fortunate enough to have many remarkable and iridescent people accompany me throughout the journey. Because of their companions, I not only have many priceless memories but also be able to learn from them and improve myself in various perspectives. As I am finishing up the dissertation, I would like to use this opportunity to express my gratitude to them.

First of all, I am deeply grateful to my Ph.D. advisor Dr. Rafael M. Fernandes. He is not only an outstanding physicist, but also a great teacher, a responsible group leader and, more generally speaking, a wonderful person. I am very thankful to have the opportunity to start working with him right after I switched field from electrical engineering to physics. Throughout my Ph.D. study, he always asks me the right questions during our discussions. From answering and sometimes trying to answer those questions, I learned not only a lot of physics but also the thought process of solving difficult problems. All the things I learned from Rafael not only benefits my Ph.D. study and research but also will continue benefiting me for the rest of my life. It is impossible to fit all my gratitude to him in this short paragraph. So, I will just say "thank you very much, Rafael".

I am also very thankful to my M.S. advisor Dr. P. Paul Ruden. His wonderful lectures on semiconductor physics spark my interest in physics. I am very grateful for his kindness and encouragement that allows me to pursue a Ph.D. in physics.

I am grateful to Dr. Jian Kang, Dr. Michael Schütt, Dr. Peter P. Orth, Dr. Xiaoyu Wang and Dr. Morten Christensen for all the valuable help they provided, fruitful discussions and collaborations we had during my Ph.D. research.

Thanks to Morten, Maria, Peter, and Michael for dragging me to the cardio classes and climbing events to help me keep fit and compensate all the delicious pizza, burger,

Korean and Chinese foods we had for lunch every day.

I would like to thank my friends in the physics department, Morten Christensen, Maria N. Gastiasoro, Laura Classen, Ming Li, Yanjun Yang, Mengqun Li, Yuting Wang, Ruiqi Xing, Mengxing Ye, Yuguang Chen, Biqiong Yu, Xuzhe Ying, Fei Chen, Zedong Yang, Xiaojun Fu, Yahor Savich, Yilikal Ayino, Ezra Day-Roberts, Virginia Gali, Thaís V. Trevisan and Vanuildo de Carvalho and many others. Their presence and companion made my life and study in physics more colorful.

I also want to thank Prof. Andrey Chubukov, Prof. Allen Goldman, and Prof. Turan Birol for generously offering their time and efforts to serve on my thesis committee.

Last but not least, I would like to thank my family. I am deeply indebted to my parents, for all their love and support throughout my entire life. I am also profoundly grateful to my long-time friend, my soulmate and now my beloved wife Alison Xiao Chen, for always by my side during this long journey.

This thesis was financially supported by the by U.S. Department of Energy, Office of Science, Basic Energy Sciences, under Award DE-SC0012336. The author acknowledges the support from the Franklin Summer Research Fellowship offered by the School of Physics and Astronomy at the University of Minnesota, the Doctoral Dissertation Fellowship awarded by the University of Minnesota. The author also acknowledges the Minnesota Supercomputing Institute (MSI) at the University of Minnesota, where parts of the numerical calculations were performed.

Dedication

To my parents: Lijuan Yang and Yongzhe Cui, my grandparents: Shuhua Fu and Xianmo Yang, and my beloved wife: Alison Xiao Chen.

Abstract

Strongly correlated materials offer promising prospects for numerous applications, from superconductivity to quantum information processing. The exotic electronic properties arise from the collective behavior due to strong electron-electron correlation. This leads to the complex phase diagram of strongly correlated materials consists of multiple distinct yet intertwined electronic orders, for examples spin density-wave, charge density-wave, nematic order, and superconductivity. Most theoretical studies of this delicate balance between different electronic orders in strongly correlated systems assume disorder is absent and equilibrium is reached, which sometimes makes comparison with experiments challenging. In this thesis, I will surpass these assumptions to show how disorder dramatically changes the way electronic orders develop, and also demonstrate that non-equilibrium perturbations enable us to understand different dynamics in various timescales and to search for new physical behaviors which are absent in equilibrium. In particular, I will discuss the rare region effect in inhomogeneous systems and show how it changes the critical behaviors of nematic and magnetic quantum phase transitions. I will propose a self-consistent perturbative approach to study the dynamics of the superconducting gap at the picosecond time scales after driven out of equilibrium. Using this approach, I will show that the dynamics of the multi-band superconductor is distinct from the single-band conventional superconductors. I will also elaborate on the damping and relaxation effects on the gap dynamics within the electronic system at picosecond time scales.

Contents

List of Figures

Chapter 1

Introduction

1.1 Quantum materials and Quantum phases

Discovered by Joseph Thomson in 1897, the electron is the first well studied subatomic particle to human being. It carries one negative elementary charge (-e), which is approximately 1.6×10^{-19} C, and one half of the intrinsic angular momentum known as spin-$\frac{1}{2}$. These fundamental properties of electron are described by quantum mechanics, the fundamental theory that governs the microscopic world. When a large amount of the electrons is in action, the collective behavior of the electrons can manifest at the macroscopic scales. Conductivity and magnetic properties are two examples of such manifestations. These phenomena can be well understood by the classical theory of electrodynamics and statistical mechanics, despite their quantum mechanical origins. However, when the interaction between electrons is prominent so that they become strongly correlated, novel behaviors and phenomena emerge. An understanding of these novel phenomena usually requires a full quantum mechanical description. Therefore, materials that host strongly correlated electrons are called quantum materials[1, 2, 3].

In quantum materials, due to strong correlation, electrons behave collaboratively, leading to electronic orders beyond the single-particle description. These exotic electronic orders have many potential applications, one of which is the phenomenon of high-temperature superconductivity. However, it is challenging to have a complete understanding of all these exotic orders, as they are also intertwined with each other, giving rise to rather complex phase diagrams[4]. Fig. 1.1 shows the phase diagram of

one iconic family of quantum materials, the cuprate superconductor. As shown in Fig. 1.1, various phases like spin density wave, charge density wave and superconductivity emerge as the temperature or hole doping concentration changes. At zero temperature, thermal fluctuations are suppressed. Therefore, the phase transitions at $T = 0$ are driven solely by the quantum fluctuations, hence the name quantum phase transitions. Although it is not possible to directly observe the phase transition at zero temperature, the existence of a quantum phase transition will leave imprints on the macroscopic thermodynamical properties at finite temperatures. Therefore, in order to decipher the complex phase diagram of quantum materials, it is crucial to understand the nature of the quantum phase transition.

1.2 Vestigial order in quantum materials

Multiple phases appear in the phase diagram of strongly correlated systems, meaning various symmetries can be broken by the collective behavior of the electrons. Electronic orders can also break several symmetries at the same time. For example, the stripe spin density-wave order breaks not only the SU(2) spin rotational symmetry, but also the underlying lattice symmetry. This leads to the concept of vestigial order. When the 'mother' electronic order break multiple symmetries, intermediate state can be achieved by partially melting the 'mother' state so that a subset of the broken symmetries is restored[5, 6]. The classical example of the vestigial order is the nematic order in liquid crystal, which breaks the rotational symmetry. The nematic order in liquid crystal can be achieved by partially "melting" the smectic order that breaks not only the rotational symmetry but also the translational symmetry.

In analogy to liquid crystal, electronic systems can also exhibit such hierarchy of symmetry breaking[7, 8]. As illustrated in Fig. 1.2, in electronic systems, the density of charge or spin can form inhomogeneous and anisotropic structures call density-wave order (e.g. spin density-wave or charge density-wave). By tuning an external parameter, like temperature or the number of electrons, we can completely "melt" the density wave order to enter the isotropic and homogeneous phase (Fig. 2(c)). Interestingly, before totally melting the density-wave order, we can also have an intermediate phase where the density is already homogeneous, but the density fluctuations are anisotropic

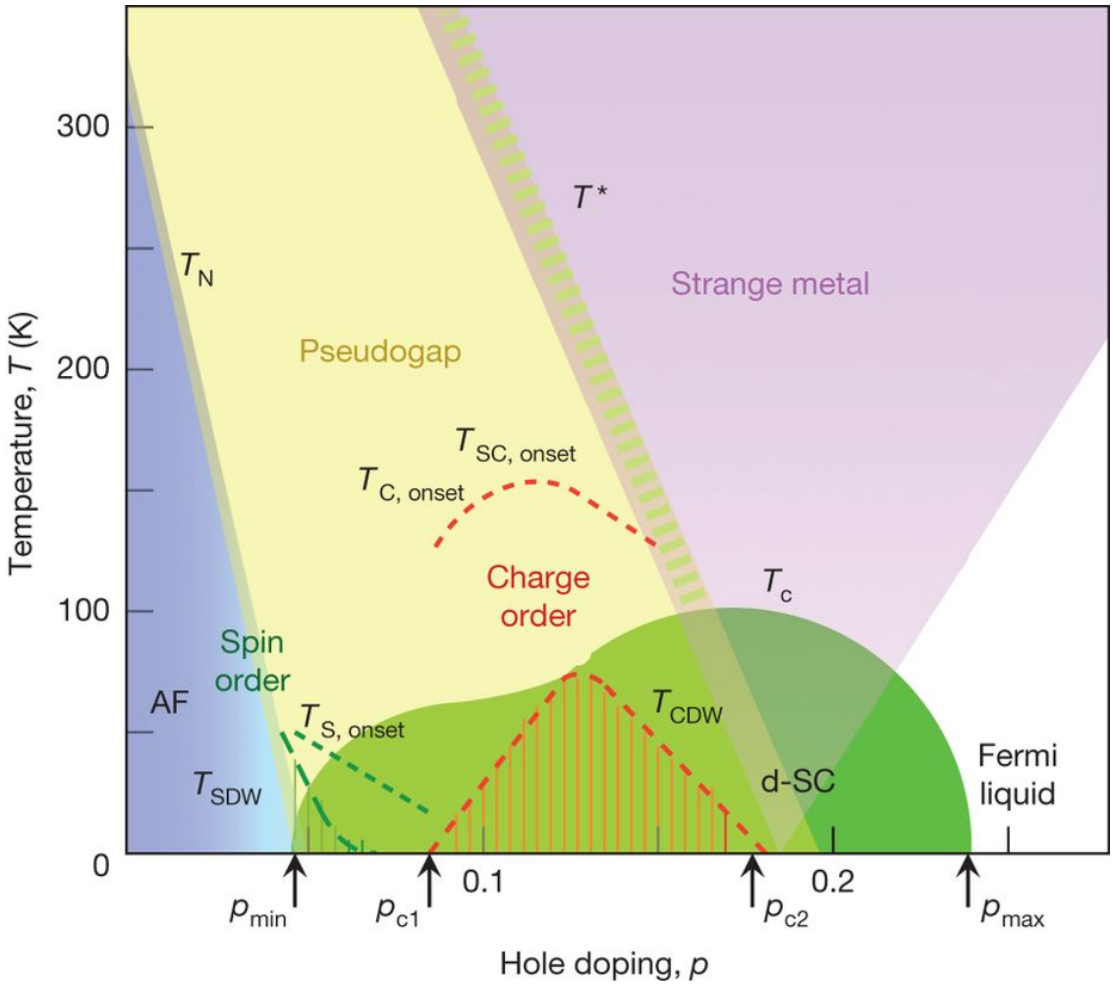

Figure 1.1: Schematic phase diagram of copper oxides taken from Ref. [4]. At low hole doping and below the temperature T_{N}, the system is in the antiferromagnetic Mott insulating state (denoted by AF). Between the doping concentration p_{min} and p_{max}, the d-wave superconducting dome emerges. Within the dome, the charge density wave order and spin-glass type of order can coexist with superconductivity. Above the dome is the pseudogap phase, within which a short range charge order emerges upon cooling. The top right portion of the phase diagram is the mysterious strange metal phase characterized by linear in T dependence resistivity. At the right bottom corner of the phase diagram, the normal Fermi liquid behavior is recovered.

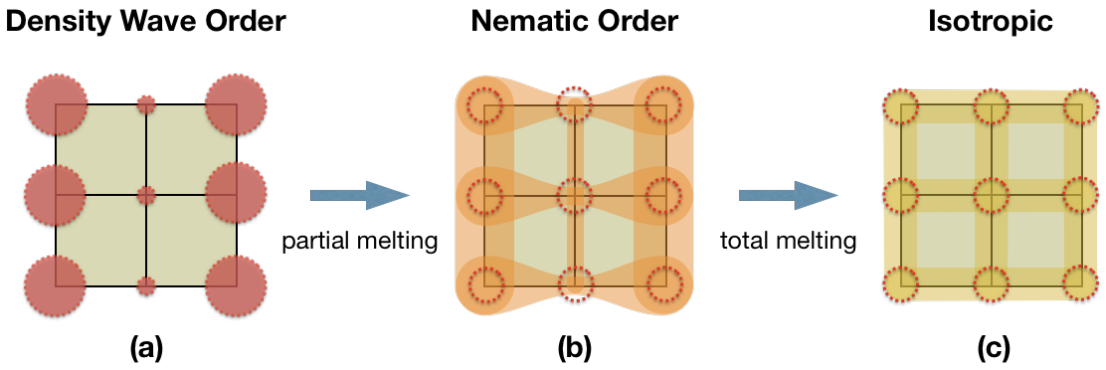

Figure 1.2: Schematics of three possible density-wave patterns in quantum materials. The circles indicate the density profile and the shaded areas indicates the density fluctuations. The density wave order (a) has an anisotropic and inhomogeneous density profile. The nematic order (b) has a homogeneous density profile, but the density fluctuations are anisotropic. In (c), the system is homogeneous and isotropic.

(shown in Fig. 2(b)). This intermediate phase is called the vestigial nematic order[9]. It has been found in many electronic systems, for example in 2 dimensional electron gas under weak magnetic field[10], doped Mott insulators[11], and high-temperature superconductors[12, 13, 14].

1.3 General effects of disorder on phase transitions

In order to understand the electronic properties of quantum materials, it is crucial to understand the phase transitions between electronic states. For clean systems, the general framework to study phase transition is the well-known Ginzburg-Landau theory, which is based on the notion of order parameter and symmetry breaking[15]. Close to the transition, the order parameter is zero in the symmetry preserved phase and non-zero in the symmetry broken phase. The behaviors of the order parameter as well as other thermodynamic observables in the vicinity of the phase transition are called the critical behaviors. If the order parameter changes at the transition in a discontinuous fashion, it is called a first-order phase transition. Otherwise, the phase transition is called continuous (second-order). Since the order parameter is infinitesimal at the continuous phase transition, the correlation length, ξ, of the fluctuation diverges as a power law: $\xi \sim t^{-\nu}$, where t measures the distance to the critical point ($T \propto T - T_c$, where T_c is the

transition point) and ν is the so called critical exponent. All these results are based on the assumption that the system is perfectly clean and free from any disorder. However, in real systems, disorder is not only inevitable but also ubiquitous. In the presence of disorder, the local value of T_c can randomly deviate from its clean value. Therefore, it is crucial to understand whether random disorder changes the critical behavior of the continuous phase transition, since it affects the thermodynamical quantities which can be observed in experiments.

In general, the effects of disorder on the order parameter can be characterized into two types. If the random disorder directly couples to the order parameter, e.g. magnetic impurities, it is called the random-field disorder. If the disorder only couples to the tendency towards the transition, it is called the random-mass (or random-T_c) disorder. Lattice defects like vacancies and dislocations are very common in real systems, which are random-mass type of disorder.

One criterion to determine whether disorder can alter the clean critical behavior is the so-called Harris criterion[16]. The criterion is based on the assumption that disorder is random-mass type and whether disorder present at different locations is uncorrelated. As a result, according to the central limit theorem, the fluctuation of T_c is determined by the size of the region $\delta T_c \sim L^{-d/2}$, where d is the dimensionality of the system. Near the phase transition, the relevant length scale is the correlation length, $\xi \sim (T - T_c)^{-\nu}$. Therefore, the random fluctuation of T_c due to disorder is given by $\delta T_c \sim \xi^{-d/2} \sim (T - T_c)^{d\nu/2}$. If δT_c goes to zero at least not slower than $(T - T_c)$ when approaching the critical point, then the critical behavior is stable against disorder. Since the system is very close to the transition, i.e. $(T - T_c) \ll 1$, the stability condition leads to the following result:

$$\nu \geq \frac{2}{d} \tag{1.1}$$

This inequality is the Harris criterion. The critical behavior of the clean system is stable against disorder if the Harris criterion is satisfied.

However, the Harris criterion is far from the full story of the interplay between disorder and critical behavior of phase transitions[17]. The Harris criterion only considers uncorrelated disorder. But disorder can also have long range correlation. Particularly, for quantum phase transitions, disorders can be perfectly correlated along the imaginary

time axis. For correlated disorders, the presence of large spatial regions that are devoid of disorder (also called rare regions) requires more detailed analysis. Although such regions are statistically rare, their contributions to the thermodynamical observables can be sizable.

The effect of rare regions can be classified based on the comparison between the effective dimension of the rare region, d_{eff}, with the lower critical dimension of the transition, d_c^-. At finite temperatures, the effective dimension of the rare region is determined by the dimensionality of the defect. This is because that point defects can confine all the spatial dimensions, leaving the effective dimension of the rare region to be zero, i.e. $d_{\text{eff}} = 0$. Line defects can only confine $d-1$ dimensions, hence $d_{\text{eff}} = 1$. At $T = 0$, however, the effective dimension of the rare region is increased by the dynamical critical exponent, z[18]. Once d_{eff} is determined, rare region effects can be classified into the following three classes[19]. For Class A, the effective dimension of the rare region is smaller than the critical dimension of the phase transition ($d_{\text{eff}} < d_c^-$). The contribution of the rare region to the thermodynamical quantities increase with region size as a power-law. This cannot the overcome the statistical suppression, which increases with the region size exponentially. As a result, the rare region effect is exponentially small. For Class B, $d_{\text{eff}} = d_c^-$. The rare region's contribution increases exponentially with region size, which cancels the statistical suppression, leading to a strong power-law critical behavior. Finally for Class C, $d_{\text{eff}} > d_c^-$, meaning the long-range order can be established inside the finite size rare regions. After statistical average, rare region effect will smear the otherwise sharpe phase transition. In chapter 2, we will discuss in detail about how quench disorders form the rare region and have a dramatic effect on the Ising nematic quantum phase transitions.

1.4 New phases out of equilibrium

Under the framework of Ginzburg-Landau theory, the phase diagram (e.g. Fig. 1.1) can be understood as the landscape of the minimum of the free energy. Upon changing the tuning parameter of the free energy, for example temperature or chemical doping, the free energy landscape changes, leading to a phase transition. During the transition, the system remains in the minimum of the free energy. What changes is the minimum

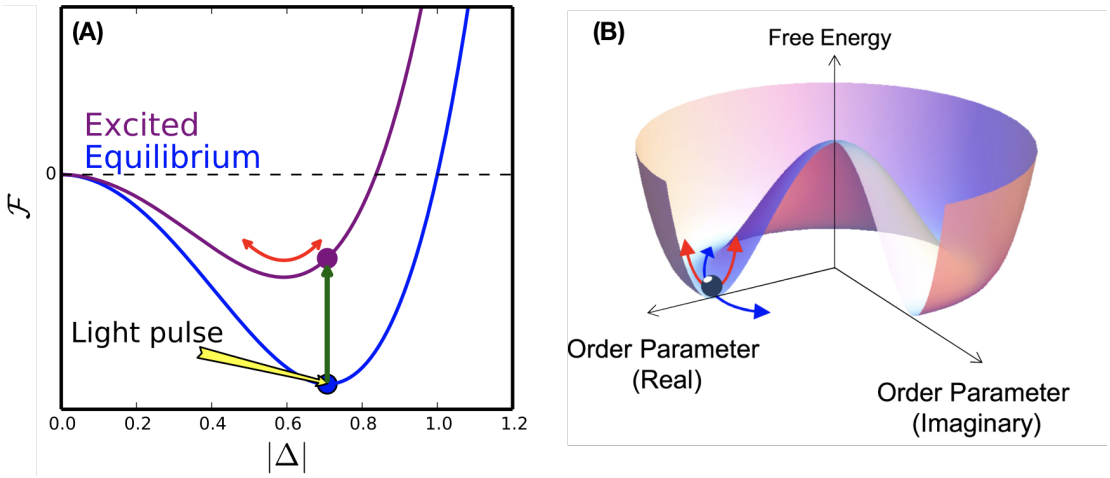

Figure 1.3: The schematic free energy landscape, $\mathcal{F}$, in and out of equilibrium as a function of the order parameter, $|\Delta|$. For superconductors, Δ is the superconducting gap. Panel (A) is taken from Ref. [21]. At equilibrium, the order parameter is in the minimum of the free energy. After driven to non-equilibrium state by an external light pulse, the system is in the excited higher energy state and the order parameter no longer sits at the free energy minimum. Panel (B) is taken from Ref. [22]. In the ordered phase, the complex order parameter can have amplitude fluctuations and phase fluctuations.

itself that evolves to a different location in the hyperparameter space. As shown in Fig. 1.1, the landscape of the free energy minimum can already host many different phases. But what happens outside the free energy minimum is also worth exploring. In order to do that, we need to drive the system out of equilibrium by applying external perturbations to the system, for example, using light pulses as shown in Fig. 1.3(A)[20]. In non-equilibrium, the system is in the excited state with higher energy. This makes it possible to study new physics which is absent in the equilibrium states.

After driven out of equilibrium, it is important to study how the system will relax back to thermal equilibrium. However, in non-equilibrium, the system contains many high energy degrees of freedoms with complex interaction between them, which make it a daunting task of keep track on their time evolutions. Fortunately, the degrees of freedom are separable by their different typical dynamical time scales. For example, the typical relaxation time due to electron-phonon interaction is on the order of nanosecond while relaxations due to electron-electron interaction is on the order of picosecond.

Therefore, different stages of non-equilibrium are characterized by different types of degrees of freedoms. For example, as shown in Fig. 1.3(B), at the correct time scale, we can focus on the dynamics of the order parameter because contributions from other degrees of freedom are negligible. Recent advances in the ultra-fast laser techniques make it possible to conduct pump-and-probe experiments at femtosecond time scale. Therefore, by using a laser at THz domain, the dynamics of the electronic order parameter, e.g. the superconducting gap, can be measured experimentally. Even for such relatively simple subsystem, its non-equilibrium dynamics is still very rich. The system can have completely different dynamical behaviors depending on how far it is driven from equilibrium. Even new phases can emerge in non-equilibrium. One example is the gapless superconducting state in the quench dynamics in picosecond time scales[23]. We will discuss in detail about the different dynamical behaviors of superconductivity from Chapter 3 to Chapter 5.

1.5 Overview

My thesis work is part of the quest of understanding the complex phase diagrams of quantum materials. In particular, my studies focused on the effects of disorder and non-equilibrium perturbations on the electronic orders of quantum materials.

In Chapter 2, I will discuss the rare region effects on the Ising-nematic quantum phase transitions in inhomogeneous systems. I will first introduce the Ising-nematic quantum phase transitions in clean systems and the corresponding low-energy model using the Landau-Ginzburg-Wilson approach. The large-N solution of the low-energy model shows, that a for clean system, the Ising-nematic quantum phase transition happens simultaneously with its "mother" density-wave transition and is first-order. Then, I will discuss the large-N solution inside a single finite size droplet and show that the Ising-nematic quantum phase transition happens separately from the density-wave transition. Furthermore, if the size of the droplet is of moderate size, the Ising-nematic quantum phase transition can be continuous, in contrast to its clean limit counterpart. After averaging over all droplets, I will show the emergence of a smeared nematic quantum phase transition in inhomogeneous systems and discuss the implications on the corresponding experimental results. This work was published in Ref. [24].

In Chapter 3, 4, 5, I will focus on transient dynamics of superconductors after driven out of equilibrium. Chapter 3 will focus on the conventional single-band superconductors, where the gap oscillates with a frequency that is two times its long time asymptotic value with $t^{-1/2}$ damping at the weakly perturbed regime[25, 26, 23]. I will first introduce the quench dynamics of superconductivity and establish the formalism. Then I will discuss the integrability of the model and the exact solution for the dynamics for arbitrary perturbation strengths[27, 26, 23, 28]. Finally, I will prepose a self-consistent perturbative approach to solve the dynamics in the long-time limit and validate it by comparing with the exact solution[29].

In Chapter 4, I will generalize the perturbative approach that I introduce in Chapter 3 to solve the dynamics of multi-band superconductors. First, I will discuss some of the equilibrium properties of multi-band superconductors and then derive the equations of motion governing the dynamics of non-equilibrium superconductivity. I will then show the numerical simulation on the superconducting gap oscillations and highlight the differences to the single-band case. After that, I will apply the perturbative approach to analyze the long-time dynamics of the superconducting gap and derive a closed form of the asymptotic behavior. Finally, I will provide the concluding remarks on the approach we develop and the distinct dynamics that appears in multi-band superconductors. This work was submitted to Physical Review B, which is also available on arXiv:1908.06125[29].

In Chapter 5, I will discuss recent results from THz pump-probe experiments on the gap dynamics of NbN and Nb_3Sn thin films. I will introduce the theoretical framework that incorporates damping effects in the time evolution of the gap in the picosecond time scales. After a detailed analysis of the model, I will apply it to explain the experimental results on the dynamics of the superconducting gap. I will show that the model is applicable to different experiments with different pump pulse profiles and shed light on the relevance of different types of relaxation and damping processes in non-equilibrium superconductivity. This work is published in Ref. [30]

In Chapter 6, I will give the conclusions of the thesis.

Various technical details will be provided in the Appendices which appear after the References.

Chapter 2

Smeared nematic quantum phase transitions due to rare-region effects in inhomogeneous systems

This chapter reproduces content published in Physical Review B in the article "Smeared nematic quantum phase transitions due to rare-region effects in inhomogeneous systems", Tianbai Cui and Rafael M. Fernandes, Phys. Rev. B **98**, 085117 (2018), ©2018 American Physical Society.

2.1 Introduction

In an electronic nematic phase, the crystalline point group symmetry is lowered by electronic degrees of freedom [31, 32, 8]. In analogy to liquid crystals, it can arise via the partial melting of a translational symmetry-breaking smectic phase, which in electronic systems corresponds to a spin or charge density-wave (DW). In several materials, the DW can have multiple wave-vectors $\mathbf{Q}$ related by the symmetries of the underlying lattice. A well known example is a DW on a square lattice with possible ordering vectors $(Q, 0)$ and $(0, Q)$, related by tetragonal symmetry. In these cases, upon melting the DW, the system may form a vestigial Ising-nematic phase in which the translational symmetry of the lattice is preserved, but its rotational symmetry is broken. In the above

example on the square lattice, the nematic transition lowers the tetragonal symmetry down to orthorhombic.

Such a mechanism for electronic nematicity has been proposed in both iron-based superconductors [13, 12, 14], in which the DW is in the spin channel, and in the high-T_c cuprates [31, 33, 34, 35], where the DW can be in both spin and charge channels. Interestingly, both materials at optimal doping exhibit behavior characteristic of a quantum critical point, such as strange metalicity and enhancement of the quasiparticle effective mass [36, 37, 38]. This has motivated deeper investigations of quantum nematic phase transitions in metals, in order to elucidate whether a putative nematic quantum critical point is a key ingredient of the phase diagrams of these superconducting compounds [39].

Several theoretical works have shown that, for a perfectly clean quasi-two-dimensional metallic system, the vestigial Ising-nematic order and the mother density-wave order undergo a simultaneous $T = 0$ first-order transition, implying the inexistence of a quantum critical point [40, 41, 42, 14]. However, disorder, ubiquitously present in realistic systems, can have dramatic effects on quantum phase transitions [43, 44, 45, 46, 47, 48, 49, 50, 51, 52, 8]. Thus, in order to assess the relevance of nematicity to the properties of these compounds, it is paramount to understand the interplay between disorder and nematic order. Previous works have focused mostly on non-vestigial Ising-nematic phases [53, 54, 55], including the role of Griffiths effects [56], and on random-field or random-mass types of disorder in the DW degrees of freedom [57, 58].

In this paper, we investigate the impact of rare regions on the vestigial Ising-nematic order arising from a DW quantum phase transition. A rare region is a relatively large droplet that is devoid of impurities in a disordered system (see Fig. 2.1). For our purposes, we consider point-like, randomly diluted impurities that completely suppress nematic and DW orders locally. Although the probability of finding such droplets decreases exponentially with their size, their impact on phase transitions can be significant , causing Griffiths singularities in thermodynamic quantities [59, 60] or smearing phase transitions [61]. These effects are particularly strong near a quantum phase transition, due to the fact that the impurity at $T = 0$ is perfectly correlated along the "time" axis [47, 62].

As we show here, the rare regions completely change the nature of the simultaneous

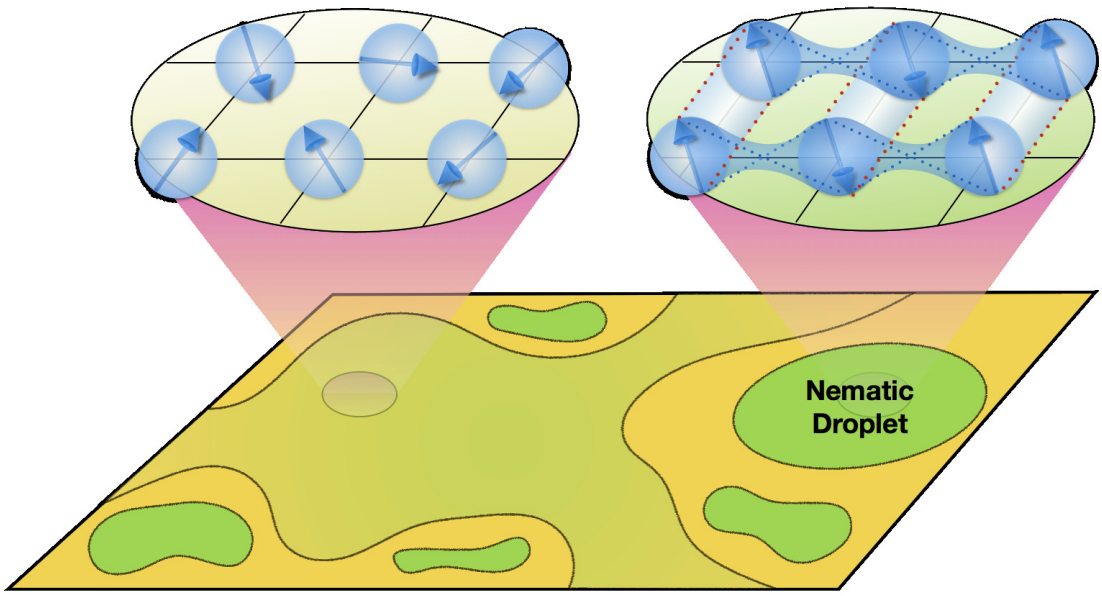

Figure 2.1: Illustration of a moderately diluted system displaying an infinite cluster (light green) and finite-size droplets (dark green) devoid of impurities. For this illustration, we consider a "mother" spin-density wave and its vestigial Ising-nematic phase. At $T = 0$, finite-size droplets cannot sustain long-range spin order (indicated by the disordered spins in the inset), but they can support long-range nematic order (indicated by the different spin-spin correlations along the x and y axis, resulting in unequal x and y bonds). Importantly, droplets of moderate sizes undergo a second-order nematic transition even before the bulk system (and thus the infinite cluster) undergoes its simultaneous first-order density-wave and nematic transition.

first-order nematic-DW quantum transition in a two-dimensional itinerant system. This is because of the crucial role of the droplet's dissipative quantum dynamics [63, 64, 65], which allows long-range Ising-nematic order in finite-size droplets at $T = 0$ (see also Ref. [45]), but not DW order (for spin or incommensurate charge density-waves). By performing large-N calculations on a finite-size droplet, we find a wide parameter range for which the first droplets to order nematically at $T = 0$ are not the largest ones, but the droplets of moderately large sizes. Remarkably, while the *largest droplets* undergo a *first-order* nematic transition very close to the quantum phase transition of the clean system, the droplets of *moderate sizes* undergo a *second-order* nematic transition even before the clean system orders. The result is the emergence of an inhomogeneously ordered nematic phase, characteristic of a smeared nematic quantum phase transition [47, 64], in the regime where the clean system is not ordered. Our findings, illustrated in Fig. 2.2, indicate also that a DW Griffiths phase appears inside this inhomogeneous nematic state, preceding the onset of long-range DW and homogeneous nematic order. As we argue below, this behavior may be related to recent puzzling experimental observations in iron-based compounds.

2.2 Low-energy model

We consider a general two-dimensional low-energy model that yields vestigial Ising-nematic order from a mother DW phase on the square lattice. For concreteness, we consider two N-component DW order parameters, $\mathbf{\Delta}_X$ and $\mathbf{\Delta}_Y$, corresponding to two wave-vectors $\mathbf{Q}_X = (Q, 0)$ and $\mathbf{Q}_Y = (0, Q)$ related by tetragonal symmetry. In the case of spin density-wave, $N = 3$ (commensurate) or $N = 6$ (incommensurate), whereas for charge density-wave, $N = 1$ (commensurate) or $N = 2$ (incommensurate). Hereafter, we consider only the case $N > 1$, as relevant for copper-based and iron-based superconductors. The low-energy action is given by[14]:

$$\begin{aligned} S\left[\mathbf{\Delta}_X, \mathbf{\Delta}_Y\right] &= \int_{\mathbf{q},\omega} \Big[\chi_{\mathbf{q},\omega}^{-1} \left(\mathbf{\Delta}_X^2 + \mathbf{\Delta}_Y^2\right) + \frac{u}{2} \left(\mathbf{\Delta}_X^2 + \mathbf{\Delta}_Y^2\right)^2 \\ &\quad - \frac{g}{2} \left(\mathbf{\Delta}_X^2 - \mathbf{\Delta}_Y^2\right)^2 \Big] \end{aligned} \tag{2.1}$$

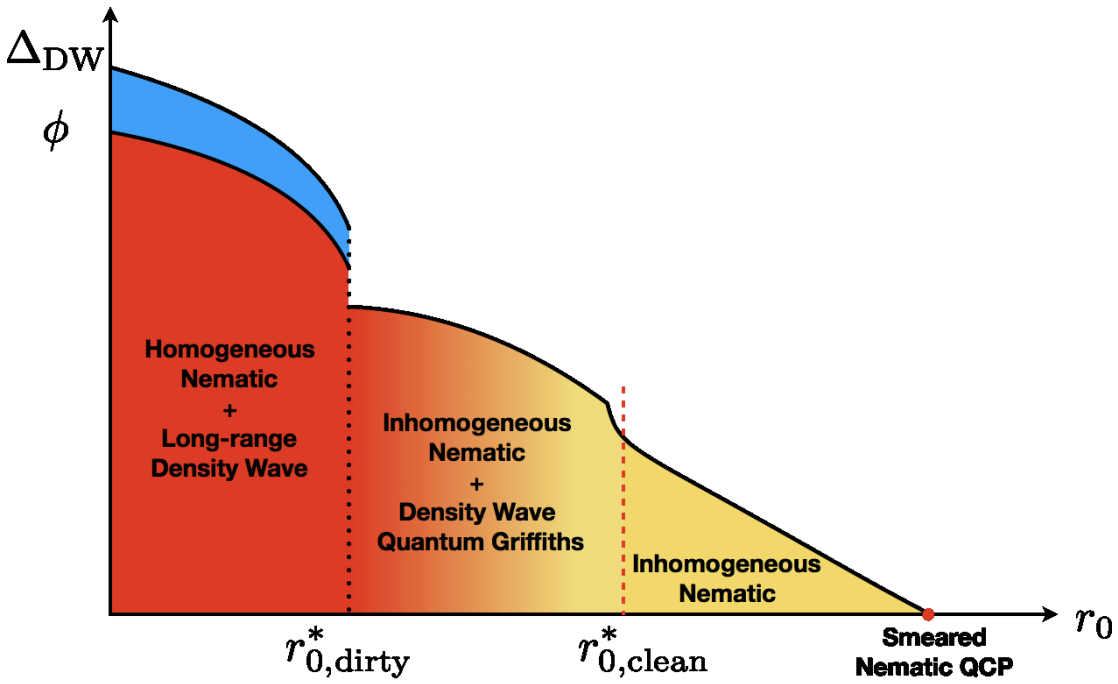

Figure 2.2: Schematic phase diagram illustrating our main results. Here, r_0 is a control parameter, such as doping or pressure. In the clean system at $T = 0$, the nematic (ϕ) and density-wave (Δ_{DW}) order parameters appear simultaneously at $r^*_{0,\mathrm{clean}}$ (dashed line). In the moderately diluted system, which still has a percolating (infinite) cluster, the first-order quantum transition is expected to be suppressed down to $r^*_{0,\mathrm{dirty}}$ (dotted line). For $r_0 > r^*_{0,\mathrm{clean}}$, moderately large droplets undergo a second-order nematic transition, giving rise to inhomogeneous nematic order. For $r^*_{0,\mathrm{dirty}} < r_0 < r^*_{0,\mathrm{clean}}$, exponentially large droplets have an exponentially large DW correlation length, resulting in a DW quantum Griffiths phase. Whether ϕ jumps or continuously evolves at $r^*_{0,\mathrm{dirty}}$ depends on details of the disorder distribution.

where $\int_{\mathbf{q},\omega} = \int \frac{d^d q}{(2\pi)^d} \int \frac{d\omega}{2\pi}$. Here, $\chi^{-1}_{\mathbf{q},\omega} = r_0 + \mathbf{q}^2 + \gamma \left|\omega\right|^{2/z}$ is the inverse DW susceptibility, with the "tuning parameter" r_0 denoting the distance to the mean-field quantum phase transition. For itinerant systems, the dynamical critical exponent is $z = 2$ and γ is the Landau damping coefficient. Vestigial Ising-nematic order arises when $g > 0$. Physically, the emergent Ising-nematic order parameter $\langle \phi \rangle = g \left\langle \mathbf{\Delta}_X^2 - \mathbf{\Delta}_Y^2 \right\rangle$, which can onset before the DW, corresponds to unequal fluctuations around the two DW wave-vectors. Mathematically, it is obtained by performing a Hubbard-Stratonovich transformation of the second quartic term of Eq. (2.1):

$$S_{\text{eff}} = \int_{\mathbf{q},\omega} \left\{ \frac{\phi^2}{2g} - \frac{\psi^2}{2u} + \frac{N}{2} \ln \left[\left(\chi^{-1}_{\mathbf{q},\omega} + \psi \right)^2 - \phi^2 \right] \right\} \tag{2.2}$$

To obtain this effective action, we also performed a Hubbard-Stratonovich transformation of the first quartic term of Eq. (2.1) to introduce the Gaussian-fluctuations field $\langle \psi \rangle = u \left\langle \mathbf{\Delta}_X^2 + \mathbf{\Delta}_Y^2 \right\rangle$. In the large-$N$ limit, and after rescaling the quartic coefficients $(u, g) \to (u, g)/N$, the equilibrium values of ϕ and ψ as function of r_0 can be found within the saddle-point approximation $\frac{\delta S_{\text{eff}}}{\delta \psi} = \frac{\delta S_{\text{eff}}}{\delta \phi} = 0$. Note that $r_0 + \psi = |\phi|$ indicates an instability towards the DW phase, whereas $\phi \neq 0$ indicates an instability towards the Ising-nematic phase. For $d = 2$, the two transitions are split at finite temperatures, but merge into a single first-order transition at $T = 0$ (see Fig. 2.2). These large-N results, reproduced in the Appendix A.1, were obtained before [14] and confirmed by renormalization group analysis [40, 41, 42].

2.3 Large-N solution for a single droplet

To assess the relevance of rare regions to the nematic and DW quantum phase transitions, we first solve the large-N saddle-point equations for a single droplet of linear size L, and later average over the distribution of droplets. The strategy is similar to that employed in Ref. [62] to study Griffiths effects near a metallic antiferromagnetic quantum critical point. Due to the finite size of the droplet, the momentum integration in Eq. (2.2) is replaced by a discrete sum over momenta $\mathbf{q} = \frac{2\pi}{L}\mathbf{n}$, with $\mathbf{n} = (n_x, n_y)$ and $n_{x,y}$ integer. The saddle-point equations at $T = 0$ become (details in Appendix

A.1):

$$
\begin{aligned}
r &= r_0 - ur\left(\ln\frac{\Lambda^2}{\sqrt{r^2-\phi^2}} + 1 - \frac{\phi}{r}\tanh^{-1}\frac{\phi}{r}\right) \\
&\quad + \frac{2\pi u}{L^2}\left\{\mathcal{F}\left[(r-\phi)\,L^2\right] + \mathcal{F}\left[(r+\phi)\,L^2\right]\right\} \qquad (2.3)\\
\phi &= \phi g\left(\ln\frac{\Lambda^2}{\sqrt{r^2-\phi^2}} + 1 - \frac{r}{\phi}\tanh^{-1}\frac{\phi}{r}\right) \\
&\quad + \frac{2\pi g}{L^2}\left\{\mathcal{F}\left[(r-\phi)\,L^2\right] - \mathcal{F}\left[(r+\phi)\,L^2\right]\right\} \qquad (2.4)
\end{aligned}
$$

where $r = r_0 + \psi$ is proportional to the inverse squared DW correlation length, $r_0 \to r_0 + u\int_{\mathbf{q},\omega}\frac{1}{q^2+\gamma|\omega|}$ is the renormalized distance to the DW quantum critical point, and Λ is the momentum cutoff, hereafter set to be $1/a$ (a is the lattice parameter). Note that the quartic coefficients have been rescaled by $u \to u/\left(4N\pi^2\gamma\right)$ and $g \to g/\left(4N\pi^2\gamma\right)$. The droplet finite-size effects are encoded in the function $\mathcal{F}(y) = \frac{1}{\pi}\sum_{\mathbf{n}\neq\mathbf{0}}\frac{\sqrt{y}}{|\mathbf{n}|}K_1\left(|\mathbf{n}|\sqrt{y}\right)$, where $K_1(x)$ is the modified Bessel function of the second kind. Because $\mathcal{F}(y \gg 1) \sim y^{1/4}\,\mathrm{e}^{-\sqrt{y}}$, Eqs. (2.3)-(2.4) recover the saddle-point expressions for the infinite system $L \to \infty$.

To understand how the finite size of the droplet affects the DW and nematic transitions, we recall that the DW transition takes place when $r = |\phi|$. But because $\mathcal{F}(y \ll 1) \sim -\ln y$, there is no solution to Eqs. (2.3)-(2.4) with $r = |\phi|$. This is a consequence of Mermin-Wagner theorem: at $T = 0$, the finite-size droplet has an effective dimensionality $d_{\text{eff}} = z = 2$, which is the lower critical dimension for the DW transition [62].

The situation is completely different for the Ising-nematic transition: since its lower critical dimension $d_c = 1 < d_{\text{eff}}$, long-range Ising-nematic order can onset at $T = 0$ even in a droplet of finite size L [45, 64]. To address which droplets order first, and the character of the Ising-nematic transition inside them, we solved Eqs. (2.3)-(2.4) to obtain $\phi(r_0, L)$. The results are shown in Fig. 2.3; for comparison, we also show the first-order behavior of the nematic order parameter of the clean system, $\phi_{\text{clean}} \equiv \phi(L \to \infty)$, which orders at $r^*_{0,\text{clean}} \equiv r^*_0(L \to \infty)$.

The figure illustrates two very different behaviors: droplets of moderately large sizes

display a non-zero nematic order parameter already in the non-ordered phase of the clean system, i.e. the nematic transition inside these droplets happens at $r_0^*(L) > r_{0,\text{clean}}^*$. Importantly, the nematic transition in these droplets is generally second-order. In contrast, large droplets undergo a first-order nematic transition very close to the clean phase transition, i.e. $r_0^*(L) \approx r_{0,\text{clean}}^*$. Note that small droplets (not shown) only order below $r_{0,\text{clean}}^*$. This is more clearly seen in the inset, which shows the nematic transition parameter $r_0^*(L)$ as function of the size L. For the particular values of u and g used here, $u = 0.9$ and $g = 0.25u$, the first droplet to order has "volume" $L^2 \approx 40a^2$, and all droplets with volumes smaller than $L^2 = 58a^2$ undergo a second-order nematic transition. As we show in Appendix A.2, this behavior is not specific to these values of u and g, but happen in a wide region of the (u, g) parameter space. Importantly, for all droplets, the DW transition does not take place, i.e. the nematic and DW quantum phase transitions are naturally split inside a finite-size droplet.

2.4 Average over droplets

To assess the impact of the nematically ordered droplets on the thermodynamic properties of the system, we need to average over the different possible droplets. The key quantity is thus the probability $P(V)$ of a impurity-free droplet of volume $V \equiv L^2$ being realized in the system, which is determined by the disorder distribution. For concreteness, we consider random dilutions that kill DW and nematic order at a given site with probability $1 - p$, such that $p = 0$ ($p = 1$) corresponds to the completely dirty (clean) system. Using results of percolation theory [66], we can write down the approximate expression (see Appendix A.3 for details):

$$P(V) = \frac{p_c V^{1-\tau} \exp(-V/V_0)}{\sum V^{1-\tau} \exp(-V/V_0)} \tag{2.5}$$

Here, $\tau = 187/91$ is a critical exponent, V_0 is the typical volume of an impurity-free droplet for a given p, and p_c is the percolation threshold for clean sites. Because V_0 changes from 0 to ∞ from $p = 0$, 1 to the percolation threshold $p = p_c$, we treat V_0 as our disorder "tuning parameter," instead of p.

We consider here the case where dilution is moderate, and the system is above the

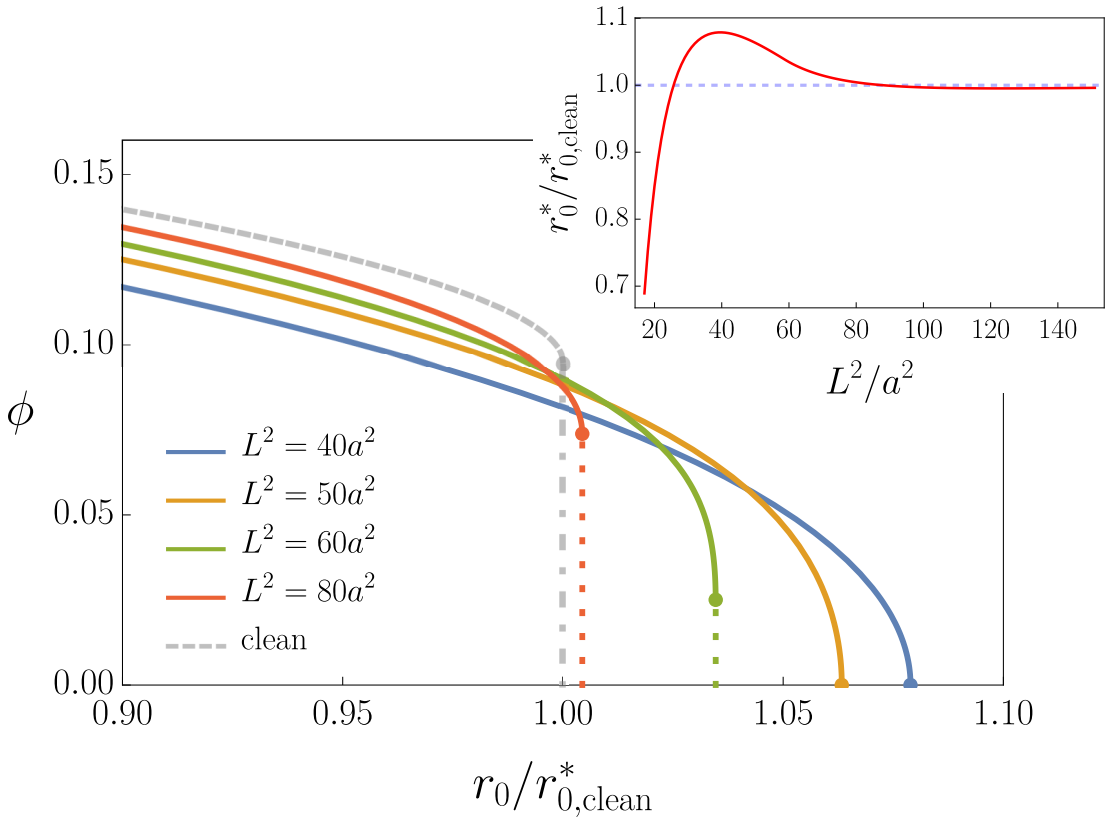

Figure 2.3: Nematic order parameter ϕ (in units of Λ^2) inside a droplet of "volume" L^2, as a function of the control parameter r_0 (in units of the value $r^*_{0,\mathrm{clean}}$ for which the clean system undergoes the first-order nematic transition). $\phi_{\mathrm{clean}} \equiv \phi\,(L \to \infty)$ is shown as a dashed line. First-order transitions are indicated by the dotted line. The inset shows the value of the tuning parameter r_0^* at the nematic transition inside a droplet as function of the droplet volume L^2.

percolating threshold for clean sites, $p > p_c$. In this case, in addition to the finite-size droplets described above, there is a single infinite percolating droplet devoid of impurities, which behaves similarly to the clean bulk system (see schematic Fig. 2.1). Because the infinite droplet has less sites than the bulk system, the DW-nematic first-order transition inside of it is expected to happen for $r^*_{0,\text{dirty}} < r^*_{0,\text{clean}}$. Thus, for $r_0 > r^*_{0,\text{dirty}}$, the average Ising-nematic order parameter is given solely by the contributions from the finite-size droplets, $\bar{\phi} = \sum P(V)\,\phi(V)\,dV$. We tacitly assume that there is a very weak inter-droplet interaction – for instance mediated by the lattice – that align the Ising-nematic order parameters of different droplets.

The results for $\bar{\phi}$ are show in Fig. 2.4 for different values of V_0. Because the first droplets to order have moderate sizes and undergo a second-order transition, $\bar{\phi}$ seems to evolve continuously as function of r_0. Our numerical result suggest a kink of $\bar{\phi}$ at $r^*_{0,\text{clean}}$, although a small jump might also be possible. This behavior is a consequence of the fact that most of the large droplets order very close to $r^*_{0,\text{clean}}$ (see inset of Fig. 2.3). At $r^*_{0,\text{dirty}}$, $\bar{\phi}$ acquires the additional contribution from the infinite droplet. At this point, the resulting nematic order parameter can then either undergo a meta-nematic transition, in which it jumps between two non-zero values, or display another kink in a continuous fashion. The ultimate behavior is determined by details of the disorder distribution beyond the scope of our model.

The proliferation of moderate-size droplets sustaining long-range nematic order upon approaching the clean DW-nematic quantum phase transition at $r^*_{0,\text{clean}}$ signals the emergence of an inhomogeneously ordered nematic state separated from the DW transition. The resulting phase transition is thus a smeared quantum phase transition. The smeared nematic quantum phase transition discovered here is very different than the smeared transitions discussed previously in other contexts [47, 61, 64] (for a review, see Ref. [19, 67]). First, in our case, many finite-size droplets order even before the clean system. Second, the droplets that order first are not the largest ones, but the droplets of intermediate size. This ensures the existence of a well-defined critical point, regardless of whether the disorder distribution is bounded or not. Finally, the size of the droplets determines not only when they order, but also the character of the corresponding phase transition (i.e. second- or first-order). As for the DW order, it only onsets at $r^*_{0,\text{dirty}}$, since finite-size droplets cannot sustain DW long-range order. However, in

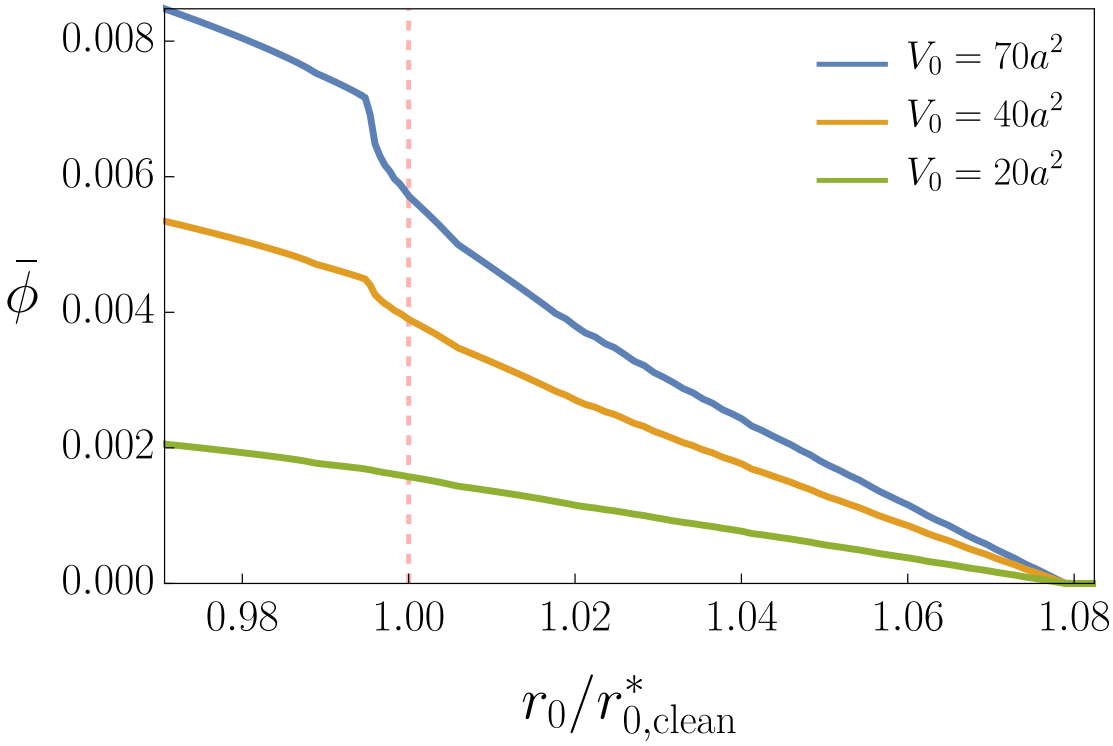

Figure 2.4: Average nematic order parameter of all droplets, $\bar{\phi}$ (in units of Λ^2), as function of the control parameter, r_0 (in units of $r^*_{0,\mathrm{clean}}$). Different curves correspond to different "critical" droplet volumes V_0 associated with the probability distribution (2.5).

the regime $r^*_{0,\mathrm{dirty}} < r_0 < r^*_{0,\mathrm{clean}}$, following the arguments of Ref. [62], exponentially large droplets have an exponentially large correlation length, which promote quantum Griffiths behavior. Thus, the regime of inhomogeneous nematic order is followed by a quantum Griffiths DW phase, as shown schematically in Fig. 2.2. The latter is characterized by power-law singularities of thermodynamic and DW-related quantities, with non-universal exponents that depend on r_0 [62]. Note that, although our analysis has been restricted to $T = 0$, we expect the smeared transition behavior to persist for small enough temperatures, as the moderate sizes of the relevant droplets can still be smaller than the nematic correlation length.

2.5 Concluding remarks

We showed that even weak disorder fundamentally alters the properties of the Ising-nematic quantum phase transition associated with a mother charge or spin density-wave quantum phase transition. The simultaneous first-order transition of the clean, itinerant system is replaced by an interesting regime that displays inhomogeneous (but long-range) smeared nematic order accompanied by a DW quantum Griffiths phase. The extent and relevance of this regime is controlled by the likelihood of finding isolated droplets of moderate (rather than very large) sizes, which in turn is controlled by the strength of disorder.

These results have important implications for the understanding of the phase diagrams of copper-based and iron-based superconductors, where an Ising-nematic phase has been argued to emerge from charge and/or spin density-waves. In the case of the iron pnictides, where the Ising-nematic and DW transition lines follow each other closely, these effects are expected to be more pronounced and less ambiguous. Interestingly, elasto-resistance measurements of the nematic susceptibility upon approaching the putative nematic-DW quantum phase transition from high temperatures revealed a weakening of fluctuations and deviation from Curie-Weiss behavior at low temperatures [56]. This behavior was observed only in compounds with sufficient degree of disorder. We argue that it could be attributed, at least in part, to the onset of long-range nematic order in finite-size droplets. This phenomenon may also help understand the appearance

of local inhomogeneous nematic order in NQR measurements in the nominally tetragonal state [68, 69]. Finally, magnetic measurements in Mn-doped $BaFe_2As_2$, which is significantly less homogeneous than other doped compounds, have been interpreted in terms of a magnetic Griffiths phase [70, 71]. It would be interesting to probe whether local nematic order also emerges in these compounds, simultaneously to the appearance of the reported Griffiths behavior.

Chapter 3

Transient dynamics of the superconducting gap in single band systems

3.1 Introduction to the quench dynamics of superconductivity

3.1.1 Superconductivity in equilibrium

Superconductivity is a phenomenon in which electricity can be transmitted without any dissipation. Although first discovered in 1911, its underline mechanism puzzled many notable physicists for more than 40 years, until 1957 when Bardeen, Cooper and Schrieffer (BCS) published the theory of superconductivity[72]. One of the key ideas in BCS theory is that electrons form Cooper pairs under the phonon-induced attractive interaction. The effective attraction between electrons is illustrated conceptually by Fig. 3.1. When negatively charged electrons move in the background of positive ions, the ion lattice is distorted by the presence of electron due to the attractive Coulomb interaction between ions and electrons. Such lattice distortion creates regions with higher positive charge densities, which attract other electrons. Mediated by this attractive interaction, electrons form the so-called Cooper pairs. BCS then established the pairing formalism that successfully describes the emergence of superconductivity.

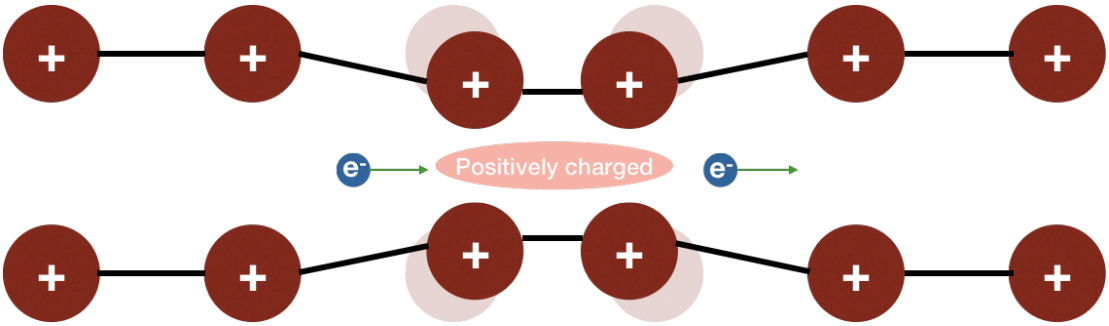

Figure 3.1: Schematics of the phonon-induced pairing mechanism.

The pairing formalism starts from the BCS reduced Hamiltonian where the electron-electron interactions other than the effective attraction between electrons with opposite momenta are neglected:

$$H_{\mathrm{BCS}} = \sum_{\mathbf{k},\sigma} \varepsilon_{\mathbf{k}} c^{\dagger}_{\mathbf{k},\sigma} c_{\mathbf{k},\sigma} + \frac{V}{N} \sum_{\mathbf{k},\mathbf{p}} c^{\dagger}_{\mathbf{k},\uparrow} c^{\dagger}_{-\mathbf{k},\downarrow} c_{-\mathbf{p},\downarrow} c_{\mathbf{p},\uparrow}, \tag{3.1}$$

where $c^{\dagger}_{\mathbf{k},\sigma}$ is electronic creation operater with momentum $\mathbf{k}$ and spin index σ, $\varepsilon_{\mathbf{k},\sigma}$ is the electronic dispersion, and $V < 0$ is the effective attractive electron-electron interaction which is simplified as momentum independent. Leon N. Cooper showed that Fermi liquid has an instability against the attractive electron-electron interaction across the Fermi surface[73]. So, we only consider consider such pairing interaction term and perform the mean-field decoupling: $\langle ABCD \rangle \approx \langle AB \rangle CD + AB \langle CD \rangle - \langle AB \rangle \langle CD \rangle$. By introducing the superconducting gap

$$\Delta = -\frac{V}{N} \sum_{\mathbf{p}} \langle c_{-\mathbf{p},\downarrow} c_{\mathbf{p},\uparrow} \rangle \,, \tag{3.2}$$

we arrive at the mean-field BCS Hamiltonian:

$$H_{\mathrm{BCS}} = \sum_{\mathbf{k},\sigma} \varepsilon_{\mathbf{k}} c^{\dagger}_{\mathbf{k},\sigma} c_{\mathbf{k},\sigma} - \sum_{\mathbf{k}} \left(\Delta c^{\dagger}_{\mathbf{k},\uparrow} c^{\dagger}_{-\mathbf{k},\downarrow} + \mathrm{h.c.} \right) - \frac{N}{V} |\Delta|^2 \,. \tag{3.3}$$

Several formalisms were developed to analyze the equilibrium properties of this mean-field Hamiltonian, such as Bogoliubov's canonical transformation[74], Anderson's pseudospin formalism[75] and Gor'kov's Green's function method[76]. We will introduce the

first two formalisms in details as they are later used in the non-equilibrium calculations.

Bogoliubov quasiparticles

The mean-field Hamiltonian, Eq. (3.3), can be diagonalized using the following Bogoliubov transformation:

$$c_{\mathbf{k},\uparrow} = u^*_{\mathbf{k}}\alpha_{\mathbf{k}} + v_{\mathbf{k}}\beta^\dagger_{\mathbf{k}}, \tag{3.4a}$$

$$c^\dagger_{-\mathbf{k},\downarrow} = u_{\mathbf{k}}\beta^\dagger_{\mathbf{k}} - v^*_{\mathbf{k}}\alpha_{\mathbf{k}}, \tag{3.4b}$$

where the new fermionic operators $\alpha_{\mathbf{k}}$ and $\beta^\dagger_{\mathbf{k}}$ are called the Bogoliubov quasiparticles. The complex coefficients of the transformation, $u_{\mathbf{k}}$ and $v_{\mathbf{k}}$, must satisfy $|u_{\mathbf{k}}|^2+|v_{\mathbf{k}}|^2 = 1$, in order to ensure the fermion operator algebra for $\alpha_{\mathbf{k}}$ and $\beta_{\mathbf{k}}$. In the literature, they are often called the coherence factors. The values of the coherence factors are chosen such that after the Bogoliubov transformation, Eq. (3.4), the mean-field Hamiltonian is diagonal in a sense that it only contains terms correspond to single-quasiparticle excitations:

$$H_{\mathrm{BCS}} = E_0 + \sum_{\mathbf{k}} E_{\mathbf{k}} \left(\alpha^\dagger_{\mathbf{k}}\alpha_{\mathbf{k}} + \beta^\dagger_{\mathbf{k}}\beta_{\mathbf{k}}\right), \tag{3.5}$$

where $E_{\mathbf{k}} = \sqrt{\varepsilon^2_{\mathbf{k}} + |\Delta|^2}$ is the dispersion of the Bogoliubov quasiparticles. $E_0 = \sum_{\mathbf{k}} (\varepsilon_{\mathbf{k}} - E_{\mathbf{k}}) - \frac{N}{V}|\Delta|^2$ is the ground state energy. The corresponding coherence factors are given by

$$u_{\mathbf{k}} = \sqrt{\frac{1}{2}\left(1 + \frac{\varepsilon_{\mathbf{k}}}{E_{\mathbf{k}}}\right)}, \tag{3.6a}$$

$$v_{\mathbf{k}} = e^{i\phi}\sqrt{\frac{1}{2}\left(1 - \frac{\varepsilon_{\mathbf{k}}}{E_{\mathbf{k}}}\right)}, \tag{3.6b}$$

where ϕ is the phase of the superconducting gap, i.e. $\Delta = |\Delta|\, e^{i\phi}$. The gap equation becomes

$$\Delta = -\frac{V}{N}\sum_{\mathbf{p}} u_{\mathbf{p}}v_{\mathbf{p}} \left(\left\langle \beta_{\mathbf{p}}\beta^\dagger_{\mathbf{p}}\right\rangle - \left\langle \alpha^\dagger_{\mathbf{p}}\alpha_{\mathbf{p}}\right\rangle\right). \tag{3.7}$$

In thermal equilibrium, $\left\langle \alpha_{\mathbf{k}} \alpha_{\mathbf{k}}^{\dagger} \right\rangle$ and $\left\langle \beta_{\mathbf{k}} \beta_{\mathbf{k}}^{\dagger} \right\rangle$ are given by the Fermi-Dirac distribution function, i.e. $\left\langle \alpha_{\mathbf{k}} \alpha_{\mathbf{k}}^{\dagger} \right\rangle = \left\langle \beta_{\mathbf{k}} \beta_{\mathbf{k}}^{\dagger} \right\rangle = n_{\mathrm{F}}\left(E_{\mathbf{k}}, T\right) = \frac{1}{1+\exp\left(\frac{E_{\mathbf{k}}}{T}\right)}$.

In this formalism, the ground state in the superconducting phase is the vacuum for Bogoliubov quasiparticles with ground state energy E_0. The excitation of the Bogoliubov quasiparticles with dispersion $E_{\mathbf{k}}$ is the fundamental excitation of the superconducting state.

Anderson pseudospins

The mean-field Hamiltonian can be recast into a form of the Hamiltonian in spin systems using the following transformation:

$$\hat{S}_{\mathbf{k}}^{-} = c_{-\mathbf{k},\downarrow} c_{\mathbf{k},\uparrow}, \tag{3.8a}$$

$$\hat{S}_{\mathbf{k}}^{+} = c_{\mathbf{k},\uparrow}^{\dagger} c_{-\mathbf{k},\downarrow}^{\dagger}, \tag{3.8b}$$

$$\hat{S}_{\mathbf{k}}^{z} = \frac{1}{2}\left(c_{\mathbf{k},\uparrow}^{\dagger} c_{\mathbf{k},\uparrow} + c_{-\mathbf{k},\downarrow}^{\dagger} c_{-\mathbf{k},\downarrow} - 1\right), \tag{3.8c}$$

where $\hat{S}_{\mathbf{k}}^{\pm} = \hat{S}_{\mathbf{k}}^{x} \pm i\hat{S}_{\mathbf{k}}^{y}$. This transformation is motivated by the fact that the BCS reduced Hamiltonian can be described by operators that only involve pair creation, pair annihilation and pair density[72, 75]. Within each pair, the electrons have opposite momenta and opposite spins. The essence of the mapping is summarized in Fig. 3.2(A), i.e. the occupied (empty) pair states are mapped into the pseudospin up (down) and the creation (annihilation) pair operators are simply pseudospin raising (lowering) operators.

After this mapping, the mean-field Hamiltonian becomes

$$H_{\mathrm{BCS}} = -\sum_{\mathbf{k}} \mathbf{B}_{\mathbf{k}} \cdot \hat{\mathbf{S}}_{\mathbf{k}} + \sum_{\mathbf{k}} \varepsilon_{\mathbf{k}} - \frac{N}{V}\left|\Delta\right|^2, \tag{3.9}$$

where the effective magnetic field is given by $\mathbf{B}_{\mathbf{k}} = 2\left(\left|\Delta\right|\cos\phi, -\left|\Delta\right|\sin\phi, -\varepsilon_{\mathbf{k}}\right)$, again ϕ is the phase of the superconducting gap. In the pseudospin formalism, the gap equation has the following simple form:

$$\Delta = -\frac{V}{N}\sum_{\mathbf{p}} \left\langle \hat{S}_{\mathbf{p}}^{-} \right\rangle. \tag{3.10}$$

In equilibrium, the pseudospins are parallel to the effective magnetic field in order to minimize energy. Comparing the two formalisms (Eq. (3.8) and (3.4)), we have the following equilibrium configuration for the pseudospins:

$$\left\langle \hat{S}^x_{\mathbf{k}} \right\rangle = \frac{|\Delta| \cos\phi}{2E_{\mathbf{k}}} \tanh\left(\frac{E_{\mathbf{k}}}{2T}\right), \tag{3.11}$$

$$\left\langle \hat{S}^y_{\mathbf{k}} \right\rangle = -\frac{|\Delta| \sin\phi}{2E_{\mathbf{k}}} \tanh\left(\frac{E_{\mathbf{k}}}{2T}\right), \tag{3.12}$$

$$\left\langle \hat{S}^z_{\mathbf{k}} \right\rangle = -\frac{\varepsilon_{\mathbf{k}}}{2E_{\mathbf{k}}} \tanh\left(\frac{E_{\mathbf{k}}}{2T}\right). \tag{3.13}$$

It is clear that the magnitude of the pseudospin is determined by the Fermi-Dirac distribution, i.e. $\left|\left\langle \hat{\mathbf{S}}_{\mathbf{k}} \right\rangle\right| = \frac{1}{2} - n_{\mathrm{F}} = \frac{1}{2}\tanh\left(\frac{E_{\mathbf{k}}}{2T}\right)$. As shown in Fig. 3.2(B), in the normal state at $T = 0$, the pseudospins below (above) the Fermi surface ($\varepsilon_{\mathbf{k}} = 0$) are pointing up (down), as all the pair states are occupied (empty) below (above) the Fermi surface. In the superconducting state, however, as the system develops a finite superconducting gap, all pseudospins will have a non-zero x-component. Consequently, the pseudospins develop a domain wall structure across the Fermi surface.

At $T = 0$, in the pseudospin formalism, we get the same ground state energy for the superconducting state as calculated using the Bogoliubov transformation:

$$\begin{aligned} E_0 &= -\sum_{\mathbf{k}} \frac{|\Delta|^2 \cos^2\phi + |\Delta|^2 \sin^2\phi + \varepsilon^2_{\mathbf{k}}}{E_{\mathbf{k}}} + \sum_{\mathbf{k}} \varepsilon_{\mathbf{k}} - \frac{N}{V}|\Delta|^2 \\ &= \sum_{\mathbf{k}} (\varepsilon_{\mathbf{k}} - E_{\mathbf{k}}) - \frac{N}{V}|\Delta|^2 . \end{aligned} \tag{3.14}$$

3.1.2 Typical time scales in non-equilibrium superconductivity

With the success of BCS theory, non-equilibrium properties of superconductivity were also thoroughly studied[75, 77, 78, 25]. Experimentally, superconductors are driven out of equilibrium typically by applying external fields. The typical time scale of this external perturbation is determined by the pulse shape of the external field. If this time scale is longer than the equilibration time, τ_{eq}, of the system, then the time evolution is in the adiabatic regime where the system stays in the ground state of the perturbed Hamiltonian. Such equilibration process is typically due to the scattering between electrons and

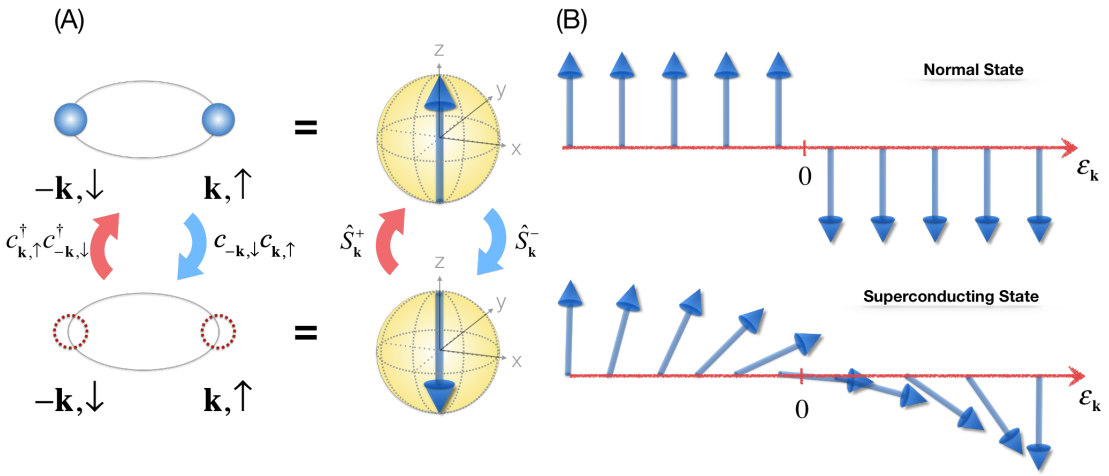

Figure 3.2: (A) Schematics of the mapping between the electronic operators and the pseudospin operators. (B) In the pseudospin formalism, the ground state of the normal phase corresponds to a Ising spin domain wall at the Fermi level ($\varepsilon_{\mathbf{k}} = 0$). In the superconducting phase, the ground state is represented by a domain wall structure across the Fermi level for Heisenberg spins, where the size of the domain wall is determined by the size of the superconducting gap.

phonons, which usually happens at a time scale of the order of nanoseconds. However, we will focus on the opposite regime, where the exotic states absent in equilibrium are accessible, and study the coherence dynamics of the superconducting gap.

In this non-adiabatic regime, the external perturbation is faster than the shortest intrinsic time scale of the system (indicated by the gray area in Fig. 3.3). For theoretical convenience, the external perturbation can be approximated by a instantaneous change of the Hamiltonian, which is called a quench. In fact, such a sudden change can be realized in some cold atom systems where a nearly-perfect control of the Hamiltonian is established. In solid state systems, the rapid perturbation can be achieved by the ultra-fast pump-probe technique[20]. Although the laser pump pulse only perturbs the electronic states, not the electronic interactions, the post-pump dynamics can still be approximated by the dynamics after an interaction quench. After all, these two different protocols are just two different ways to prepare the initial conditions for the dynamics out of equilibrium. Therefore, a theoretical study on the quench dynamics can provide valuable insights on the ultra-fast pump-probe experiments of superconductors as well.

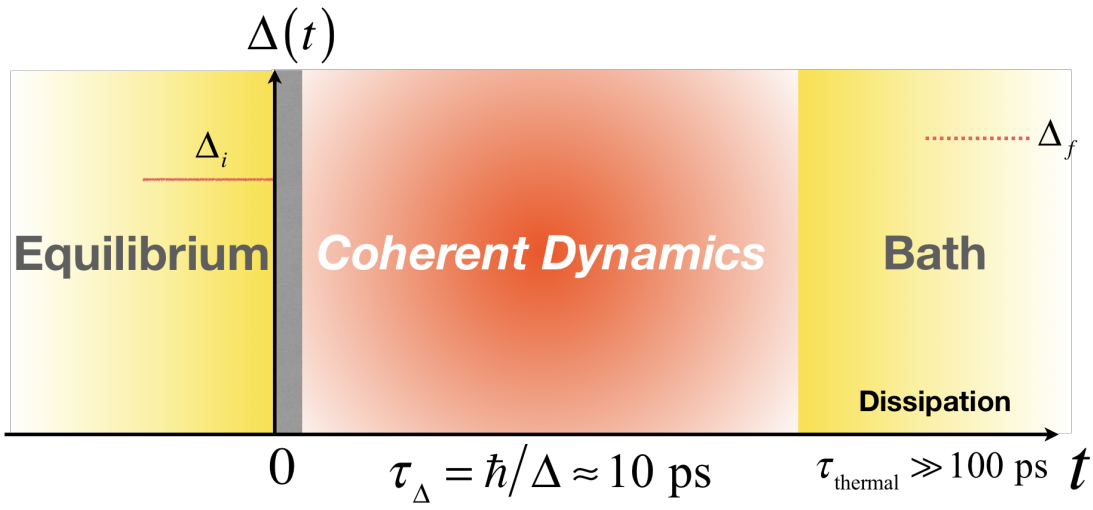

Figure 3.3: Typical time scales in non-equilibrium superconductivity. Δ_i (Δ_f) is the superconducting gap in thermal equilibrium for the pairing interaction v_i (v_f). In quantum quench protocols, $v_i \neq v_f$. In THz-pump-probe experiments, the pairing interaction is unchanged, therefore, $\Delta_i = \Delta_f$. In this case, the system is driven out of equilibrium by modifying the electronic states due to the coupling with the laser pump. Picture taken from Ref. [29]

In this section we will focus on the interaction quench scenario and study the post-quench dynamics of the superconductivity.

After the quench, the superconducting gap can exhibit coherent time evolution at a typical time scale determined by the superconducting gap: $\tau_\Delta = \hbar/\Delta$, which is typically around tens of picoseconds. Eventually, the electronic system thermalize with the phonon heat bath. As a consequence, the gap reaches its final equilibrium value at much larger time scales (as shown in Fig. 3.3).

Because the coherent dynamics of the superconducting gap occurs at the tens of picosecond time scale, conventional theoretical techniques for studying non-equilibrium properties such as time-dependent Ginzburg-Landau (TDGL) and Boltzmann kinetic equation are not suitable. These techniques often rely on a clear distinction between slow and fast degrees of freedom such that separate treatments of them do not lose any essential physics. For example, TDGL theory assumes that the superconducting gap changes much slower than the quasiparticle energy relaxation time, and Boltzmann kinetic equation requires adiabaticity of the quasiparticle distribution on the time scale

of τ_Δ. As a consequence, we adopt the approach that treats the dynamics of the gap and the dynamics of the quasiparticle distribution on equal footing, i.e. deriving the equations of motion of the BCS Hamiltonian.

3.2 Derivation of the equations of motion

In this section, we will derive the equations of motion of the mean-field BCS Hamiltonian (Eq. (3.3)). With the solutions of the equations of motion, the dynamics of the superconducting gap is then determined by the self-consistent gap equation (Eq. (3.2)). We consider an interaction quench protocol to drive the system out of equilibrium, where the electron-electron interaction is suddenly changed. Then the electronic degrees of freedom will evolve under the mean-field BCS Hamiltonian. As discussed in the previous section, both Bogoliubov quasiparticle and Anderson pseudospin are the proper descriptions of the electronic degrees of freedom of the mean-field BCS Hamiltonian. We will use both formalisms to derive the equations of motion.

3.2.1 Bogoliubov quasiparticles

In the previous section, we show how to use the Bogoliubov transformation to diagonalize the mean-field BCS Hamiltonian. In this subsection, we apply the density matrix formalism[79, 80, 81] to derive the equations of motion. After the Bogoliubov transformation (Eq. (3.4)), the mean-field BCS Hamiltonian is written in terms of Bogoliubov quasiparticles:

$$\begin{aligned} H_{\mathrm{BCS}}(t) &= E_0(t) + \sum_{\mathbf{k}} \Big\{ \Big[\varepsilon_{\mathbf{k}} \left(|u_{\mathbf{k}}|^2 - |v_{\mathbf{k}}|^2 \right) + \Delta(t)\, u_{\mathbf{k}} v_{\mathbf{k}}^* + \Delta^*(t)\, u_{\mathbf{k}}^* v_{\mathbf{k}} \Big] \left(\alpha_{\mathbf{k}}^\dagger \alpha_{\mathbf{k}} + \beta_{\mathbf{k}}^\dagger \beta_{\mathbf{k}} \right) \\ &\quad + \Big[\left(\Delta(t)\, u_{\mathbf{k}}^2 - \Delta^*(t)\, v_{\mathbf{k}}^2 - 2\varepsilon_{\mathbf{k}} u_{\mathbf{k}} v_{\mathbf{k}} \right) \alpha_{\mathbf{k}}^\dagger \beta_{\mathbf{k}}^\dagger + \mathrm{h.c.} \Big] \Big\}, \end{aligned} \tag{3.15}$$

Since the system is not at equilibrium, the mean-field BCS Hamiltonian is no longer diagonal in the quasiparticle basis of $\alpha_{\mathbf{k}}$ and $\beta_{\mathbf{k}}$. Such basis is defined by the coherence factor $u_{\mathbf{k}}$ and $v_{\mathbf{k}}$ which diagonalize the post-quench Hamiltonian when equilibrium is

reached,

$$u_{\mathbf{k}} = \sqrt{\frac{1}{2}\left(1 + \frac{\varepsilon_{\mathbf{k}}}{E_{\mathbf{k}}}\right)}, \tag{3.16a}$$

$$v_{\mathbf{k}} = e^{i\phi}\sqrt{\frac{1}{2}\left(1 - \frac{\varepsilon_{\mathbf{k}}}{E_{\mathbf{k}}}\right)}, \tag{3.16b}$$

where $E_{\mathbf{k}} = \sqrt{\varepsilon_{\mathbf{k}}^2 + |\Delta_f|^2}$ and $\Delta_f = |\Delta_f| e^{i\phi}$ is the equilibrium value of the gap after the quench. Substituting the coherence factor, we can rewrite the time-dependent mean-field BCS Hamiltonian in a more compact form:

$$H_{\mathrm{BCS}}(t) = E_0(t) + \sum_{\mathbf{k}} \left[\eta_{\mathbf{k}}(t)\left(\alpha_{\mathbf{k}}^{\dagger}\alpha_{\mathbf{k}} + \beta_{\mathbf{k}}^{\dagger}\beta_{\mathbf{k}}\right) + \left(\gamma_{\mathbf{k}}(t)\,\alpha_{\mathbf{k}}^{\dagger}\beta_{\mathbf{k}}^{\dagger} + \mathrm{h.c.}\right)\right], \tag{3.17}$$

where

$$\eta_{\mathbf{k}}(t) = \frac{\varepsilon_{\mathbf{k}}^2 + \mathrm{Re}\left[\Delta(t)\,\Delta_f^*\right]}{E_{\mathbf{k}}}, \tag{3.18a}$$

$$\gamma_{\mathbf{k}}(t) = \Delta_f\left[\frac{\varepsilon_{\mathbf{k}}}{E_{\mathbf{k}}}\left(\mathrm{Re}\frac{\Delta(t)}{\Delta_f} - 1\right) + i\mathrm{Im}\frac{\Delta(t)}{\Delta_f}\right]. \tag{3.18b}$$

Notice that the condensation energy becomes time-dependent in non-equilibrium,

$$E_0(t) = \sum_{\mathbf{k}}\left(\varepsilon_{\mathbf{k}} - \frac{\varepsilon_{\mathbf{k}}^2}{E_{\mathbf{k}}} - \frac{\Delta(t)\,\Delta_f^* + \Delta^*(t)\,\Delta_f}{2E_{\mathbf{k}}}\right) - \frac{N}{V}|\Delta(t)|^2. \tag{3.19}$$

The gap equation becomes:

$$\Delta(t) = -\frac{V}{N}\sum_{\mathbf{p}}\left[u_{\mathbf{p}}v_{\mathbf{p}}\left(\left\langle\beta_{\mathbf{p}}\beta_{\mathbf{p}}^{\dagger}\right\rangle - \left\langle\alpha_{\mathbf{p}}^{\dagger}\alpha_{\mathbf{p}}\right\rangle\right) + u_{\mathbf{p}}^2\left\langle\beta_{\mathbf{p}}\alpha_{\mathbf{p}}\right\rangle - v_{\mathbf{p}}^2\left\langle\alpha_{\mathbf{p}}^{\dagger}\beta_{\mathbf{p}}^{\dagger}\right\rangle\right]. \tag{3.20}$$

From the gap equation, it is clear that we need to solve for the quasiparticle densities $\left\langle\alpha_{\mathbf{k}}^{\dagger}\alpha_{\mathbf{k}}\right\rangle$, $\left\langle\beta_{\mathbf{k}}\beta_{\mathbf{k}}^{\dagger}\right\rangle$ and $\langle\beta_{\mathbf{k}}\alpha_{\mathbf{k}}\rangle$ in order to determine the dynamics of the superconducting gap ($\left\langle\alpha_{\mathbf{k}}^{\dagger}\beta_{\mathbf{k}}^{\dagger}\right\rangle$ is simply the Hermitian conjugate of $\langle\beta_{\mathbf{k}}\alpha_{\mathbf{k}}\rangle$). The time evolution of the

quasiparticle densities is governed by the Heisenberg equation of motion:

$$i\frac{d}{dt}\langle A\rangle = \langle [A, H_{\mathrm{BCS}}]\rangle \,. \tag{3.21}$$

Using the fermionic anti-commutation relation between Bogoliubov quasiparticles, we have the following equations of motion:

$$\begin{aligned}
i\frac{d}{dt}\left\langle \alpha^\dagger_{\mathbf{k}}\alpha_{\mathbf{k}}\right\rangle &= \gamma_{\mathbf{k}}(t)\left\langle \alpha^\dagger_{\mathbf{k}}\beta^\dagger_{\mathbf{k}}\right\rangle - \gamma^*_{\mathbf{k}}(t)\langle \beta_{\mathbf{k}}\alpha_{\mathbf{k}}\rangle \,, && \text{(3.22a)}\\
i\frac{d}{dt}\left\langle \beta_{\mathbf{k}}\beta^\dagger_{\mathbf{k}}\right\rangle &= \gamma^*_{\mathbf{k}}(t)\langle \beta_{\mathbf{k}}\alpha_{\mathbf{k}}\rangle - \gamma_{\mathbf{k}}(t)\left\langle \alpha^\dagger_{\mathbf{k}}\beta^\dagger_{\mathbf{k}}\right\rangle , && \text{(3.22b)}\\
i\frac{d}{dt}\langle \beta_{\mathbf{k}}\alpha_{\mathbf{k}}\rangle &= -2\eta_{\mathbf{k}}(t)\langle \beta_{\mathbf{k}}\alpha_{\mathbf{k}}\rangle - \gamma_{\mathbf{k}}(t)\left(\left\langle \alpha^\dagger_{\mathbf{k}}\alpha_{\mathbf{k}}\right\rangle - \left\langle \beta_{\mathbf{k}}\beta^\dagger_{\mathbf{k}}\right\rangle\right) . && \text{(3.22c)}
\end{aligned}$$

Given the initial conditions, the dynamics of the superconducting gap can be determined by solving the equations of motion (Eq. (3.22)) combining with the gap equation (Eq. (3.20)).

In the interaction quench protocol, the electron-electron interaction is suddenly changed. Let us say the quench happens at $t = 0$, and we call the initial interaction at $t < 0$, V_i and the interaction after quench, V_f. At $t < 0$, the system is in equilibrium. The pre-quench Hamiltonian is diagonalized by the Bogoliubov quasiparticle α_i and β_i. Here, the momentum dependence is kept implicit and the subscript i denotes the quasiparticle in the pre-quench basis. The equilibrium value of the gap corresponding to interaction constant V_i is denoted by Δ_i. Immediately after the quench, the system is still at the initial state, however, no longer in equilibrium, since the Hamiltonian was suddenly changed. Now we want to write this initial state in the basis of the post-quench Hamiltonian, by applying a basis transformation. Let the Bogoliubov quasiparticles in the post-quench basis be α_f and β_f. At $t = 0$, we have the following condition:

$$\begin{pmatrix} u^*_i & v_i \\ -v^*_i & u_i \end{pmatrix}\begin{pmatrix} \alpha_i \\ \beta^\dagger_i \end{pmatrix} = \begin{pmatrix} u^*_f & v_f \\ -v^*_f & u_f \end{pmatrix}\begin{pmatrix} \alpha_f \\ \beta^\dagger_f \end{pmatrix} . \tag{3.23}$$

Then, the initial conditions of Eq. (3.22) at the post-quench basis are:

$$\left\langle \alpha_f^\dagger \alpha_f \right\rangle = \left[\frac{1}{2} + \frac{\varepsilon^2 + |\Delta_i|\,|\Delta_f|}{2E_iE_f}\right]\left\langle \alpha_i^\dagger \alpha_i \right\rangle + \left[\frac{1}{2} - \frac{\varepsilon^2 + |\Delta_i|\,|\Delta_f|}{2E_iE_f}\right]\left\langle \beta_i \beta_i^\dagger \right\rangle, \tag{3.24a}$$

$$\left\langle \beta_f \beta_f^\dagger \right\rangle = \left[\frac{1}{2} - \frac{\varepsilon^2 + |\Delta_i|\,|\Delta_f|}{2E_iE_f}\right]\left\langle \alpha_i^\dagger \alpha_i \right\rangle + \left[\frac{1}{2} + \frac{\varepsilon^2 + |\Delta_i|\,|\Delta_f|}{2E_iE_f}\right]\left\langle \beta_i \beta_i^\dagger \right\rangle, \tag{3.24b}$$

$$\langle \beta_f \alpha_f \rangle = \frac{\varepsilon\,(\Delta_f - \Delta_i)}{2E_iE_f}\left(\left\langle \alpha_i^\dagger \alpha_i \right\rangle - \left\langle \beta_i \beta_i^\dagger \right\rangle\right). \tag{3.24c}$$

$\left\langle \alpha_i \alpha_i^\dagger \right\rangle$ and $\left\langle \beta_i \beta_i^\dagger \right\rangle$ are given by the same Fermi-Dirac distribution function $f\,(E_i, T) = \frac{1}{1+\exp\left(\frac{E_i}{T}\right)}$, where $E_{i/f} = \sqrt{\varepsilon^2 + \left|\Delta_{i/f}\right|^2}$ and T is the temperature of the system. The off-diagonal terms, e.g. $\langle \beta_i \alpha_i \rangle$ and $\left\langle \alpha_i^\dagger \beta_i^\dagger \right\rangle$ are zero due to the equilibrium condition before the quench. Therefore, for a given quench ($V_i \to V_f$), we have the following initial conditions for the post-quench equations of motion:

$$\left\langle \alpha_f^\dagger \alpha_f \right\rangle = \frac{1}{2} + \frac{\varepsilon^2 + |\Delta_i|\,|\Delta_f|}{2E_iE_f}\tanh\frac{E_i}{2T}, \tag{3.25a}$$

$$\left\langle \beta_f \beta_f^\dagger \right\rangle = \frac{1}{2} - \frac{\varepsilon^2 + |\Delta_i|\,|\Delta_f|}{2E_iE_f}\tanh\frac{E_i}{2T}, \tag{3.25b}$$

$$\langle \beta_f \alpha_f \rangle = \frac{\varepsilon\,(\Delta_f - \Delta_i)}{2E_iE_f}\tanh\frac{E_i}{2T}. \tag{3.25c}$$

3.2.2 Anderson pseudospins

In the pseudospin formalism, the equations of motion are more intuitive. The post-quench Hamiltonian is the same as Eq. (3.9), except that both the effective magnetic field and the pseudospins are time-dependent. Applying the spin algebra, $\left[\hat{S}_{\mathbf{k}}^\mu, \hat{S}_{\mathbf{P}}^\nu\right] = i\epsilon^{\mu\nu\lambda}\delta_{\mathbf{k},\mathbf{p}}\hat{S}_{\mathbf{k}}^\lambda$, the Heisenberg equations of motion of the pseudospins have the simple form of spin precession under magnetic fields:

$$\frac{d}{dt}\left\langle \hat{\mathbf{S}}_{\mathbf{k}} \right\rangle = -\mathbf{B}_{\mathbf{k}}\,(t) \times \left\langle \hat{\mathbf{S}}_{\mathbf{k}} \right\rangle. \tag{3.26}$$

However, the effective magnetic field is self-consistently determined by the pseudospin configurations, as $\mathbf{B}_{\mathbf{k}}(t) = 2\left(\mathrm{Re}\Delta(t), -\mathrm{Im}\Delta(t), -\varepsilon_{\mathbf{k}}\right)$ and

$$\Delta(t) = -\frac{V_f}{N}\sum_{\mathbf{k}}\left\langle \hat{S}_{\mathbf{k}}^{-}\right\rangle. \tag{3.27}$$

Before the quench, the pseudospins are parallel to the effective magnetic field defined by the initial value of the superconducting gap $\mathbf{B}_{\mathbf{k}} = 2\left(\mathrm{Re}\Delta_i, -\mathrm{Im}\Delta_i, -\varepsilon_{\mathbf{k}}\right)$. As a result, the initial conditions of the pseudospins are given by

$$\left\langle \hat{S}_{\mathbf{k}}^{x}\right\rangle_i = \frac{\mathrm{Re}\Delta_i}{2E}\tanh\left(\frac{E_i}{2T}\right), \tag{3.28a}$$

$$\left\langle \hat{S}_{\mathbf{k}}^{y}\right\rangle_i = -\frac{\mathrm{Im}\Delta_i}{2E}\tanh\left(\frac{E_i}{2T}\right), \tag{3.28b}$$

$$\left\langle \hat{S}_{\mathbf{k}}^{z}\right\rangle_i = -\frac{\varepsilon_{\mathbf{k}}}{2E}\tanh\left(\frac{E_i}{2T}\right). \tag{3.28c}$$

where $E_i = \sqrt{\varepsilon_{\mathbf{k}}^2 + |\Delta_i|^2}$. From the equations of motion (Eq. (3.26)), it is clear that $\left\langle \hat{\mathbf{S}}_{\mathbf{k}}^2\right\rangle$ is conserved, as

$$\frac{d}{dt}\left\langle \hat{\mathbf{S}}_{\mathbf{k}}^2\right\rangle = 2\left\langle \hat{\mathbf{S}}_{\mathbf{k}}\right\rangle \cdot \frac{d}{dt}\left\langle \hat{\mathbf{S}}_{\mathbf{k}}\right\rangle = -\left\langle \hat{\mathbf{S}}_{\mathbf{k}}\right\rangle \cdot \left(\mathbf{B}_{\mathbf{k}}(t) \times \left\langle \hat{\mathbf{S}}_{\mathbf{k}}\right\rangle\right) = 0. \tag{3.29}$$

Therefore, the quasiparticle distribution is invariant under time evolution.

3.2.3 Comparison between the quasiparticle and pseudospin formalisms

In the previous two subsections, we derived the post-quench equations of motion using two different formalisms. For the interaction quench protocol, within the BCS reduced Hamiltonian, these two formalisms are completely equivalent. But clearly, the pseudospin formalism is more concise and intuitive. So, we will use the pseudospin formalism for the remainder of the thesis.

If the external perturbation excites finite momentum fluctuations, the pseudospin formalism will lose the aforementioned advantages over the quasiparticle formalism since the pseudospin operators are no longer the complete set of operators for the non-equilibrium problem.

3.3 Exact solution of long-time asymptotic value

For conventional superconductors, the exact solution of the gap dynamics in interaction quench protocols can be extracted from the integrability of the BCS model[27, 82, 23, 26]. It is convenient to find the integrals of motion of the BCS Hamiltonian using the pseudospin formalism (Eq. (3.8)):

$$H_{\mathrm{BCS}} = \sum_{\mathbf{k}} 2\varepsilon_{\mathbf{k}} \hat{S}^z_{\mathbf{k}} + \frac{V}{N} \sum_{\mathbf{k},\mathbf{p}} \left(\hat{S}^x_{\mathbf{k}} \hat{S}^x_{\mathbf{p}} + \hat{S}^y_{\mathbf{k}} \hat{S}^y_{\mathbf{p}} \right). \tag{3.30}$$

The notion of integrability is only well-defined for classical systems. The BCS mean-field dynamics of the superconducting gap is indeed classical, as it only depends on the expectation values of the pseudospin operators (Eq. (3.26) and (3.27)). We can therefore study the classical Hamiltonian system by replacing the pseudospin operators, $\hat{\mathbf{S}}_{\mathbf{k}}$, with their expectation values, $\mathbf{S}_{\mathbf{k}} \equiv \left\langle \hat{\mathbf{S}}_{\mathbf{k}} \right\rangle$, and replacing the commutators by the Poisson brackets. The key observation that allows solving the non-equilibrium problem exactly is the fact that the BCS model at the mean-field approximation can be mapped to a linear combinations of central spin models[27]. Due to the particle-hole symmetry, the total z-component of the pseudospins is zero, i.e. $\sum_{\mathbf{k}} S^z_{\mathbf{k}} = 0$. And it is conserved because it commutes with the BCS Hamiltonian (Eq. (3.30))[75]. Therefore, we can write the BCS Hamiltonian in the following form:

$$H_{\mathrm{BCS}} = \sum_{\mathbf{k}} 2\varepsilon_{\mathbf{k}} S^z_{\mathbf{k}} + \frac{V}{N} \sum_{\mathbf{k},\mathbf{p}} \mathbf{S}_{\mathbf{k}} \cdot \mathbf{S}_{\mathbf{p}}. \tag{3.31}$$

which can be further rewritten as

$$H_{\mathrm{BCS}} = \sum_{\mathbf{k}} \left(2\varepsilon_{\mathbf{k}} H_{\mathbf{k}} + \frac{V}{N} \mathbf{S}^2_{\mathbf{k}} \right). \tag{3.32}$$

where

$$H_{\mathbf{k}} = \frac{V}{N} \sum_{\mathbf{p} \neq \mathbf{k}} \frac{\mathbf{S}_{\mathbf{k}} \cdot \mathbf{S}_{\mathbf{p}}}{\varepsilon_{\mathbf{k}} - \varepsilon_{\mathbf{p}}} + S^z_{\mathbf{k}}, \tag{3.33}$$

In order to rewrite $H_{\rm BCS}$ in terms of $H_{\mathbf{k}}$, we split the last term in Eq. (3.31) and interchange the summation over $\mathbf{k}$ and $\mathbf{p}$for one of them:

$$\begin{aligned}\frac{V}{N}\sum_{\mathbf{k},\mathbf{p}}\mathbf{S}_{\mathbf{k}}\cdot\mathbf{S}_{\mathbf{p}} &= \frac{V}{N}\sum_{\mathbf{k}}\sum_{\mathbf{p}\neq\mathbf{k}}\left(\frac{\varepsilon_{\mathbf{k}}-\varepsilon_{\mathbf{p}}}{\varepsilon_{\mathbf{k}}-\varepsilon_{\mathbf{p}}}\mathbf{S}_{\mathbf{k}}\cdot\mathbf{S}_{\mathbf{p}}+\mathbf{S}_{\mathbf{k}}^2\right)\\ &= \frac{V}{N}\sum_{\mathbf{k}}\sum_{\mathbf{p}\neq\mathbf{k}}\left(\frac{2\varepsilon_{\mathbf{k}}}{\varepsilon_{\mathbf{k}}-\varepsilon_{\mathbf{p}}}\mathbf{S}_{\mathbf{k}}\cdot\mathbf{S}_{\mathbf{p}}+\mathbf{S}_{\mathbf{k}}^2\right). \end{aligned} \tag{3.34}$$

It is obvious that $\mathbf{S}_{\mathbf{k}}^2$ is conserved according to the equations of motion (Eq. (3.26)), as $\mathbf{S}_{\mathbf{k}}\cdot\frac{d\mathbf{S}_{\mathbf{k}}}{dt}=0$. In order to show that $H_{\mathbf{k}}$ is the other set of integrals of motion, we calculate the commutator between $H_{\mathbf{k}}$ and $H_{\mathbf{k}'}$ with $\mathbf{k}\neq\mathbf{k}'$:

$$\begin{aligned}[H_{\mathbf{k}},H_{\mathbf{k}'}] &= \left[S_{\mathbf{k}}^z,\frac{V}{N}\sum_{\mathbf{p}\neq\mathbf{k}'}\frac{\mathbf{S}_{\mathbf{k}'}\cdot\mathbf{S}_{\mathbf{p}}}{\varepsilon_{\mathbf{k}'}-\varepsilon_{\mathbf{p}}}\right]+\left[\frac{V}{N}\sum_{\mathbf{p}\neq\mathbf{k}}\frac{\mathbf{S}_{\mathbf{k}}\cdot\mathbf{S}_{\mathbf{p}}}{\varepsilon_{\mathbf{k}}-\varepsilon_{\mathbf{p}}},S_{\mathbf{k}'}^z\right]\\ &\quad+\frac{V^2}{N^2}\left[\sum_{\mathbf{p}\neq\mathbf{k}}\frac{\mathbf{S}_{\mathbf{k}}\cdot\mathbf{S}_{\mathbf{p}}}{\varepsilon_{\mathbf{k}}-\varepsilon_{\mathbf{p}}},\sum_{\mathbf{p}\neq\mathbf{k}'}\frac{\mathbf{S}_{\mathbf{k}'}\cdot\mathbf{S}_{\mathbf{p}}}{\varepsilon_{\mathbf{k}'}-\varepsilon_{\mathbf{p}}}\right]. \end{aligned} \tag{3.35}$$

The first two terms add up to zero:

$$\begin{aligned}&\left[S_{\mathbf{k}}^z,\frac{V}{N}\sum_{\mathbf{p}\neq\mathbf{k}'}\frac{\mathbf{S}_{\mathbf{k}'}\cdot\mathbf{S}_{\mathbf{p}}}{\varepsilon_{\mathbf{k}'}-\varepsilon_{\mathbf{p}}}\right]+\left[\frac{V}{N}\sum_{\mathbf{p}\neq\mathbf{k}}\frac{\mathbf{S}_{\mathbf{k}}\cdot\mathbf{S}_{\mathbf{p}}}{\varepsilon_{\mathbf{k}}-\varepsilon_{\mathbf{p}}},S_{\mathbf{k}'}^z\right]\\ &= \frac{V}{N}\left(\frac{S_{\mathbf{k}'}^xS_{\mathbf{k}}^y-S_{\mathbf{k}'}^yS_{\mathbf{k}}^x}{\varepsilon_{\mathbf{k}'}-\varepsilon_{\mathbf{k}}}+\frac{S_{\mathbf{k}'}^xS_{\mathbf{k}}^y-S_{\mathbf{k}'}^yS_{\mathbf{k}}^x}{\varepsilon_{\mathbf{k}}-\varepsilon_{\mathbf{k}'}}\right)\\ &= 0 \end{aligned} \tag{3.36}$$

The last commutator in Eq. (3.35) is also zero:

$$\begin{aligned}
&\left[\sum_{\mathbf{p}\neq\mathbf{k}}\frac{S^{\mu}_{\mathbf{k}}\cdot S^{\mu}_{\mathbf{p}}}{\varepsilon_{\mathbf{k}}-\varepsilon_{\mathbf{p}}},\sum_{\mathbf{p}'\neq\mathbf{k}'}\frac{S^{\nu}_{\mathbf{k}'}\cdot S^{\nu}_{\mathbf{p}'}}{\varepsilon_{\mathbf{k}'}-\varepsilon_{\mathbf{p}'}}\right]\\
=&\sum_{\mathbf{p}\neq\mathbf{k}}\sum_{\mathbf{p}'\neq\mathbf{k}'}\frac{S^{\mu}_{\mathbf{k}}\left[S^{\mu}_{\mathbf{p}},S^{\nu}_{\mathbf{k}'}\right]S^{\nu}_{\mathbf{p}'}+S^{\mu}_{\mathbf{k}}S^{\nu}_{\mathbf{k}'}\left[S^{\mu}_{\mathbf{p}},S^{\nu}_{\mathbf{p}'}\right]+S^{\nu}_{\mathbf{k}'}\left[S^{\mu}_{\mathbf{k}},S^{\nu}_{\mathbf{p}'}\right]S^{\mu}_{\mathbf{p}}}{\left(\varepsilon_{\mathbf{k}}-\varepsilon_{\mathbf{p}}\right)\left(\varepsilon_{\mathbf{k}'}-\varepsilon_{\mathbf{p}'}\right)}\\
=&\sum_{\mathbf{p}\neq\mathbf{k}\neq\mathbf{k}'}\left[\frac{\epsilon_{\mu\nu\lambda}S^{\mu}_{\mathbf{k}}S^{\nu}_{\mathbf{p}}S^{\lambda}_{\mathbf{k}'}}{\varepsilon_{\mathbf{k}}-\varepsilon_{\mathbf{k}'}}\left(\frac{1}{\varepsilon_{\mathbf{k}'}-\varepsilon_{\mathbf{p}}}-\frac{1}{\varepsilon_{\mathbf{k}}-\varepsilon_{\mathbf{p}}}\right)+\frac{\epsilon_{\mu\nu\lambda}S^{\mu}_{\mathbf{k}}S^{\nu}_{\mathbf{k}'}S^{\lambda}_{\mathbf{p}}}{\left(\varepsilon_{\mathbf{k}}-\varepsilon_{\mathbf{p}}\right)\left(\varepsilon_{\mathbf{k}'}-\varepsilon_{\mathbf{p}}\right)}\right]\\
=&\sum_{\mathbf{p}\neq\mathbf{k}\neq\mathbf{k}'}\frac{\epsilon_{\mu\nu\lambda}S^{\mu}_{\mathbf{k}}S^{\nu}_{\mathbf{p}}S^{\lambda}_{\mathbf{k}'}+\epsilon_{\mu\nu\lambda}S^{\mu}_{\mathbf{k}}S^{\nu}_{\mathbf{k}'}S^{\lambda}_{\mathbf{p}}}{\left(\varepsilon_{\mathbf{k}}-\varepsilon_{\mathbf{p}}\right)\left(\varepsilon_{\mathbf{k}'}-\varepsilon_{\mathbf{p}}\right)}\\
=&\ 0
\end{aligned}\tag{3.37}$$

Hence, $H_{\mathbf{k}}$ commute with each other: $[H_{\mathbf{k}},H_{\mathbf{k}'}]=0$. It is rather straightforward that $\left[H_{\mathbf{k}},\mathbf{S}^2_{\mathbf{k}}\right]=0$. Therefore, $[H_{\mathbf{k}},H_{\mathrm{BCS}}]=0$ and in Eq. (3.32) we successfully write the BCS Hamiltonian as a sum of the integrals of motion. Since the total number of $\mathbf{k}$-states is N and we found $2N+1$ number of integrals of motion ($H_{\mathbf{k}}$, $\mathbf{S}^2_{\mathbf{k}}$ and $\sum_{\mathbf{k}}S^z_{\mathbf{k}}$), the BCS model is integrable.

The oscillation frequency and the asymptotic value of the gap are obtained with the help of the construction of the Lax vector[27, 26, 23]:

$$\mathbf{L}_{\mathbf{q}}=\hat{z}+\frac{V}{N}\sum_{\mathbf{k}\neq\mathbf{q}}\frac{\mathbf{S}_{\mathbf{k}}}{\varepsilon_{\mathbf{q}}-\varepsilon_{\mathbf{k}}}.\tag{3.38}$$

$\mathbf{L}^2_{\mathbf{q}}$ is also a conserved quantity, as it consists of the integrals of motion,

$$\mathbf{L}^2_{\mathbf{q}}=1+\frac{V^2}{N^2}\sum_{\mathbf{k}\neq\mathbf{q}}\frac{\hat{\mathbf{S}}^2_{\mathbf{k}}}{\left(\varepsilon_{\mathbf{q}}-\varepsilon_{\mathbf{k}}\right)^2}+\frac{V}{N}\sum_{\mathbf{k}\neq\mathbf{q}}\frac{2}{\varepsilon_{\mathbf{q}}-\varepsilon_{\mathbf{k}}}\left[\frac{V}{N}\sum_{\mathbf{p}\neq\mathbf{k}}\frac{\hat{\mathbf{S}}_{\mathbf{k}}\cdot\hat{\mathbf{S}}_{\mathbf{p}}}{\varepsilon_{\mathbf{k}}-\varepsilon_{\mathbf{p}}}+\hat{S}^z_{\mathbf{k}}\right]\tag{3.39}$$

$$=1+\frac{V}{N}\sum_{\mathbf{k}\neq\mathbf{q}}\frac{1}{\varepsilon_{\mathbf{q}}-\varepsilon_{\mathbf{k}}}\left[\frac{V}{N}\frac{\hat{\mathbf{S}}^2_{\mathbf{k}}}{\left(\varepsilon_{\mathbf{q}}-\varepsilon_{\mathbf{k}}\right)}+2H_{\mathbf{k}}\right]\tag{3.40}$$

As shown in Ref. [27, 26, 23], the complex roots of $\mathbf{L}^2_{\mathbf{q}}$ determines the long-time asymptotic value of the gap as well as the gap oscillation frequency. It is convenient to work in

the energy space by using the transformation, $-\frac{V}{N}\sum_{\mathbf{k}} \to v\int d\varepsilon$, where $v=-V\mathcal{N}$ is the coupling constant after the quench divided by the density of states at the Fermi level $\mathcal{N}$. Since $\mathbf{L}^2$ is conserved, we evaluate it by substituting the initial conditions for the pseudospins at $T=0$ (Eq. (3.28)) for the Lax vector of the post-quench Hamiltonian (with coupling constant v_f):

$$\mathbf{L}^2(u)=\left(\hat{z}-v_f\int d\varepsilon\frac{\Delta_i\hat{x}-\varepsilon\hat{z}}{2(u-\varepsilon)\sqrt{\varepsilon^2+\Delta_i^2}}\right)^2, \tag{3.41}$$

where the auxiliary spectral parameter, u, is complex, and the initial value of the gap, Δ_i, is chosen to be real. Normalizing the energy by the initial value of the gap and introducing the dimensionless variables $s=u/\Delta_i$ and $\xi=\varepsilon/\Delta_i$, we have

$$\begin{aligned}\mathbf{L}^2(s)&=\left(\hat{z}-v_f\int d\xi\frac{\hat{x}-\xi\hat{z}}{2(s-\xi)\sqrt{\xi^2+1}}\right)^2\\&=v_f^2G^2(s)+v_f^2\left[sG(s)+\ln\left(\frac{\Delta_i}{\Delta_f}\right)\right]^2.\end{aligned} \tag{3.42}$$

where $G(s)=\frac{1}{2}\int_{-\infty}^{\infty}\frac{d\xi}{s-\sinh(\xi)}=\frac{1}{2\sqrt{1+s^2}}\ln\frac{s+\sqrt{1+s^2}}{s-\sqrt{1+s^2}}$. A detailed analysis of the gap dynamics (see e.g. Ref. [23]) shows that the oscillation frequency and the asymptotic value of the gap is determined by the root(s) of the Lax vector. From Eq. (3.42), it is clear that the root(s) is (are) located at the imaginary axis, i.e. $\mathbf{L}^2\left(i\frac{\Delta_\infty}{\Delta_i}\right)=0$. Solving for Δ_∞/Δ_i, we get the asymptotic value of the gap as a function of the quench parameter, Δ_i/Δ_f, as shown in Fig. 3.4(A). There are three quench parameter regimes corresponds to three different asymptotic behaviors of the gap dynamics, as shown in Fig. 3.4(B)-(D). Regime A is defined by $\Delta_i/\Delta_f<e^{-\pi/2}$. In this regime, the gap persistently oscillates between Δ_+ and Δ_- (see Fig. 3.4(B)). In regime B, where $e^{-\pi/2}<\Delta_i/\Delta_f<e^{\pi/2}$, the gap oscillates with frequency $2\Delta_\infty$ and $t^{-1/2}$ damping (see Fig. 3.4(C)). In regime C, where $\Delta_i/\Delta_f>e^{\pi/2}$, the gap decays exponentially to zero (see Fig. 3.4(D)). We will focus more on the weak quench regime (regime B), where the

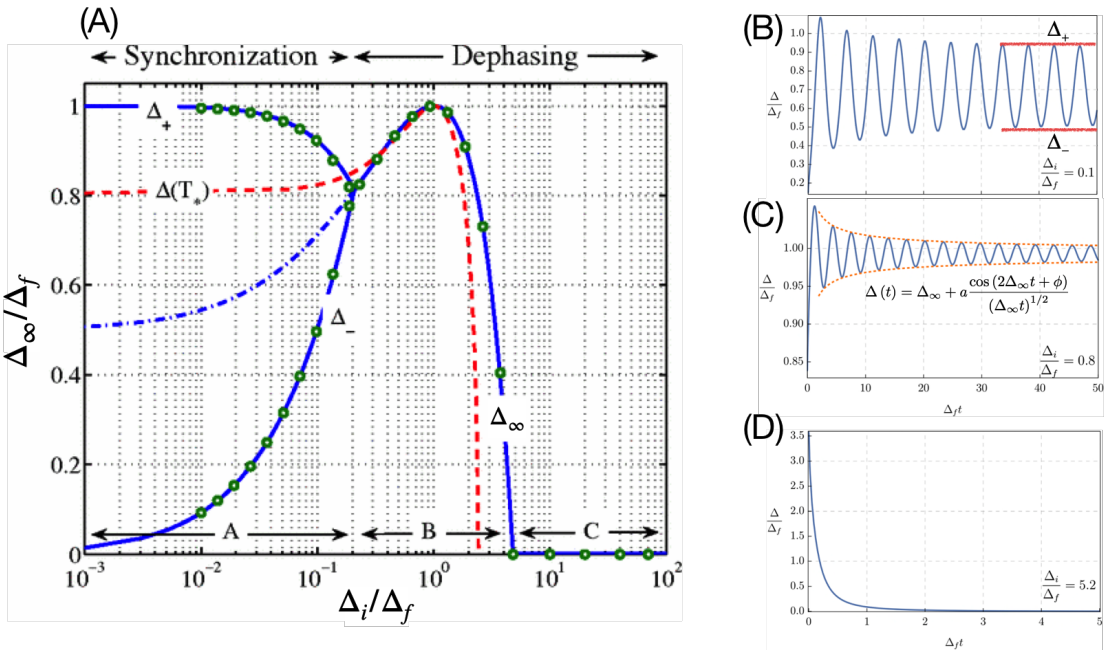

Figure 3.4: (A) Phase diagram of the gap dynamics of single-band superconductors (Figure taken from Ref. [23]). (B) The persistent gap oscillation between Δ_+ and Δ_-, when the quench parameter is in regime A ($\Delta_i/\Delta_f < e^{-\pi/2}$). (C) The $2\Delta_\infty$-oscillation with $t^{-1/2}$ damping in regime B ($e^{-\pi/2} < \Delta_i/\Delta_f < e^{\pi/2}$). (C) Then exponential decay of the gap in regime C ($\Delta_i/\Delta_f > e^{\pi/2}$).

asymptotic behavior of gap oscillation is given by

$$\Delta(t) = \Delta_\infty + a\frac{\cos(2\Delta_\infty t + \phi)}{(\Delta_\infty t)^{1/2}}, \tag{3.43}$$

since such regime is more relevant to experiments. We will later compare this exact result with the one obtained from the self-consistent perturbation theory. But before that, we would like to discuss what could potentially break the integrability of the BCS model.

There are two crucial conservation laws that lead to the success of mapping the BCS Hamiltonian into central spin models, Eq. (3.31) and (3.32). The first one is the

conservation of the total z-component of the pseudospins. More generally,

$$\sum_{\mathbf{k}} \left\langle \hat{S}^z_{\mathbf{k}} \right\rangle = 2N_{\text{pairs}} - N_{\text{total}}, \tag{3.44}$$

where N_{total} is the total number of available states and N_{pairs} is the number of pair-occupied states. Therefore, for systems with particle-hole symmetry, $\sum_{\mathbf{k}} \left\langle \hat{S}^z_{\mathbf{k}} \right\rangle = 0$. However, the conservation of $\sum_{\mathbf{k}} \left\langle \hat{S}^z_{\mathbf{k}} \right\rangle$, i.e. $\left[\sum_{\mathbf{k}} \hat{S}^z_{\mathbf{k}}, H_{\text{BCS}}\right] = 0$, is independent of the particle-hole symmetry. What it implies is the conservation of the number of pair-occupied states within the subspace of $n_{\mathbf{k}} = n_{-\mathbf{k}}$. As a result, any perturbations involving processes of pair breaking or imbalance between $n_{\mathbf{k}}$ and $n_{-\mathbf{k}}$, e.g. generation of quasiparticles or supercurrents, will break the integrability of the BCS model (Eq. (3.30)).

The second indispensable conservation law is the conservation of the quasiparticle distribution, $\left[\hat{\mathbf{S}}^2_{\mathbf{k}}, H_{\text{BCS}}\right] = 0$. This is due to the fact that quasiparticle scattering is absent in the BCS mean-field Hamiltonian (see Eq. (3.5)). Out of equilibrium, such collisionless regime is valid as long as the variation of the gap happens within the quasiparticle scattering time, as discussed in Section 3.1.2. However, the presence of impurities, which mediates quasiparticle scattering, will eventually break the integrability of the BCS model. A model that incorporates the aforementioned integrability-breaking processes to describe the gap dynamics observed in experiments, will be discussed in Section 5.5.

3.4 Perturbative solution

An alternative approach to solve the problem of the gap dynamics is to expand the equations of motion around the asymptotic value of the gap self-consistently. Similar perturbative approach was used to study the gap dynamics by A. F. Volkov and Sh. M. Kogan[25]. However, they expanded gap around its equilibrium value, which facilitated the linearization of the equations of motion. Although the analytical expression of the gap oscillation was obtained, the asymptotic value of the gap and the oscillation frequency were off comparing to the exact solution. We improve the perturbative approach by expanding the gap around the long-time asymptotic value and imposing the

self-consistency condition to ensure the long-time dynamics converges to the asymptotic value. Concretely, in the long-time limit, we separate the pseudospins and the gap into stationary and non-stationary components:

$$S^z = S^z_\infty + g(t), \tag{3.45a}$$
$$S^- = S^-_\infty + f(t), \tag{3.45b}$$
$$\Delta(t) = \Delta_\infty + \delta\Delta(t), \tag{3.45c}$$

where $S^\pm_\infty = S^x_\infty$, $S^y_\infty = 0$, $\varepsilon S^x_\infty = -\Delta_\infty S^z_\infty$. We work in the energy space and keep the energy dependence of the pseudospins implicit. Based on the gap equation, we have the following relations:

$$\Delta_\infty = v_f \int d\varepsilon S^x_\infty, \tag{3.46}$$
$$\delta\Delta(t) = v_f \int d\varepsilon f(t). \tag{3.47}$$

We first rewrite the equations of motion (Eq. (3.26)) as the following:

$$\dot{S}^z = -i\Delta(t)\left(S^+ - S^-\right), \tag{3.48}$$
$$\dot{S}^- = -2i\left[\varepsilon S^- + \Delta(t) S^z\right]. \tag{3.49}$$

Then by substituting Eq. (3.45), the equations of motion are linearized:

$$\dot{f}'(t) = 2\varepsilon f''(t), \tag{3.50a}$$
$$\dot{f}''(t) = -2\varepsilon f'(t) - 2\Delta_\infty g(t) - 2S^z_\infty \delta\Delta(t), \tag{3.50b}$$
$$\dot{g}(t) = 2\Delta_\infty f''(t), \tag{3.50c}$$

where $f(t) = f'(t) + if''(t)$. The linearized equations of motion are good approximations to Eq. (3.26), assuming the deviations from the stationary part are small. The validity of this assumption is crucial for capturing the correct dynamics of the gap but not the correct asymptotic value of the gap. Contributions from higher order terms will converge to the same asymptotic value when self-consistency is imposed. So in this subsection, we will apply Laplace analysis to the linearized equations of motion (Eq.

(3.50)) and extract the long-time asymptotic value of the gap.

We further simplify the linearized equations of motion by eliminating $g(t)$:

$$\ddot{f}''(t) = -4E_\infty^2 f''(t) - 2S_\infty^z \delta\dot{\Delta}(t), \tag{3.51a}$$

$$\dddot{f}'(t) = -4E_\infty^2 \dot{f}'(t) - 4\varepsilon S_\infty^z \delta\dot{\Delta}(t), \tag{3.51b}$$

where $E_\infty = \sqrt{\varepsilon^2 + \Delta_\infty^2}$. The variation of the gap, $\delta\Delta$, and the variation of the pair-occupied states, f, are related through the gap equation (Eq. (3.47)). Due to integrability, the information of the initial condition is not lost in the coherent time evolution. Therefore, in order to extract the long-time asymptotic behavior, we need to keep the information of the initial states. A ordinary differential equation with such properties is known to be particularly well suited for a Laplace analysis, rather than a Fourier analysis. The Laplace transformation is given by:

$$y(s) = \int_0^\infty y(t)\, e^{-st} dt \tag{3.52}$$

Integrating by parts, we obtain the following identity for the Laplace transformation of $\dot{y}(t)$:

$$\begin{aligned}\int_0^\infty \dot{y}(t)\, e^{-st} dt &= \left[y(t)\, e^{-st}\right]_0^\infty + s\int_0^\infty y(t)\, e^{-st} dt \\ &= sy(s) - y(t=0).\end{aligned} \tag{3.53}$$

Laplace transformation of higher derivatives can be obtained in the same fashion.

Applying Laplace transformation, the above linearized equations are

$$f''(s) + \frac{2sS_\infty^z}{s^2+4E_\infty^2}\delta\Delta(s) = \frac{sf_0'' + \dot{f}_0''}{s^2+4E_\infty^2} + \frac{2S_\infty^z}{s^2+4E_\infty^2}\delta\Delta_0, \tag{3.54a}$$

$$f'(s) - \frac{-4\varepsilon S_\infty^z}{s^2+4E_\infty^2}\delta\Delta(s) = \frac{1}{s}\left[f_0' - \frac{-4\varepsilon S_\infty^z}{s^2+4E_\infty^2}\delta\Delta_0\right] - \frac{2\varepsilon}{s}\frac{sf_0'' + \dot{f}_0''}{s^2+4E_\infty^2}, \tag{3.54b}$$

where s is the complex frequency in the Laplace domain. The initial conditions are formulated via: $f_0 \equiv f(t=0^+)$, $\delta\Delta_0 \equiv \delta\Delta(t=0^+)$, etc.. Since we are interested in the dynamics of the superconducting gap, we multiply both sides of the linearized equations of motion by the coupling constant after the quench, v_f, and then integrate over ε. By

substituting the gap equation, Eq. (3.47), and using the fact that S_∞^z is odd in ε due to the particle-hole symmetry, we obtain the equations of motion for the variation of the gap in the Laplace space. Using the following notation $\langle \ldots \rangle = v_f \int d\varepsilon \, (\ldots)$, we have

$$\mathrm{Im}\delta\Delta\,(s) = \left\langle \frac{s f_0'' + \dot{f}_0''}{s^2 + 4E_\infty^2} \right\rangle, \tag{3.55a}$$

$$\mathrm{Re}\delta\Delta\,(s) = \frac{1}{s}\delta\Delta_0 - \frac{1}{s}\frac{I\,(s)}{\Phi_\infty\,(s)}, \tag{3.55b}$$

where $I\,(s) = \left\langle \frac{2\varepsilon\left[s f_0'' + \dot{f}_0''\right]}{s^2 + 4E_\infty^2} \right\rangle$ is given by the initial conditions, and

$$\Phi_\infty\,(s) = \left(s^2 + 4\Delta_\infty^2\right) \left\langle \frac{-S_\infty^z/\varepsilon}{s^2 + 4E_\infty^2} \right\rangle, \tag{3.56}$$

which contains only the information about the long time asymptotic state. Eq. (3.55a) is automatically satisfied by choosing the initial value of the gap to be real. From Eq. (3.50), it is clear that for real initial gap, $f_0'' = 0$ and $\dot{f}_0''$ is odd in ε, which makes the right hand side of Eq. (3.55a) automatically zero. This is just a consequence of the fact that the interaction quench does not change the phase of the superconducting gap. Therefore, $\delta\Delta\,(s) = \mathrm{Re}\delta\Delta\,(s)$ and the dynamics of the gap is then described solely by Eq. (3.55b).

3.4.1 Initial conditions

The initial conditions are determined by the equilibrium states before the quench, i.e. with pairing interaction v_i. The pseudospins are parallel to the effective magnetic field, $\mathbf{B_k}\,(t=0) = 2\,(\Delta_i, 0, -\varepsilon_\mathbf{k})$, with the following configuration:

$$S_i^x = \frac{\Delta_i}{2\sqrt{\varepsilon^2 + \Delta_i^2}}, \tag{3.57a}$$

$$S_i^y = 0, \tag{3.57b}$$

$$S_i^z = \frac{-\varepsilon}{2\sqrt{\varepsilon^2 + \Delta_i^2}}. \tag{3.57c}$$

The initial conditions for the linearized equations of motion, Eq. (3.50), are obtained based on the linearization, Eq. (3.45).

$$f_0' = \frac{\Delta_i}{2\sqrt{\varepsilon^2+\Delta_i^2}} - S_\infty^x, \tag{3.58a}$$

$$f_0'' = 0, \tag{3.58b}$$

$$g_0 = \frac{-\varepsilon}{2\sqrt{\varepsilon^2+\Delta_i^2}} - S_\infty^z, \tag{3.58c}$$

$$\dot{f_0}'' = -2\varepsilon f_0' - 2\Delta_\infty g_0 - 2S_\infty^z \delta\Delta_0. \tag{3.58d}$$

We used the equations of motion (Eq. (3.50)) to obtain the last equation for $\dot{f_0}''$. After the quench, the pairing interaction becomes v_f. Therefore, the initial value for the post-quench dynamics of the gap is not Δ_i, but determined by the following gap equation:

$$\Delta\left(t=0\right) = v_f \int d\varepsilon S_i^x = v_f \int d\varepsilon \frac{\Delta_i}{2\sqrt{\varepsilon^2+\Delta_i^2}}. \tag{3.59}$$

The above gap equation reflects the fact that the quench only changes the pairing interaction but not the underlying electronic states at $t = 0$. The initial value of the gap variation is therefore given by

$$\delta\Delta_0 = v_f \int d\varepsilon \frac{\Delta_i}{2\sqrt{\varepsilon^2+\Delta_i^2}} - \Delta_\infty = \frac{v_f}{v_i}\Delta_i - \Delta_\infty \tag{3.60}$$

With these initial values, we arrive at the following expression for the initial condition in Eq. (3.55b):

$$\begin{aligned} I(s) &= \left\langle \frac{2\varepsilon\left[sf_0'' + \dot{f}_0''\right]}{s^2+4E_\infty^2} \right\rangle \\ &= \left\langle \frac{4\varepsilon^2\left(-S_\infty^z/\varepsilon\right)\delta\Delta_0}{s^2+4E_\infty^2} \right\rangle - \left\langle \frac{4\varepsilon^2}{s^2+4E_\infty^2}\frac{\Delta_i-\Delta_\infty}{2\sqrt{\varepsilon^2+\Delta_i^2}} \right\rangle \\ &= \delta\Delta_0\left[\langle -S_\infty^z/\varepsilon\rangle - \left\langle \frac{s^2+4\Delta_\infty^2}{s^2+4E_\infty^2}\left(-S_\infty^z/\varepsilon\right)\right\rangle\right] \\ &\quad -\left(\Delta_i-\Delta_\infty\right)\left[\langle -S_i^z/\varepsilon\rangle - \left\langle \frac{s^2+4\Delta_\infty^2}{s^2+4E_\infty^2}\left(-S_i^z/\varepsilon\right)\right\rangle\right]. \end{aligned} \tag{3.61}$$

Due to the stationary condition: $-\frac{S_{i/\infty}^z}{\varepsilon} = \frac{S_{i/\infty}^x}{\Delta_{i/\infty}}$ and the gap equation, we have

$$\langle -S_\infty^z/\varepsilon\rangle = \langle S_\infty^x/\Delta_\infty\rangle = 1, \tag{3.62a}$$

$$\langle -S_i^z/\varepsilon\rangle = \langle S_i^x/\Delta_i\rangle = \frac{v_f}{v_i}. \tag{3.62b}$$

Substituting to the expression for $I(s)$, we have

$$I(s) = \delta\Delta_0\left[1-\Phi_\infty(s)\right] - \left(\Delta_i-\Delta_\infty\right)\left[\frac{v_f}{v_i} - \Phi_i(s)\right], \tag{3.63}$$

where

$$\Phi_{i/\infty}(s) = \left\langle \frac{s^2+4\Delta_\infty^2}{\left(s^2+4E_\infty^2\right)2\sqrt{\varepsilon^2+\Delta_{i/f}^2}} \right\rangle. \tag{3.64}$$

But in order to evaluate $I(s)$, we need to find the expression for $-S_\infty^z/\varepsilon$ and calculate $\Phi_{i/\infty}(s)$.

3.4.2 Long-time asymptotic states

To proceed, we use the gap equation as a constraint and propose an ansatz for the asymptotic states of the pseudospins S_∞^x and S_∞^z. The ansatz is motivated by the fact that the gap equation is always satisfied regardless of whether the system is in or out

of equilibrium. In equilibrium, the gap equation requires:

$$1 = v_f \int d\varepsilon \frac{n_{\text{eq}}\left(\sqrt{\varepsilon^2+\Delta_f^2}\right)}{2\sqrt{\varepsilon^2+\Delta_f^2}}, \tag{3.65}$$

where $n_{\text{eq}}(x) = 1 - 2n_{\text{F}}(x) = \tanh\left(\frac{x}{2T}\right) \overset{T=0}{\to} \text{sgn}(x)$ is the equilibrium quasiparticle distribution function. The stationary state of the pseudospins also satisfies the same constraint, $1 = v_f \int d\varepsilon \frac{-S_\infty^z}{\varepsilon}$. We rewrite this asymptotic gap equation in a similar fashion to the equilibrium counterpart:

$$1 = v_f \int d\varepsilon \frac{n_{\text{eff}}\left(\sqrt{\varepsilon^2+\Delta_\infty^2}\right)}{2\sqrt{\varepsilon^2+\Delta_\infty^2}}, \tag{3.66}$$

where $n_{\text{eff}}(x)$ is the effective quasiparticle distribution function. As shown in the previous subsection, the quasiparticle distribution function is intact under the time evolution of the BCS Hamiltonian. Therefore, it is only an effective distribution imposed by the gap equation after projecting the persistent oscillatory pseudospins onto the x-z plane. Comparing Eq. (3.65) with Eq. (3.66), we propose the following ansatz for the effective distribution:

$$n_{\text{eff}}\left(\sqrt{\varepsilon^2+\Delta_\infty^2}\right) = \sqrt{\frac{\varepsilon^2+\Delta_\infty^2}{\varepsilon^2+\Delta_f^2}}. \tag{3.67}$$

Consequently, long-time asymptotic states of the pseudospins are given by

$$\frac{S_\infty^x}{\Delta_\infty} = -\frac{S_\infty^z}{\varepsilon} = \frac{n_{\text{eff}}\left(\sqrt{\varepsilon^2+\Delta_\infty^2}\right)}{2\sqrt{\varepsilon^2+\Delta_\infty^2}} = \frac{1}{2\sqrt{\varepsilon^2+\Delta_f^2}}. \tag{3.68}$$

With the long-time asymptotic states, we obtain the following expression for $\Phi_{i/\infty}(s)$:

$$\Phi_{i/\infty}(s) = v_f \frac{\sqrt{s^2+4\Delta_\infty^2}\arccos\left(\sqrt{\frac{s^2+4\Delta_\infty^2}{4\Delta_{i/f}^2}}\right)}{\sqrt{4\left(\Delta_{i/f}^2-\Delta_\infty^2\right)-s^2}}. \tag{3.69}$$

Substituting to Eq. (3.63) and (3.55b), we obtain the solution for the variation of the

gap in Laplace space:

$$\delta\Delta\left(s\right)=-\frac{\left(1-\frac{v_f}{v_i}\right)\Delta_\infty}{s}\frac{1}{\Phi_\infty\left(s\right)}+\frac{\left(\Delta_i-\Delta_\infty\right)}{s}\frac{\Phi_i\left(s\right)}{\Phi_\infty\left(s\right)}. \tag{3.70}$$

Since we expand the equations of motion around the long-time asymptotic value, the variation of the gap at $t\to\infty$ must vanish. Therefore, based on the final value theorem in Laplace analysis, we have the following self-consistency condition:

$$\lim_{t\to\infty}\delta\Delta\left(t\right)=\lim_{s\to0}\left[s\delta\Delta\left(s\right)\right]=0. \tag{3.71}$$

From Eq. (3.70), we have

$$\lim_{s\to0}\left[s\delta\Delta\left(s\right)\right]=-\frac{\sqrt{\Delta_f^2-\Delta_\infty^2}}{\arccos\left(\frac{\Delta_\infty}{\Delta_f}\right)}\left[\ln\left(\frac{\Delta_i}{\Delta_f}\right)-\left(1-\frac{\Delta_\infty}{\Delta_i}\right)\frac{\arccos\left(\frac{\Delta_\infty}{\Delta_i}\right)}{\sqrt{1-\frac{\Delta_\infty^2}{\Delta_i^2}}}\right]. \tag{3.72}$$

As a result, the asymptotic value of the gap must satisfy the following self-consistency condition:

$$\ln\left(\frac{\Delta_i}{\Delta_f}\right)-\left(1-\frac{\Delta_\infty}{\Delta_i}\right)\frac{\arccos\left(\frac{\Delta_\infty}{\Delta_i}\right)}{\sqrt{1-\frac{\Delta_\infty^2}{\Delta_i^2}}}=0. \tag{3.73}$$

This is the exact same equation for finding the roots of the Lax vector square, $\mathbf{L}^2\left(s\right)=0$, from Eq. (3.42). It is clear from this self-consistency condition that the upper bound of the quench parameter is $\frac{\Delta_i}{\Delta_f}=e^{\frac{\pi}{2}}$, beyond which the asymptotic value of the gap becomes zero, $\Delta_\infty=0$. We compare the asymptotic value of the gap as a function of the quench parameter calculated from the self-consistency condition with the same quantity calculated from the Lax vector in Fig. 3.5. According to the Lax root calculation, there is also a lower bound for the quench parameter, $\frac{\Delta_i}{\Delta_f}=e^{-\frac{\pi}{2}}$, below with the gap exhibits undamped persistent oscillation. However, the average value of the gap still follows the asymptotic gap value calculated from the self-consistency condition.

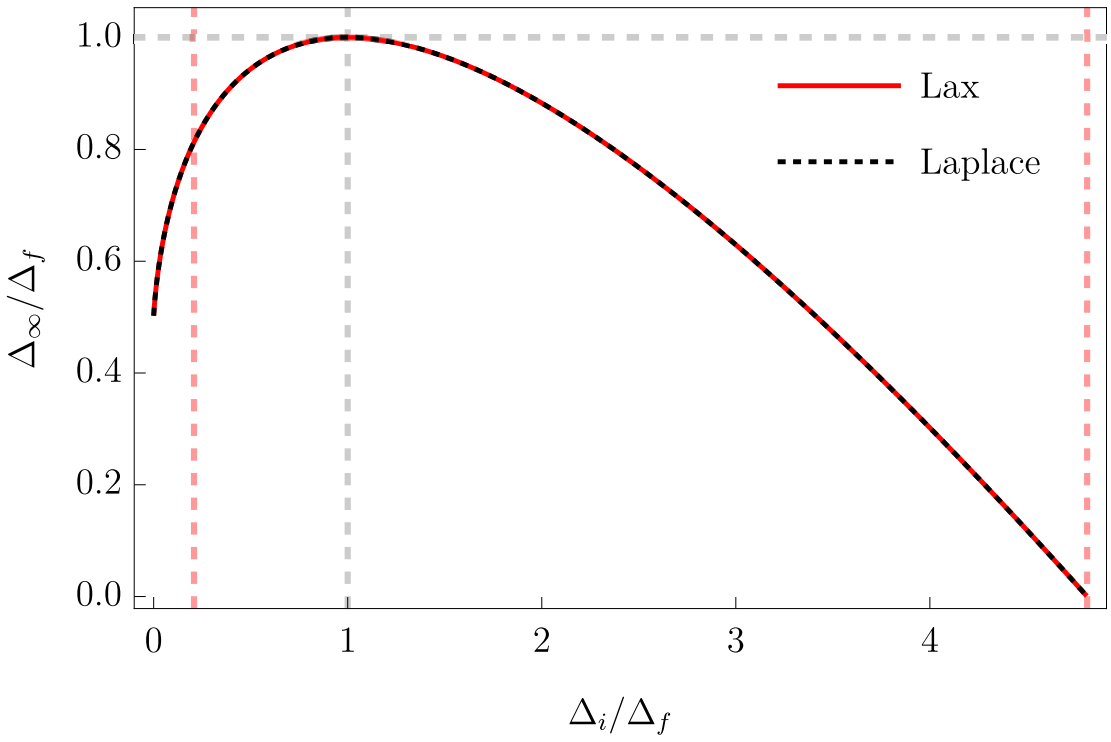

Figure 3.5: Δ_∞ as a function of the quench parameter Δ_i/Δ_f, the red dash lines are the lower and upper bounds for the damped oscillatory dynamics for the superconducting gap obtained from the roots of the Lax operator. (Figure taken from Ref. [29].)

3.4.3 Long-time dynamics of the gap

With the solution of the linearized equations of motion in the Laplace space (Eq. (3.70)), the long-time dynamics of the gap in the weak quench limit is therefore given by the inverse Laplace transformation:

$$y(t)=\frac{1}{2\pi i}\int_{\sigma-i\infty}^{\sigma+i\infty}y(s)\,e^{st}ds \tag{3.74}$$

where σ is a real number that is larger than the real parts of all the singularities of $y(s)$. An integral of this kind is called a Bromwich integral, which can be evaluated via the Cauchy's integral formula. In order to do that, we need to first study the analytic properties of the integrand.

From Eq. (3.70), it is clear that the analytic properties of $\delta\Delta(s)$ are solely determined by $\Phi_{i/\infty}(s)$. For convenience, we use $z=\frac{s}{2\Delta_\infty}$ as the complex variable in the Laplace space, which leads to

$$\Phi_{i/\infty}(z)=v_f\frac{\sqrt{\frac{z^2+1}{\tilde{\Delta}_{i/f}^2}}\arccos\left(\sqrt{\frac{z^2+1}{\tilde{\Delta}_{i/f}^2}}\right)}{\sqrt{1-\frac{z^2+1}{\tilde{\Delta}_{i/f}^2}}}, \tag{3.75}$$

where $\tilde{\Delta}_{i/f}=\Delta_{i/f}/\Delta_\infty$. The only non-analyticity of $\Phi_{i/\infty}(z)$ comes from $\sqrt{z^2+1}$, which has two branch cuts located at $(-i\infty,\,-i)$ and $(i,\,i\infty)$. The additional branch cut of $\arccos\left(\sqrt{\frac{z^2+1}{\tilde{\Delta}_{i/f}^2}}\right)$ at $z^2=\tilde{\Delta}_{i/f}^2-1$ is annihilated by the same branch cut of $\sqrt{1-\frac{z^2+1}{\tilde{\Delta}_{i/f}^2}}$ in the denominator. To show this, we perform the the expansion in the neighborhood of $\zeta=\frac{z^2+1}{\tilde{\Delta}_{i/f}^2}=1+\epsilon e^{i\theta}$, with $\epsilon\ll 1$:

$$\frac{\arccos\left(\sqrt{\zeta}\right)}{\sqrt{1-\zeta}}=\frac{\frac{1}{i}\ln\left(\sqrt{\zeta}+i\sqrt{1-\zeta}\right)}{\sqrt{1-\zeta}}=\frac{\frac{1}{i}\ln\left(1+\frac{\epsilon}{2}e^{i\theta}+i\sqrt{-\epsilon e^{i\theta}}\right)}{\sqrt{-\epsilon e^{i\theta}}}=\frac{\sqrt{\epsilon}e^{i\frac{\theta+\pi}{2}}}{\sqrt{\epsilon}e^{i\frac{\theta+\pi}{2}}}+\mathcal{O}(\epsilon). \tag{3.76}$$

At the neighborhood of $\zeta=1$, as θ goes from 0 to 2π, the value of $\frac{\arccos\left(\sqrt{\zeta}\right)}{\sqrt{1-\zeta}}$ does not change. Therefore, $z^2=\tilde{\Delta}_{i/f}^2-1$ is not a branch point of $\Phi_{i/\infty}(z)$ even though it is a

branch point of $\arccos\left(\sqrt{\frac{z^2+1}{\tilde{\Delta}_{i/f}^2}}\right)$ and $\sqrt{1-\frac{z^2+1}{\tilde{\Delta}_{i/f}^2}}$ individually.

Because the non-analyticity only occurs at the imaginary axis, using Cauchy's integral formula, the integration contour becomes the grey curve shown in Fig. 3.6. Because of the initial value theorem, i.e. $\lim_{s\to\infty} s\delta\Delta(s) = \delta\Delta_0$, $\delta\Delta(s)$ goes to zero as $s \to \infty$. Therefore, the Bromwich integral becomes

$$\begin{aligned}\delta\Delta(t) &= \frac{1}{2\pi i}\int_{\sigma-i\infty}^{\sigma+i\infty} \delta\Delta(s)\, e^{st} ds \\ &= -\frac{1}{2\pi i}\left\{\int_{0^+ +i\infty}^{0^+ +2i\Delta_\infty} + \int_{0^- +2i\Delta_\infty}^{0^- +i\infty} + \int_{0^- -i\infty}^{0^- -2i\Delta_\infty} + \int_{0^+ -2i\Delta_\infty}^{0^+ -i\infty}\right\} \delta\Delta(s)\, e^{st} ds \\ &= \frac{2}{\pi}\int_{0^+ +2i\Delta_\infty}^{0^+ +i\infty} \mathrm{Im}\left[s\delta\Delta(s)\right] \frac{\cosh(st)}{s} ds, \end{aligned} \tag{3.77}$$

where the last equality is due to the fact that $\delta\Delta(s) = -\delta\Delta(-s)$.

After changing the complex variable to z, we rotate to the imaginary axis by letting $z = iy$. Then,

$$\delta\Delta(t) = \frac{2}{\pi}\int_1^\infty \mathrm{Im}\left[iy\delta\Delta(y)\right] \frac{\cos(2\Delta_\infty yt)}{y} dy \tag{3.78}$$

The above integral is dominated by the contribution from the vicinity of the branch point, i.e. $y \to 1$, as for large y, $\frac{\cos(2\Delta_\infty yt)}{y}$ goes to zero while $\mathrm{Im}\left[iy\delta\Delta(y)\right]$ converges to a constant. The asymptotic behavior of $\Phi_{i/\infty}(y)$ around $y \gtrsim 1$ is given by

$$\Phi_{i/\infty}(y) = v_f \frac{\sqrt{\frac{1-y^2}{\tilde{\Delta}_{i/f}^2}}\arccos\left(\sqrt{\frac{1-y^2}{\tilde{\Delta}_{i/f}^2}}\right)}{\sqrt{1-\frac{1-y^2}{\tilde{\Delta}_{i/f}^2}}} \simeq i\frac{v_f\pi}{\left|\tilde{\Delta}_{i/f}\right|}\sqrt{\frac{y-1}{2}}. \tag{3.79}$$

Substituting to Eq. (3.70), we obtain the following asymptotics

$$\mathrm{Im}\left[iy\delta\Delta(y)\right] \simeq \frac{\left(\frac{1}{v_f}-\frac{1}{v_i}\right)|\Delta_f|}{\pi}\sqrt{\frac{2}{y-1}}. \tag{3.80}$$

At the long-time limit, where $2\Delta_\infty t \gg 1$, the inverse Laplace transformation yields to

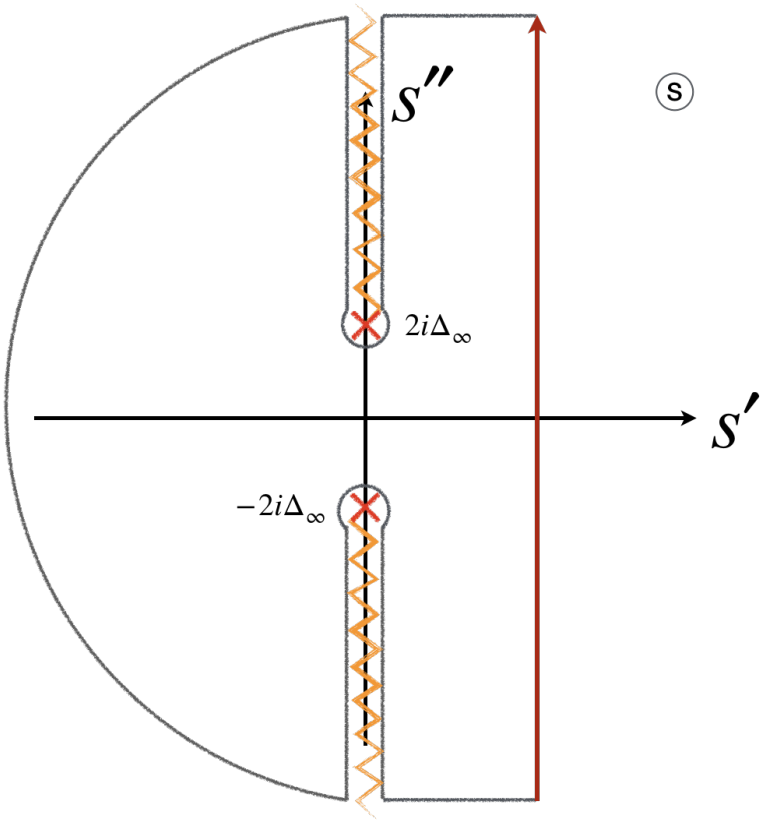

Figure 3.6: Integration contour in complex Laplace space.

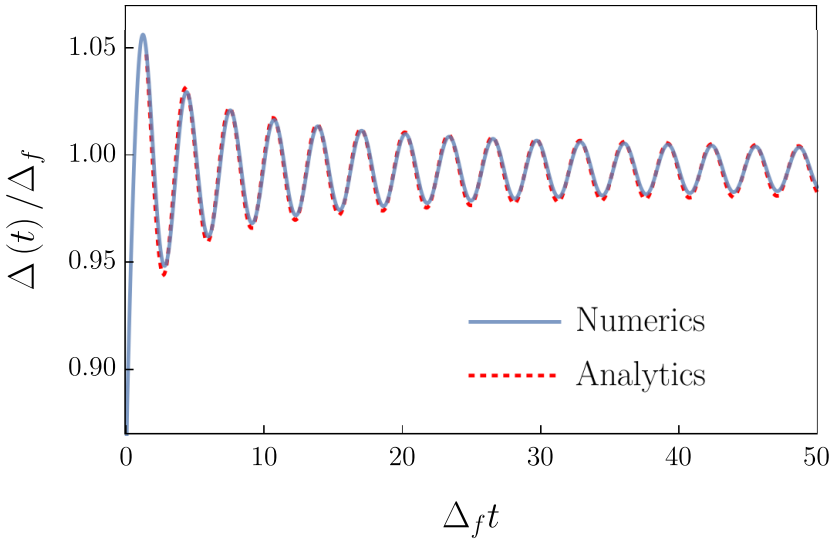

Figure 3.7: Comparison between numerical result of the exact equations of motion with the analytic result extracted from the Laplace analysis on the linearized equations of motion. $\Delta_i/\Delta_f = 0.8$ for both the numerics and analytics.

the following closed-form:

$$\delta\Delta(t) \simeq \left(\frac{2}{\pi}\right)^{3/2} \Delta_f \ln\left(\frac{\Delta_i}{\Delta_f}\right) \frac{\cos\left(2\Delta_\infty t + \frac{\pi}{4}\right)}{\sqrt{2\Delta_\infty t}}. \tag{3.81}$$

As a result, the long-time asymptotic dynamics of the gap is given by

$$\Delta(t) \simeq \Delta_\infty + \left(\frac{2}{\pi}\right)^{3/2} \Delta_f \ln\left(\frac{\Delta_i}{\Delta_f}\right) \frac{\cos\left(2\Delta_\infty t + \frac{\pi}{4}\right)}{\sqrt{2\Delta_\infty t}}. \tag{3.82}$$

Comparing with the previous exact solution, Eq. (3.43), it is self-evident that the perturbative solution fully captures the dynamics of the gap at the long-time limit. We also compare the asymptotic result, Eq. (3.82), with the numerical solution of the exact equations of motion, Eq. (3.26), in Fig. 3.7. The two curves matches perfectly. In the next chapter, we will extend this perturbative approach to multi-band superconductors.

Chapter 4

Post-quench gap dynamics of two-band superconductors

This chapter partially reproduces content of a preprint posted on arXiv:1908.06125 "Post-quench gap dynamics of two-band superconductors", Tianbai Cui, Michael Schütt, Peter P. Orth, and Rafael M. Fernandes.

4.1 Introduction

In the previous section, we established the theoretical framework for the study of non-equilibrium superconductivity. For simplicity, we were restricted to conventional superconductors where the low-energy effective theory is approximated by a single conduction band under the attractive electron-electron interaction mediated by electron-phonon coupling. From this study, we learned the oscillatory and damping characteristics of the transient dynamics of the conventional superconducting gap. More fascinating questions are related to what we can learn about the non-equilibrium phenomena of unconventional superconductors. For example, are unconventional superconductors share the same oscillatory and damping characteristics out of equilibrium as conventional superconductors?

Unconventional superconductors distinguishes from the conventional ones on the pairing mechanism. Until now, there is still no consensus on the pairing mechanism on any of the unconventional superconducting materials, except the fact that it is not

mediated by electron-phonon coupling. Due to the different pairing mechanism, unconventional superconductor can exhibit different gap symmetries depending on the shape of the Fermi surface. For example, in the cuprate family of unconventional superconductors, the sign-changing superconducting gap has 4-fold rotational symmetry, which is called the d-wave superconducting gap. Because different electronics states experience different values of the gap, it is more difficult to maintain coherence for the out of equilibrium dynamics between different momentum states, leading to much faster damping of the gap oscillation comparing to the conventional case[83]. Other families of unconventional superconductors, such as iron-pnictides [84], perovskite [85, 86] and heavy fermions [87, 88, 89], have multiple bands crossing the Fermi level. As a consequence, when multiple electronic bands involve in the superconducting condensate, the superconducting gap can develop different values in different bands. In fact, the pairing channel of electrons can take advantage of the repulsive electron-electron interaction between different bands by adjusting the relative gap signs between different bands without introducing any nodes[90]. Note that the multi-band superconductivity can also arise in conventional systems where pairing is phonon mediated, e.g. MgB_2. In this case, there is no relative sign change between the superconducting gaps in different bands. The non-equilibrium properties of superconductors with multiple bands is the focus of this chapter. Previous numerical studies show multiply frequencies in the gap oscillations, as expected due to the multi-band nature of such systems[81, 91]. However, their exact interplay, the resulting relaxation behaviors as well as the dependence on the quenching strength require insights from the analytical results. To address this, we extend the perturbative approach introduced in the previous chapter to multi-band systems.

4.2 Superconductivity in multi-band systems

Similar to the single-band counterpart as discussed in the previous chapter, the BCS Hamiltonian for multi-band systems has the same form but now with an extra band index:

$$H_{\mathrm{BCS}} = \sum_{\mathbf{k},\sigma,\alpha} \varepsilon_{\mathbf{k},\alpha} c^{\dagger}_{\mathbf{k},\sigma,\alpha} c_{\mathbf{k},\sigma,\alpha} + \frac{1}{N} \sum_{\mathbf{k},\mathbf{p},\alpha,\beta} V_{\alpha\beta} c^{\dagger}_{\mathbf{k},\uparrow,\alpha} c^{\dagger}_{-\mathbf{k},\downarrow,\alpha} c_{-\mathbf{p},\downarrow,\beta} c_{\mathbf{p},\uparrow,\beta}, \tag{4.1}$$

where α, $\beta \in \{1, 2, \ldots, \}$ are the band indices, $\varepsilon_{\mathbf{k},\alpha}$ is the electronic dispersion near the Fermi level in band α (including the chemical potential), and $V_{\alpha\beta}$ is the effective pairing interaction between band α and band β. The interaction constants $V_{\alpha\beta}$ are positive (negative) if the interaction is repulsive (attractive). For convenience, we will restrict the band indices to be α, $\beta \in \{1, 2\}$, and consider two-band systems.

In two-band systems, different bands develop different values of the superconducting gap, depending on the values of the intra-band interactions, V_{11} and V_{22}, and the inter-band interactions, V_{12} and V_{21} as well as the density of states of the two bands at the Fermi level, $\mathcal{N}_\alpha$. We assume that the two bands have the same intra-band electronic interactions such that $V_{11} = V_{22} \equiv U$; by definition, $V_{12} = V_{21} \equiv V$. Due to the different density of states $\mathcal{N}_1 \neq \mathcal{N}_2$, electrons in different bands experience different effective interaction strengths. The BCS gap equation is therefore band-dependent:

$$\Delta_\alpha = \Delta'_\alpha + i\Delta''_\alpha = -\frac{1}{N}\sum_{\mathbf{p},\beta} V_{\alpha\beta} \left\langle c_{-\mathbf{p},\downarrow,\beta} c_{\mathbf{p},\uparrow,\beta} \right\rangle \tag{4.2}$$

Going from summation over momenta to integrations over energy using the density of states, we write the equilibrium BCS gap equations explicitly in matrix form in the band-space.

$$\begin{pmatrix} \Delta_1 \\ \Delta_2 \end{pmatrix} = \hat{\gamma} v \begin{pmatrix} \int_{-\Lambda}^{\Lambda} d\varepsilon \frac{\Delta_1}{2E_1} \tanh\left(\frac{E_1}{2T}\right) \\ \int_{-\Lambda}^{\Lambda} d\varepsilon \frac{\Delta_2}{2E_2} \tanh\left(\frac{E_2}{2T}\right) \end{pmatrix} \tag{4.3}$$

where Λ is a high-energy cutoff and

$$\hat{\gamma} = \begin{pmatrix} r & -\eta \\ -1 & r\eta \end{pmatrix} \tag{4.4}$$

with $\eta = \mathcal{N}_2/\mathcal{N}_1$ being the ratio of the density of states of the two bands, $E_\alpha = \sqrt{\varepsilon^2 + \Delta_\alpha^2}$ is the Bogoliubov quasiparticle dispersion in band α and T is the temperature of the system. In the following, we restrict our analysis to the $T = 0$ ground state as the initial pre-quench state of the system. We have also defined the dimensionless inter-band interaction coupling constant $v = V\mathcal{N}_1$, and the dimensionless ratio $r = -U/V$ between intra-band and inter-band interactions. Here, we include the minus sign in the definition, as we will assume that $U < 0$ is negative, corresponding to attractive

intra-band interaction.

Note that the ratio of the density of states in the two bands, $\eta = \mathcal{N}_2/\mathcal{N}_1$, determines the relative sizes of the superconducting gaps of the two bands. If the two bands have the same density of states near the Fermi energy, i.e. $\eta = 1$, the matrix $\hat{\gamma}$ becomes symmetric. Therefore, the gap equations are solved by $\Delta_1 = -\Delta_2$ for repulsive inter-band interaction ($v > 0$), corresponding to s^{+-} pairing, and $\Delta_1 = \Delta_2$ for attractive inter-band interaction ($v < 0$), corresponding to s^{++} pairing. In this paper, we will focus on the case with $\eta \neq 1$, in which case the amplitude of the two gaps is different in equilibrium $|\Delta_1| \neq |\Delta_2|$ and the multi-band nature of the system has a pronounced imprint on the non-equilibrium dynamics of the superconducting gap.

It is convenient to use the pseudospin formalism [75] to study the non-equilibrium dynamics of the superconducting state. In the mean-field approach, which is exact in the BCS regime we consider here, the BCS Hamiltonian can be described by pseudospins exposed to an effective magnetic field:

$$H_{\mathrm{BCS}} = -\sum_{\mathbf{k},\alpha} \mathbf{B}_{\mathbf{k},\alpha} \cdot \hat{\mathbf{S}}_{\mathbf{k},\alpha} + \mathrm{const.} \tag{4.5}$$

where $\mathbf{B}_{\mathbf{k},\alpha} = 2\left(\Delta_\alpha^{'}, -\Delta_\alpha^{''}, -\varepsilon_{\mathbf{k},\alpha}\right)$ and

$$\hat{S}^{-}_{\mathbf{k},\alpha} = c_{-\mathbf{k},\downarrow,\alpha} c_{\mathbf{k},\uparrow,\alpha} \tag{4.6a}$$

$$\hat{S}^{+}_{\mathbf{k},\alpha} = c^{\dagger}_{\mathbf{k},\uparrow,\alpha} c^{\dagger}_{-\mathbf{k},\downarrow,\alpha} \tag{4.6b}$$

$$\hat{S}^{z}_{\mathbf{k},\alpha} = \frac{1}{2}\left(c^{\dagger}_{\mathbf{k},\uparrow,\alpha} c_{\mathbf{k},\uparrow,\alpha} + c^{\dagger}_{-\mathbf{k},\downarrow,\alpha} c_{-\mathbf{k},\downarrow,\alpha} - 1\right) \tag{4.6c}$$

The constant term contributes to the ground state energy, which will be ignored because it is not relevant to the dynamics out of equilibrium. The mapping between pseudospins and electronic pair operators is the same as the mapping in the single-band systems introduced in Chapter 3, expect now with an extra band index. The anti-commutation relation between the electronic operators ensures the spin commutation relation between $\hat{\mathbf{S}}_{\mathbf{k},\alpha}$. Notice that despite the simple form of the pseudospin Hamiltonian, the effective magnetic field is self-consistently determined by the pseudospins collectively via the gap

equation:

$$\Delta_\alpha = -\frac{1}{N}\sum_{\mathbf{k},\beta} V_{\alpha\beta} S^-_{\mathbf{k},\beta} \tag{4.7}$$

where $S^-_{\mathbf{k},\alpha} = \left\langle \hat{S}^-_{\mathbf{k},\alpha} \right\rangle = \langle c_{-\mathbf{k},\downarrow,\alpha} c_{\mathbf{k},\uparrow,\alpha} \rangle$. In equilibrium, the pseudospins are parallel to the effective magnetic field. For convenience, we choose to work in a gauge where both the gaps are real, i.e. $S^y_{\mathbf{k},\alpha} = 0$.

In equilibrium, the pseudospins are parallel to the effective magnetic field. It is convenient to work in a gauge where both the gaps are real. Then the expectation values of the pseudo-spins at temperature T are given by

$$S^x_{\mathbf{k},\alpha} = \frac{\Delta_\alpha}{2E_\alpha} \tanh\left(\frac{E_\alpha}{2T}\right) \tag{4.8a}$$

$$S^y_{\mathbf{k},\alpha} = 0 \tag{4.8b}$$

$$S^z_{\mathbf{k},\alpha} = \frac{-\varepsilon_{\mathbf{k}}}{2E_\alpha} \tanh\left(\frac{E_\alpha}{2T}\right) . \tag{4.8c}$$

Note that the length of the pseudospins in equilibrium is determined by the Fermi-Dirac distribution, n_{F}, of the Bogoliubov quasiparticles, i.e. $|\mathbf{S}_{\mathbf{k},\alpha}| = \frac{1}{2} - n_{\mathrm{F}}$. As mentioned above, we will focus hereafter on initial pre-quench states at zero temperature ($T = 0$).

4.3 Equations of motions and numerical results

The system is driven out of equilibrium by an interaction quench protocol, where the electron-electron interaction is suddenly changed. Specifically, interaction quench we consider here is a sudden change of the inter-band coupling $v_i \to v_f$ while keeping the ratio between intra- and inter-band interaction, r, and the ratio between the density of states, η, unchanged. The subscript i and f denote the initial and final value of the dimensionless coupling. Here we only quench v while keeping r and η unchanged in order to constrain the parameter space. Generally, one can quench both the intra- and inter-band interactions independently. However, this will not lead to any qualitative changes to the non-equilibrium dynamics. Nevertheless, it is simply a quantitatively different way to prepare the initial conditions. If $\eta = 1$, however, one of the bands can be viewed as an exact copy of the other. The quench dynamics is therefore described

faithfully by the exact solution of the single-band BCS model.[92, 93, 94, 20, 95].

If the two bands have different density of states, i.e. $\eta \neq 1$, the quench dynamics is intrinsically different from the single-band systems. In the pseudospins formalism, the superconducting gap determines the intrinsic frequency of the pseudospin processions. Therefore, once the two bands have different density of states, they develop different values of the gap, leading to two distinct intrinsic frequencies. In addition, the gap also serves as the effective magnetic field that drives the procession motion. Through the inter-band interaction, each band experiences an oscillating magnetic field with the intrinsic frequency of the other band. Hence, the dephasing of the pseudospin oscillations in multi-band systems is fundamentally different from single-band systems. The dynamics is described by the two sets of equations of motion for the two bands, which are derived from Eq. (4.5) in terms of expectation values of the pseudo-spins operators,

$$\frac{d}{dt}\mathbf{S}_{\mathbf{k},\alpha}(t) = -\mathbf{B}_{\mathbf{k},\alpha}(t) \times \mathbf{S}_{\mathbf{k},\alpha}(t) \tag{4.9}$$

which are similar to the one-band case, but now with an extra band index α. More importantly, the pseudospin dynamics in the two bands are coupled via the gap equations (Eq. (4.10)) with a time-dependent interaction $v(t) = v_i\theta(-t) + v_f\theta(t)$.

$$\Delta_\alpha(t) = v(t)\sum_\beta \gamma_{\alpha\beta}\int d\varepsilon S^-_\beta(\varepsilon, t) \tag{4.10}$$

The equations of motion for the pseudo-spins (Eq. (4.9)) and the time-dependent gap equation (Eq. (4.10)) solve the quench dynamics of the two-band superconductors. The numerical results are shown in Fig. 4.1. In contrast to the single-band BCS model, There are two important qualitative features that emerge in the two-band case: first, the gap oscillations are characterized by two frequencies, corresponding to the steady-state values $\Delta_{1,\infty}$ and $\Delta_{2,\infty}$. This phenomenon has been described previously in numerical studies of two-band (multi-band) superconductors exposed to terahertz laser pulses [81, 96, 91] Second, the algebraic damping of the gap oscillations occurs more rapidly than in the single-band case. As opposed to the $t^{-1/2}$ damping in the single band case, the damping is characterized by $t^{-3/2}$ in two-band systems as shown in Fig. 4.1(D) and (H).

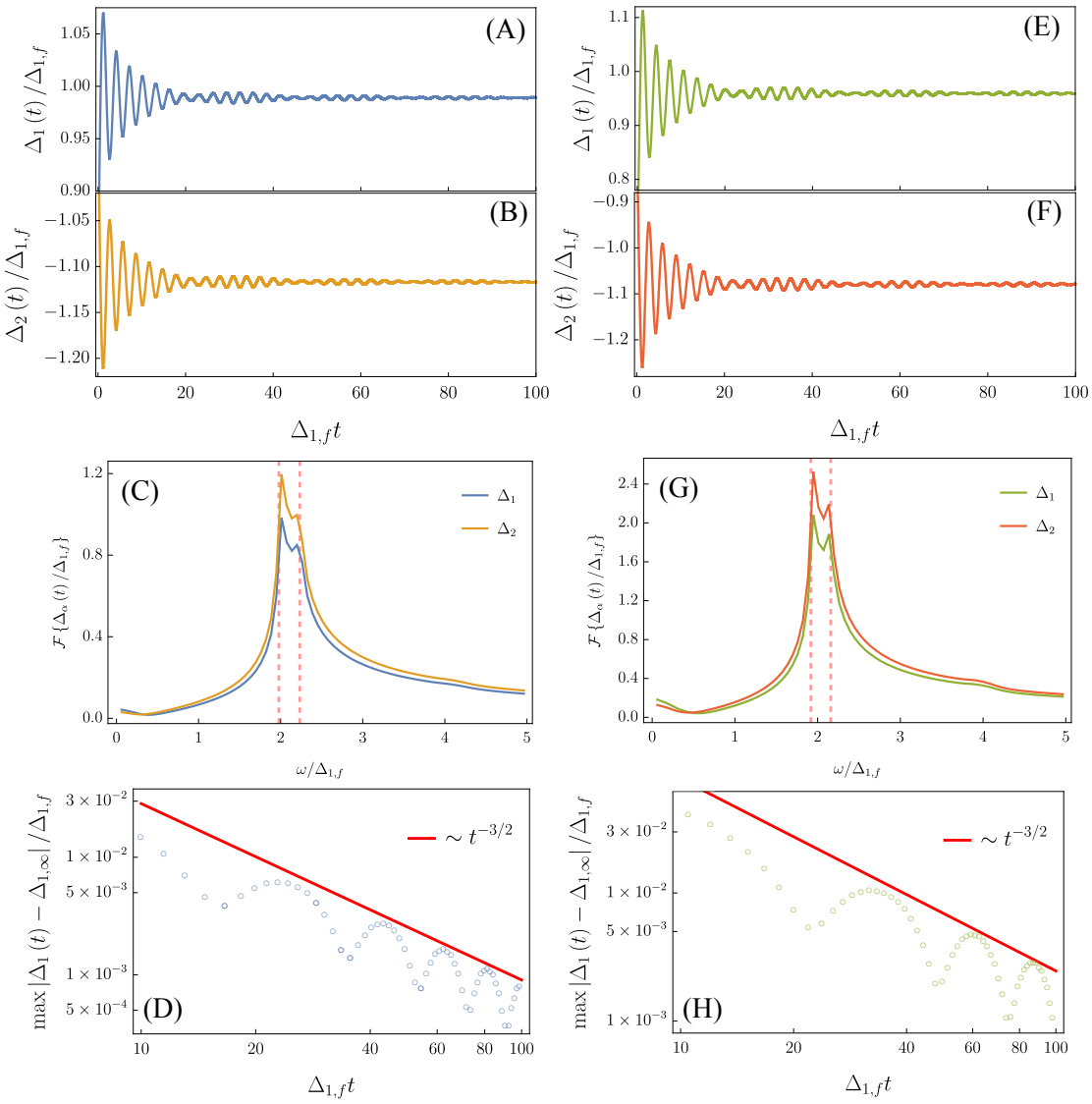

Figure 4.1: Gap oscillations in two-band superconductors. (A)-(D) are the results for an interaction quench from $v_i = 0.19$ to $v_f = 0.2$. (E)-(H) correspond to interaction quench from $v_i = 0.18$ to $v_f = 0.2$. (C) and (G) are the Fourier spectrums of the gap oscillations. (D) and (H) shown the $t^{-3/2}$ damping of the gap oscillations in a log-log plot. The ratio of the density of states between the two bands is $\eta = 0.8$ in these calculations.

This behavior seems insensitive to the actual value of r. In Fig. 4.2, we compare the behavior of $\Delta_1(t)$ for the cases in which $r = 0.5$ and $r = 0$. The other parameter used were $v_i = 0.19$ and $v_f = 0.2$.

4.4 Long-time asymptotic gap dynamics

In order to gain more insights on the transient dynamics of the superconducting gap in two-band systems, it is instructive to have analytic solutions for the superconducting gap evolution. The gap dynamics in single-band conventional superconductors with isotropic gap structures can be solved exactly due to the integrability of the BCS model [97, 98, 27, 28, 82, 26, 23, 99]. The two-band BCS model doubles the number of degrees of freedom compared to the single-band model. Due to the coupling between the two distinct bands, the integrals of motion that were constructed previously for the single-band BCS model [28, 99] do not commute between the two bands, except in the symmetric case $\eta = 1$. In the single-band case, it was determined that there are three different "phases" depending on the strength of the quench Δ_i/Δ_f: in phase A, corresponding to $\Delta_i/\Delta_f < \mathrm{e}^{-\pi/2}$, the gap shows persistent oscillations between two asymptotic values; in phase B, for $\mathrm{e}^{-\pi/2} < \Delta_i/\Delta_f < \mathrm{e}^{\pi/2}$, the gap shows damped $1/t^{1/2}$ oscillations around one asymptotic value; and in phase C, which takes place for $\Delta_i/\Delta_f > \mathrm{e}^{\pi/2}$, the gap asymptotically approaches zero in an exponential fashion.

Whether the two-band BCS model is integrable or not is beyond the scope of this work. Given the difficulties in finding the integrals of motion of the two-band case, in this section we employ instead a perturbative method to extract the long-time asymptotic dynamics of the superconducting gap in phase B, where the gap shows damped oscillations. This is precisely the behavior found numerically for weak quenches, shown in Fig. 4.1. In particular, the method we develop here is a modified version of the one pioneered by Volkov and Kogan in Ref. [25], which allows us to also analytically determine the steady-state gap values $\Delta_{\alpha,\infty}$.

For convenience, we briefly review our notation scheme: subscripts i and f denote the thermal equilibrium value before (i) and after (f) the quench. The subscript ∞ denotes the long-time asymptotic steady-state value of the gap. For example, $\Delta_{\alpha,i}$

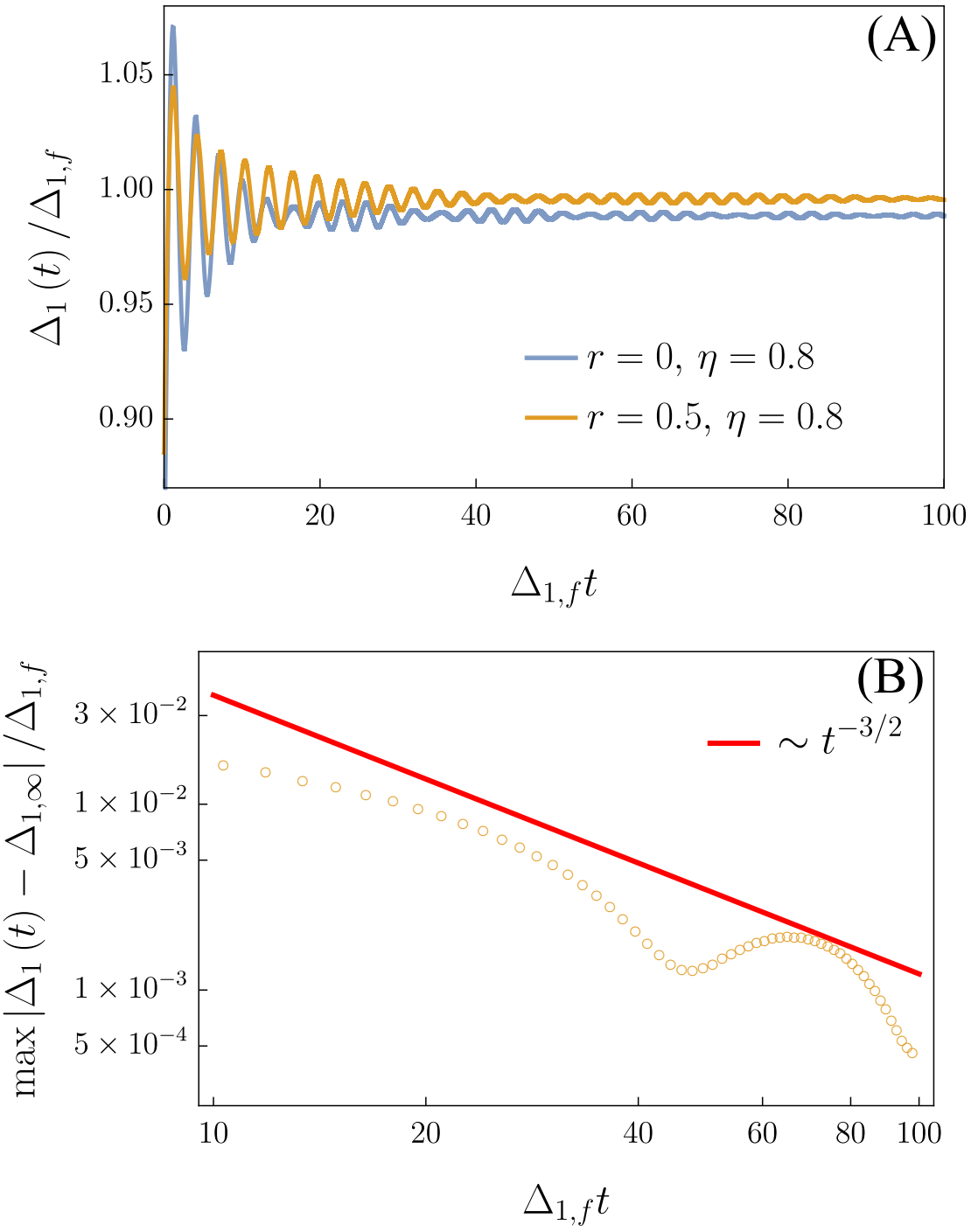

Figure 4.2: (A) Gap oscillations for the case of inter-band pairing only ($r = 0$) and inter-band and intra-band pairing ($r = 0.5$). Here, we set $\eta = 0.8$. (B) The $t^{-3/2}$ damping of the gap oscillations in a log-log scale.

$(\Delta_{\alpha,f})$ is the equilibrium value of gap α before (after) the quench, and $\Delta_{\alpha,\infty}$ is its long-time asymptotic steady-state value following the time evolution governed by the BCS Hamiltonian. We note that our analysis is restricted to weak quenches, resulting in the system being in phase B, where the gap experiences Volkov-Kogan-like behavior.

4.4.1 Linearized equations of motion

To analytically describe the post-quench gap dynamics at long times, we generalize the method used first by Volkov and Kogan in Ref. [25]. Instead of expanding around the final equilibrium state $S^i_{\alpha,f}$ and $\Delta_{\alpha,f}$, however, we expand around the long-time non-equilibrium steady-state values $S^i_{\alpha,\infty}$ and $\Delta_{\alpha,\infty}$. Importantly, these steady-state values will be determined self-consistently in our calculation using Laplace's final value theorem. We thus assume that in the long-time limit the superconducting gaps reach their long-time asymptotic values $\Delta_{\alpha,\infty}$. We expand the equations of motion and the gap equations around the asymptotic steady-state values

$$S^z_\alpha(\varepsilon,t) = S^z_{\alpha,\infty}(\varepsilon) + g_\alpha(\varepsilon,t) \tag{4.11a}$$

$$S^-_\alpha(\varepsilon,t) = S^-_{\alpha,\infty}(\varepsilon) + f_\alpha(\varepsilon,t) \tag{4.11b}$$

$$\Delta_\alpha(t) = \Delta_{\alpha,\infty} + \delta_\alpha(t) \tag{4.11c}$$

where, from the stationary condition of the equations of motion, $S^{\pm}_{\alpha,\infty} = S^x_{\alpha,\infty}$, $S^y_{\alpha,\infty} = 0$, $\varepsilon S^x_{\alpha,\infty} = -\Delta_{\alpha,\infty} S^z_{\alpha,\infty}$. Note that f_α describes pairing amplitude fluctuations and g_α describe density fluctuations. The deviation of the gap from its long-time asymptotic value is denoted by δ_α, which is determined by the pairing-amplitude fluctuations f_α via the gap equations:

$$\delta_\alpha(t) = v_f \sum_\beta \gamma_{\alpha\beta} \int_{-\Lambda}^{\Lambda} d\varepsilon f_\beta(\varepsilon,t) \tag{4.12}$$

where $\gamma_{\alpha\beta}$ is given in Eq. (4.4).

As we will show below, because f''_α is an odd function of ε, δ_α is real, as long as we choose the initial equilibrium gaps of the two bands $\Delta_{\alpha,i}$ to be real. With this in mind, we linearize the equations of motion by inserting Eqs. (4.11) into the Eq. (4.9) to obtain

$$\dot{f}'_\alpha = 2\varepsilon f''_\alpha \tag{4.13a}$$

$$\dot{f}''_\alpha = -2\varepsilon f'_\alpha - 2\Delta_{\alpha,\infty} g_\alpha - 2S^z_{\alpha,\infty}\delta_\alpha(t) \tag{4.13b}$$

$$\dot{g}_\alpha = 2\Delta_{\alpha,\infty} f''_\alpha \tag{4.13c}$$

where $f_\alpha = f'_\alpha + i f''_\alpha$ and the notation $\dot{f} \equiv \frac{df}{dt}$ is used. Note that, as anticipated, f''_α remains an odd function of ε for all times, since $S_{z,\infty}$ and g_α are odd while f'_α is even. As a result, the gap remains real for all times. The fact that the phases of the gaps are constants of motion follows directly from the particle-hole symmetry of the BCS Hamiltonian [23]. Therefore, the relative phase of the two gaps is also a constant of motion and the Leggett (relative phase) mode, which would in any case be overdamped in the regime we study here of inter-band pairing interaction only, is not excited in our quench protocol. In order to excite it, one must break the particle-hole symmetry of the BCS Hamiltonian, for example, by external perturbations as in the pump-probe setups [91].

The linearized equations of motion faithfully describe the long-time dynamics for relatively weak quenches where v_f/v_i is close to 1, since at the long-time limit, the deviations from the asymptotic values are small, i.e. $(g_\alpha, f_\alpha, \delta_\alpha) \ll \left(S^z_{\alpha,\infty}, S^-_{\alpha,\infty}, \Delta_{\alpha,\infty}\right)$. To have a better description of the gap dynamics over a wider time range, we focus on relatively weak quenches where v_f/v_i is close to 1. In this case, the oscillations around $\Delta_{\alpha,\infty}$ are small already at earlier times, allowing for a better comparison between numerics and analytics. Such weak quench regime is also the most relevant to experiments, where excess heating is suppressed.

Since we are interested in δ_α, which is only related to f_α, see Eq. (4.12), we can further simplify the above equations by eliminating g_α to find

$$\ddot{f}''_\alpha = -4E^2_{\alpha,\infty} f''_\alpha - 2S^z_{\alpha,\infty}\dot{\delta}_\alpha(t) \tag{4.14a}$$

$$\dddot{f}'_\alpha = -4E^2_{\alpha,\infty} \dot{f}'_\alpha - 4\varepsilon S^z_{\alpha,\infty}\dot{\delta}_\alpha(t)\ , \tag{4.14b}$$

where $E^2_{\alpha,\infty} = \varepsilon^2 + \Delta^2_{\alpha,\infty}$. Eq. (4.14a) and 4.14b describe the dynamics of the imaginary and real parts of the pairing amplitude fluctuations, respectively, which determine the

time evolution of the imaginary and real parts of the gap.

4.4.2 Solution in Laplace space

To solve the differential equations (4.14a) and (4.14b), it is useful to perform a Laplace transformation $y(s) = \int_0^\infty y(t)\, e^{-st} dt$. We find the the following algebraic equations:

$$f''_\alpha(s) + \frac{2sS^z_{\alpha,\infty}}{s^2 + 4E^2_{\alpha,\infty}}\delta_\alpha(s) = \frac{sf''_{\alpha,0} + \dot{f}''_{\alpha,0}}{s^2 + 4E^2_{\alpha,\infty}} + \frac{2S^z_{\alpha,\infty}}{s^2 + 4E^2_{\alpha,\infty}}\delta_{\alpha,0} \tag{4.15a}$$

$$f'_\alpha(s) - \frac{-4\varepsilon S^z_{\alpha,\infty}}{s^2 + 4E^2_{\alpha,\infty}}\delta_\alpha(s) = \frac{1}{s}\left[f'_{\alpha,0} - \frac{-4\varepsilon S^z_{\alpha,\infty}}{s^2 + 4E^2_{\alpha,\infty}}\delta_{\alpha,0}\right] - \frac{2\varepsilon}{s}\frac{sf''_{\alpha,0} + \dot{f}''_{\alpha,0}}{s^2 + 4E^2_{\alpha,\infty}}. \tag{4.15b}$$

where s is the complex frequency in the Laplace domain and the subscript 0 indicates an initial condition, i.e. $f_{\alpha,0} \equiv f_\alpha(\varepsilon, t = 0^+)$, $\delta_{\alpha,0} \equiv \delta_\alpha(t = 0^+)$, etc. Physically, Eqs. (4.15a) and (4.15b) describe the phase and amplitude dynamics of the gap, respectively.

Since δ_α and f_α are related through the gap equation (4.12), it is convenient to integrate both sides of the above equations over ε. Then, Eq. (4.15a) is trivially satisfied, since $S^z_{\alpha,\infty}$ is an odd function of ε, by virtue of Eq. (4.8), $f''_{\alpha,0} = 0$ by construction, and $\dot{f}''_{\alpha,0}$ is an odd function of ε, by virtue of the second equation of (4.13). Consequently, we are left with a single equation for f'_α and δ_α, which are related through the gap equation (4.12).

Expressing f in terms of δ, and recasting Eq. (4.15b) in matrix form, the deviations of the superconducting gaps from their asymptotic values, δ_α, are given by:

$$\left(\hat{\Phi}^\infty(s) + \hat{\mathcal{M}}\right)\vec{\delta}(s) = \frac{\vec{I}(s)}{s}, \tag{4.16}$$

where the hat (arrow) denote a matrix (vector) in band space. Here, we defined:

$$\hat{\Phi}^\infty_{\alpha\beta}(s) = \mathbb{I}_{\alpha\beta}\left(s^2 + 4\Delta^2_{\alpha,\infty}\right)\left\langle \frac{S^x_{\alpha,\infty}/\Delta_{\alpha,\infty}}{s^2 + 4E^2_{\alpha,\infty}}\right\rangle \tag{4.17}$$

$$\hat{\mathcal{M}}_{\alpha\beta} = \left(\hat{\gamma}^{-1}\right)_{\alpha\beta} - \mathbb{I}_{\alpha\beta}\left\langle \frac{S^x_{\beta,\infty}}{\Delta_{\beta,\infty}}\right\rangle. \tag{4.18}$$

where $\mathbb{I}$ is the identity matrix in band space and the following notation is used:

$$\langle \ldots \rangle = v_f \int d\varepsilon \, (\ldots) \; . \tag{4.19}$$

For convenience, we write $\hat{\Phi}^{\infty}_{\alpha\beta}(s) \equiv \mathbb{I}_{\alpha\beta}\Phi^{\infty}_{\alpha}$ and define:

$$\Phi^{\infty}_{\alpha}(s) = \left(s^2 + 4\Delta^2_{\alpha,\infty}\right) \left\langle \frac{S^x_{\alpha,\infty}/\Delta_{\alpha,\infty}}{s^2 + 4E^2_{\alpha,\infty}} \right\rangle \tag{4.20}$$

The function $\vec{I}(s)$ on the right-hand side is given by (detailed derivation in Appendix B.1)

$$\begin{aligned} I_{\alpha}(s) = &\sum_{\beta} \left(\hat{\gamma}^{-1}\right)_{\alpha\beta} \delta_{\beta,0} + \left(\Delta_{\alpha,i} - \Delta_{\alpha,\infty}\right) \\ &\times \left[\Phi^{i}_{\alpha}(s) - \frac{v_f}{v_i} \sum_{\beta} \left(\hat{\gamma}^{-1}\right)_{\alpha\beta} \frac{\Delta_{\beta,i}}{\Delta_{\alpha,i}} \right] , \end{aligned} \tag{4.21}$$

with:

$$\Phi^{i}_{\alpha}(s) = \left(s^2 + 4\Delta^2_{\alpha,\infty}\right) \left\langle \frac{S^x_{\alpha,i}/\Delta_{\alpha,i}}{s^2 + 4E^2_{\alpha,\infty}} \right\rangle \tag{4.22}$$

The solution for $\vec{\delta}(s)$ in Laplace space is then simply given by

$$\vec{\delta}(s) = \left(\hat{\Phi}^{\infty}(s) + \hat{\mathcal{M}}\right)^{-1} \frac{\vec{I}(s)}{s} \tag{4.23}$$

It is clear that without inter-band interaction, $V = 0$, $\hat{\mathcal{M}}_{\alpha\beta}$ becomes a diagonal matrix, since $\hat{\gamma}_{\alpha\beta}$ in Eq. (4.4) is diagonal. As a result, Eq. (4.16) becomes diagonal in band space as well, and the two-band model reduces to two independent one-band models. In the following subsections, we will extract the dynamics of the gaps in the long-time limit from their analytic behaviors in Laplace space. These are determined by the functions $\hat{\Phi}^{\infty}(s)$ and $\vec{I}(s)$, as they are the only s-dependent functions in Eq. (4.16). Their s-dependence comes from the two functions $\Phi^{\infty}_{\alpha}(s)$ and $\Phi^{i}_{\alpha}(s)$ defined above.

The function $\Phi^{i}_{\alpha}(s)$ is straightforward to calculate since the initial pseudospin configuration is given by the equilibrium value of the gap at $T = 0$, i.e. $S^x_{\alpha,i}/\Delta_{\alpha,i} = \frac{1}{2\sqrt{\varepsilon^2 + \Delta^2_{\alpha,i}}}$.

Inserting this initial pseudo-spin state into Eq. (4.22), this can be brought to the form

$$\Phi_{\alpha}^{i}(s) = \Upsilon\left(\tilde{\Delta}_{\alpha,i}, \frac{s}{2\Delta_{\alpha,\infty}}\right) \tag{4.24}$$

where we defined the dimensionless ratio $\tilde{\Delta}_{\alpha,i} = \Delta_{\alpha,i}/\Delta_{\alpha,\infty}$ and the function

$$\Upsilon(\Delta, x) = v_f \frac{\sqrt{\frac{x^2+1}{\Delta^2}}\arccos\left(\sqrt{\frac{x^2+1}{\Delta^2}}\right)}{\sqrt{1-\frac{1+x^2}{\Delta^2}}} \tag{4.25}$$

To find an explicit expression for $\Phi_{\alpha}^{\infty}(s)$, given by Eq. (4.20), we first need to compute the function $S_{\alpha,\infty}^{x}/\Delta_{\alpha,\infty}$. The gap equation (see Eq. (4.7)), which is satisfied regardless of whether the system is in thermal equilibrium or not, restricts the expectation value of this quantity to:

$$\left\langle \frac{S_{\alpha,\infty}^{x}}{\Delta_{\alpha,\infty}} \right\rangle = \sum_{\beta} \left(\hat{\gamma}^{-1}\right)_{\alpha\beta} \frac{\Delta_{\beta,\infty}}{\Delta_{\alpha,\infty}} \tag{4.26}$$

As we discussed above, the non-zero inter-band interactions render the matrix $\hat{\mathcal{M}}$ off-diagonal and make the two-band model fundamentally different than the single-band case. While a generic discussion of arbitrary inter- and intra-band interactions is possible, the analysis is simplified considerably by focusing on the case of inter-band repulsion only, i.e. $r = 0$. Indeed, our numerical results discussed in Fig. 4.2 show that the general behavior of the two-band problem is the same for $r = 0$ and $r \neq 0$. Setting $r = 0$ in Eq. (4.4) yields an off-diagonal matrix $\hat{\gamma} = \begin{pmatrix} 0 & -\eta \\ -1 & 0 \end{pmatrix}$. As result, the equation above becomes:

$$\left\langle \frac{S_{1,\infty}^{x}}{\Delta_{2,\infty}} \right\rangle = \eta \left\langle \frac{S_{2,\infty}^{x}}{\Delta_{1,\infty}} \right\rangle = -1\,. \tag{4.27}$$

Note that this ratio involves the pseudospin of band α and the gap of the other band $\bar{\alpha}$, where $\bar{\alpha} = 1(2)$ for $\alpha = 2(1)$. To proceed, we note that, in equilibrium, the same relationship holds between the ratios of the pseudospin and the gap:

$$\left\langle \frac{S^x_{1,f}}{\Delta_{2,f}} \right\rangle = \eta \left\langle \frac{S^x_{2,f}}{\Delta_{1,f}} \right\rangle = -1\,. \tag{4.28}$$

The difference is that, in equilibrium, from Eq. (4.8), we know precisely the expression for $S^x_{\alpha,f}$:

$$\left\langle \frac{S^x_{1,f}}{\Delta_{2,f}} \right\rangle = \left\langle \frac{\Delta_{1,f}/\Delta_{2,f}}{2\sqrt{\varepsilon^2 + \Delta^2_{1,f}}} \right\rangle = -1 \tag{4.29a}$$

$$\eta \left\langle \frac{S^x_{2,f}}{\Delta_{1,f}} \right\rangle = \eta \left\langle \frac{\Delta_{2,f}/\Delta_{1,f}}{2\sqrt{\varepsilon^2 + \Delta^2_{2,f}}} \right\rangle = -1\,, \tag{4.29b}$$

Based on this similarity, we propose the following ansatz:

$$\frac{S^x_{\alpha,\infty}}{\Delta_{\alpha,\infty}} = \frac{\tilde{\Delta}_{\alpha,f}}{\tilde{\Delta}_{\bar{\alpha},f}} \left(\frac{1}{2\sqrt{\varepsilon^2 + \Delta^2_{\alpha,f}}} \right) \tag{4.30}$$

where $\tilde{\Delta}_{\alpha,f} = \Delta_{\alpha,f}/\Delta_{\alpha,\infty}$ is defined analogously to $\tilde{\Delta}_{\alpha,i}$. Clearly, this ansatz satisfies the constraint Eq. (4.27). For $r \neq 0$, the constraint has a more complicated form. The corresponding ansatz is expected to be less concise as Eq. (4.30). For the purpose of clarity, we will stay with the case where $r = 0$. We will verify the validity of this ansatz later by an explicit comparison to numerical calculations and by comparison with the exact solution of the single-band case. For now, we proceed with this ansatz and perform the energy integration in the expression of $\Phi^\infty_\alpha(s)$. We obtain:

$$\Phi^\infty_\alpha(s) = \frac{\tilde{\Delta}_{\alpha,f}}{\tilde{\Delta}_{\bar{\alpha},f}} \Upsilon\left(\tilde{\Delta}_{\alpha,f}, \frac{s}{2\Delta_{\alpha,\infty}} \right) \tag{4.31}$$

4.5 Self-consistency conditions and long-time asymptotic value of the gap

The perturbative approach we purposed in Chapter 3 has been validated by comparing with the exact solution of quench dynamics of the single-band BCS model. We now perform the same calculation for the two-band model with pure inter-band repulsion

$(r=0)$. Using Eqs.4.24 and 4.31, we obtain the following expression for $\delta_\alpha(s)$ from Eq. (4.16):

$$s\delta_\alpha(s) = \left(\Phi^\infty_{\bar{\alpha}}(s) + \frac{1}{\eta_{\bar{\alpha}}}\frac{\Delta_{\alpha,\infty}}{\Delta_{\bar{\alpha},\infty}}\right)\frac{I_\alpha(s)}{D(s)} + \frac{1}{\eta_\alpha}\frac{I_{\bar{\alpha}}(s)}{D(s)}, \tag{4.32}$$

where, for convenience of notation, we introduced $\eta_1 = 1$ and $\eta_2 \equiv \eta$, $I_\alpha(s)$ is given by Eq. (4.21), and:

$$D(s) = \Phi^\infty_1(s)\Phi^\infty_2(s) + \frac{\Delta_{2,\infty}}{\Delta_{1,\infty}}\Phi^\infty_2(s) + \frac{1}{\eta}\frac{\Delta_{1,\infty}}{\Delta_{2,\infty}}\Phi^\infty_1(s)\ . \tag{4.33}$$

To find the asymptotic long-time value of the gaps $\Delta_{\alpha,\infty}$, we employ once again the final value theorem in Laplace space, Eq. 3.71. We numerically solve for $\Delta_{1,\infty}$ and $\Delta_{2,\infty}$ for a given quench protocol, $v_i \to v_f$, or equivalently $\Delta_{1,i} \to \Delta_{1,f}$. As shown in Fig. 4.3, we find that, in the case of pure inter-band interactions $(r=0)$, the ratios between the asymptotic and final equilibrium gaps $\Delta_{\alpha,\infty}/\Delta_{\alpha,f}$ are, to a very good approximation (i.e. with a numerical deviation of less than 0.01%), equal for both bands, i.e. $\tilde{\Delta}_{1,f} = \tilde{\Delta}_{2,f}$.

Using the result obtained here that $\tilde{\Delta}_{1,f} = \tilde{\Delta}_{2,f}$, the pre-factor of Eq. (4.31) becomes 1. Thus, both $\Phi^\infty_\alpha(s)$ and $\Phi^i_\alpha(s)$ have the same functional dependence: $\Phi^\infty_\alpha(s) = \Upsilon\left(\tilde{\Delta}_{\alpha,f}, \frac{s}{2\Delta_{\alpha,\infty}}\right)$, $\Phi^i_\alpha(s) = \Upsilon\left(\tilde{\Delta}_{\alpha,i}, \frac{s}{2\Delta_{\alpha,\infty}}\right)$.

4.6 Damped gap oscillations in the long time limit

The long-time behavior of the gap in the time domain $\Delta(t)$ can be obtained by applying the inverse Laplace transformation to Eq. (4.32). In order to perform the inverse Laplace transformation, we first need to study the analytical behavior of the solution in Laplace space and find its poles and branch cuts. They are determined by the analytic properties of the function $\Upsilon(\Delta, x)$, defined in Eq. (4.25) and repeated here for convenience:

$$\Upsilon(\Delta, x) = v_f \frac{\sqrt{\frac{x^2+1}{\Delta^2}}\arccos\left(\sqrt{\frac{x^2+1}{\Delta^2}}\right)}{\sqrt{1-\frac{1+x^2}{\Delta^2}}} \tag{4.34}$$

The reason why only the analytical properties of $\Upsilon(\Delta, x)$ matter is because we can

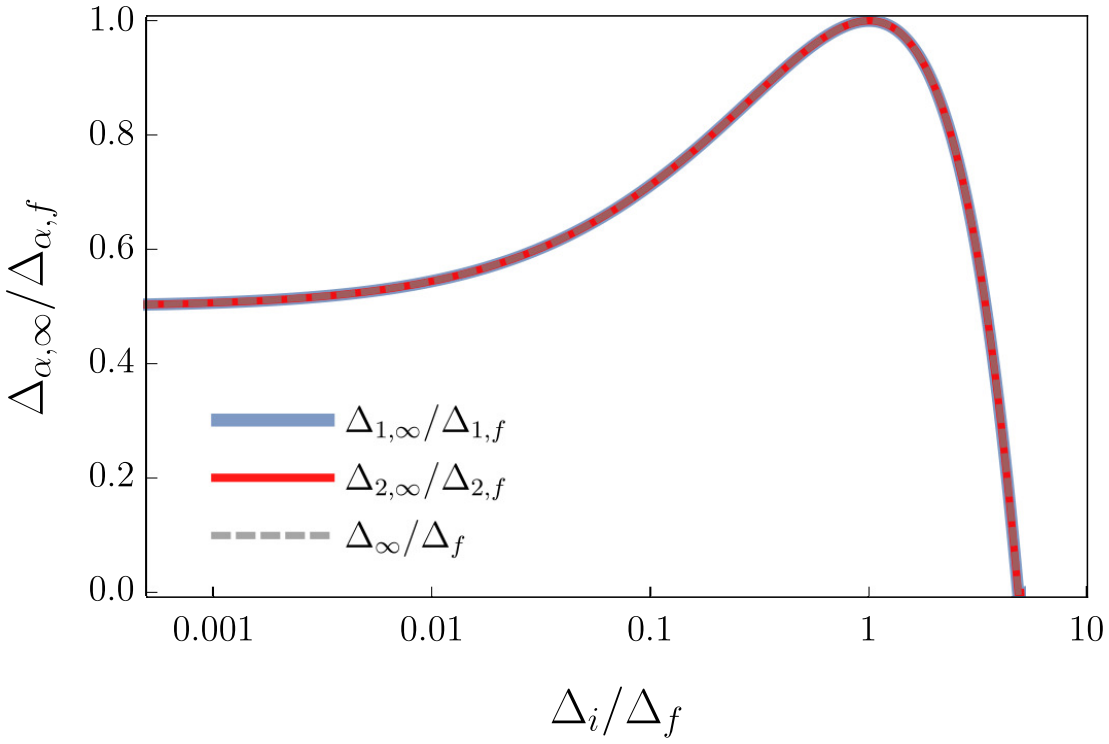

Figure 4.3: Asymptotic values of the gaps in the two band case as a function of the interaction quench parameter Δ_i/Δ_f. The dashed gray line is the result for the single-band BCS model. For the two-band model, we use $\Delta_{1,i}/\Delta_{1,f}$ as the quench parameter, and we choose the ratio between the density of states to be $\eta = 0.8$.

express both $\Phi_\alpha^i(s)$ and $\Phi_\alpha^\infty(s)$ in terms of this function:

$$\Phi_1^{i/\infty}(s) = \Upsilon\left(\tilde{\Delta}_{1,i/f}, z\right) \tag{4.35a}$$

$$\Phi_2^{i/\infty}(s) = \Upsilon\left(\tilde{\Delta}_{2,i/f}, \kappa z\right), \tag{4.35b}$$

where $z = \frac{s}{2\Delta_{1,\infty}}$, $\tilde{\Delta}_{\alpha,i/f,\infty} = \frac{\Delta_{\alpha,i/f}}{\Delta_{\alpha,\infty}}$, and $\kappa = \frac{\Delta_{1,\infty}}{\Delta_{2,\infty}}$. By choosing the gap with $\alpha = 1$ to be the one that is asymptotically smaller, it holds that $|\kappa| < 1$.

The function $\Upsilon(\Delta, z)$ has two branch cuts, one between $(-i\infty, -i)$ and another one between $(i, i\infty)$. The function is analytic elsewhere. Applying the Cauchy's residue theorem (see Appendix B.3 and Fig. B.1 for details), we convert the Bromwich integral into four integrals along the sides of the two branch cuts. Note that we have already

eliminated the pole at the origin by imposing the final value theorem (Eq. (3.71)). In addition, we also use the following properties of the function Υ:

$$\Upsilon\left(\Delta,\, z\right) = \Upsilon\left(\Delta,\, -z\right) \tag{4.36a}$$

$$\mathrm{Re}\left[\Upsilon\left(\Delta,\, 0^{+} \pm iy\right)\right] = \mathrm{Re}\left[\Upsilon\left(\Delta,\, 0^{-} \pm iy\right)\right], \text{ for } y > 1 \tag{4.36b}$$

$$\mathrm{Im}\left[\Upsilon\left(\Delta,\, 0^{+} \pm iy\right)\right] = -\mathrm{Im}\left[\Upsilon\left(\Delta,\, 0^{-} \pm iy\right)\right], \text{ for } y > 1. \tag{4.36c}$$

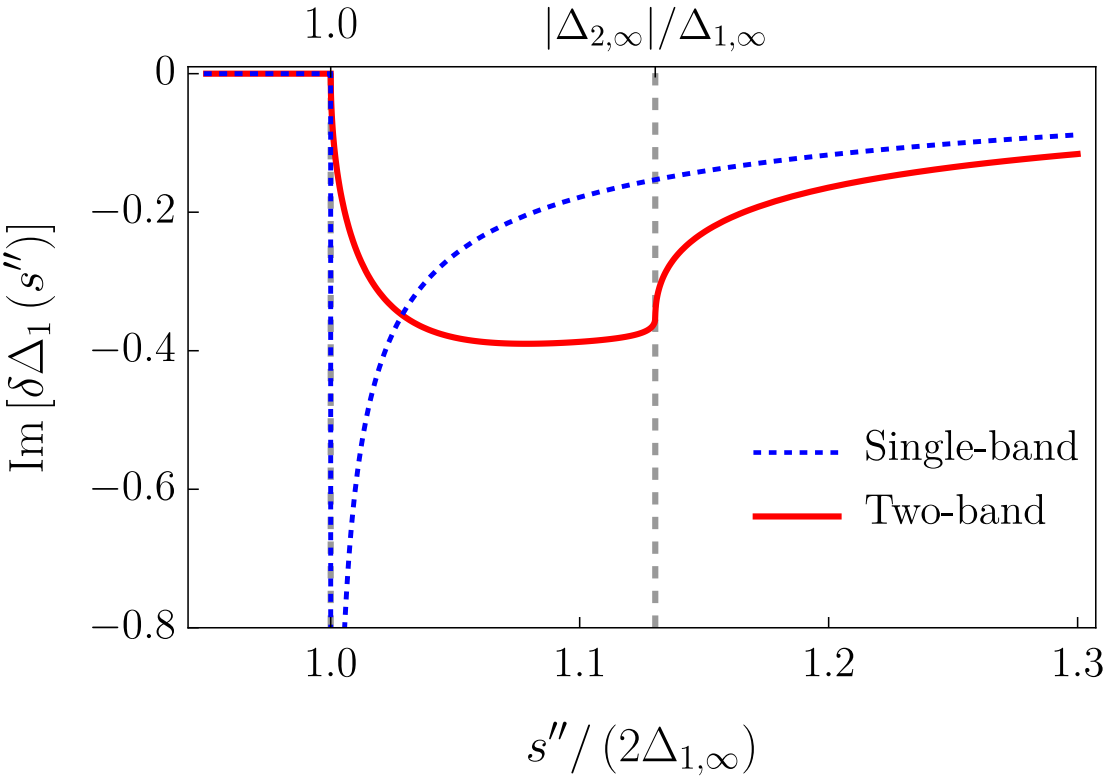

Figure 4.4: Non-analyticity of the gaps in Laplace space along the imaginary axis, s''. In the single-band case (blue dashed line), the only non-analyticity is the inverse square root branch point at $s'' = \pm 2\Delta_{\infty}$ (only the positive axis is shown here). In two-band systems (red solid line), however, the branch point at $s'' = \pm 2\Delta_{1,\infty}$ becomes square root like. Moreover, additional square root branch points appear at $s'' = \pm 2\Delta_{2,\infty}$, which gives rise to the additional oscillation frequency of the gaps.

As a result, the inverse Laplace transformation is given by the following integral:

$$\delta_\alpha(t) = \frac{2}{\pi}\int_i^{i\infty} \mathrm{Im}\left[z\delta_\alpha(z)\right]\frac{\cosh\left(2\Delta_{\alpha,\infty}zt\right)}{z}dz \tag{4.37}$$

where $z\delta_\alpha(z)$ is given by

$$\begin{aligned}
\frac{z\delta_\alpha(z)}{2\Delta_{\alpha,\infty}} = & -\frac{1}{\eta_2}\left[\frac{1}{2}\frac{v_f}{v_i}\left(\frac{\tilde{\Delta}_{\alpha,\infty}}{\tilde{\Delta}_{\bar{\alpha},\infty}}+\frac{\tilde{\Delta}_{\bar{\alpha},\infty}}{\tilde{\Delta}_{\alpha,\infty}}\right)-1\right]\frac{1}{\tilde{D}(z)} \\
& +\frac{\left(\tilde{\Delta}_{\alpha,\infty}-1\right)}{2}\frac{\Upsilon\left(\tilde{\Delta}_{\alpha,\infty},\frac{\Delta_{1,\infty}}{\Delta_{\alpha,\infty}}z\right)\Upsilon\left(\tilde{\Delta}_{\bar{\alpha},f},\frac{\Delta_{1,\infty}}{\Delta_{\bar{\alpha},\infty}}z\right)}{\tilde{D}(z)} \\
& -\frac{1}{2\eta_\alpha}\left(\frac{\Delta_{\bar{\alpha},\infty}}{\Delta_{\alpha,\infty}}\right)\left(\frac{v_f}{v_i}\frac{\tilde{\Delta}_{\bar{\alpha},\infty}}{\tilde{\Delta}_{\alpha,\infty}}-1\right)\frac{\Upsilon\left(\tilde{\Delta}_{\bar{\alpha},f},\frac{\Delta_{1,\infty}}{\Delta_{\bar{\alpha},\infty}}z\right)}{\tilde{D}(z)} \\
& +\frac{\left(\tilde{\Delta}_{\bar{\alpha},i}-1\right)}{2\eta_\alpha}\left(\frac{\Delta_{\bar{\alpha},\infty}}{\Delta_{\alpha,\infty}}\right)\frac{\Upsilon\left(\tilde{\Delta}_{\bar{\alpha},i},\frac{\Delta_{1,\infty}}{\Delta_{\bar{\alpha},\infty}}z\right)}{\tilde{D}(z)} \\
& +\frac{\left(\tilde{\Delta}_{\alpha,\infty}-1\right)}{2\eta_{\bar{\alpha}}}\left(\frac{\Delta_{\alpha,\infty}}{\Delta_{\bar{\alpha},\infty}}\right)\frac{\Upsilon\left(\tilde{\Delta}_{\alpha,\infty},\frac{\Delta_{1,\infty}}{\Delta_{\alpha,\infty}}z\right)}{\tilde{D}(z)}
\end{aligned} \tag{4.38}$$

where

$$\begin{aligned}
D(z) = & \Upsilon(\tilde{\Delta}_{1,f},z)\Upsilon(\tilde{\Delta}_{2,f},\kappa z) \\
& +\frac{1}{\kappa}\Upsilon(\tilde{\Delta}_{2,f},\kappa z)+\frac{\kappa}{\eta_2}\Upsilon(\tilde{\Delta}_{1,f},z)\,.
\end{aligned} \tag{4.39}$$

In the long-time limit, where $2\Delta_{1,\infty}t \gg 1$, the integrand of Eq. (4.37) is highly oscillatory. Only singular behaviors of $\mathrm{Im}\left[z\delta_\alpha(z)\right]$ will therefore make a contribution to the long-time dynamics of the superconducting gap. Indeed, $\mathrm{Im}\left[z\delta_\alpha(z)\right]$ has two branch points along $z\in[i,\,\infty)$: one is located at $z=i$ and the other one is located at $z=i/|\kappa|$. We expand $\mathrm{Im}\left[z\delta_\alpha(z)\right]$ near these two branch points, i.e. $z=i+i\epsilon$ and $z=i/|\kappa|\pm i\epsilon$, and find that both exhibit $\sqrt{\epsilon}$ behavior (details are shown in Appendix B.2). This is sharply distinct from the single-band case, where only one branch point is present along $z\in[i,\,\infty)$. More importantly, the asymptotic behavior in the vicinity of the branch point in the single-band case is $1/\sqrt{\epsilon}$ rather than $\sqrt{\epsilon}$. The two cases are plotted and

compared in Fig. 4.4. The $1/\sqrt{\epsilon}$ behavior leads to a $t^{-1/2}$ decay of the gap oscillation amplitude at long times in the single-band case [25]. In contrast, the $\sqrt{\epsilon}$ behavior in Laplace space leads to a faster $t^{-3/2}$ decay in the two-band model

$$\int_1^\infty \frac{\sqrt{y-1}}{y} \cos\left[y\left(2\Delta t\right)\right] dy \simeq -\frac{\sqrt{\pi}\sin\left(2\Delta t+\frac{\pi}{4}\right)}{2\left(2\Delta t\right)^{3/2}} \tag{4.40}$$

for $2\Delta t \gg 1$ (details are shown in Appendix B.3). The damping of the gap oscillations thus occurs faster for two-band superconductivity.

To find the full long-time expressions of the gap, including prefactors and oscillatory factors, we perform a careful asymptotic analysis of $\mathrm{Im}\left[z\delta_\alpha\left(z\right)\right]$. The final result for the long-time gap oscillations reads

$$\Delta_1\left(t\right) \simeq \Delta_{1,\infty} + \mathcal{A}_1\frac{\sin\left(2\Delta_{1,\infty}t+\frac{\pi}{4}\right)}{\left(\Delta_{1,\infty}t\right)^{3/2}} + \mathcal{B}_1\frac{\sin\left(2\left|\Delta_{2,\infty}\right|t-\frac{\pi}{4}\right)}{\left(\left|\Delta_{2,\infty}\right|t\right)^{3/2}} + \mathcal{C}_1\frac{\sin\left(2\left|\Delta_{2,\infty}\right|t+\frac{\pi}{4}\right)}{\left(\left|\Delta_{2,\infty}\right|t\right)^{3/2}} \tag{4.41a}$$

$$\Delta_2\left(t\right) \simeq \Delta_{2,\infty} + \mathcal{A}_2\frac{\sin\left(2\left|\Delta_{2,\infty}\right|t+\frac{\pi}{4}\right)}{\left(\left|\Delta_{2,\infty}\right|t\right)^{3/2}} + \mathcal{B}_2\frac{\sin\left(2\Delta_{1,\infty}t-\frac{\pi}{4}\right)}{\left(\Delta_{1,\infty}t\right)^{3/2}} + \mathcal{C}_2\frac{\sin\left(2\Delta_{1,\infty}t+\frac{\pi}{4}\right)}{\left(\Delta_{1,\infty}t\right)^{3/2}} \tag{4.41b}$$

where the pre-factors $\mathcal{A}_\alpha$, $\mathcal{B}_\alpha$ and $\mathcal{C}_\alpha$ are calculated from the asymptotic analysis and explicitly shown in Appendix B.4. The gap oscillation frequencies are determined by the asymptotic values of the gaps in the two different bands $\Delta_{\alpha,\infty}$. As discussed in the previous sections, the asymptotic values of the gaps are determined by the quench amplitude $\Delta_{\alpha,i}/\Delta_{\alpha,f}$ and the ratio of the density of states η between the two bands. In general, they will also depend on $r = -U/V$, which we have set to zero for simplicity here. The same holds for the pre-factors of the sinusoidal oscillations.

In Fig. 4.5, we compare our analytical results to the numerical solution of the equations of motion for two different (weak) quench amplitudes in phase B. We find an excellent quantitative agreement between the two, which also justifies our analytical ansatz *a posteriori*.

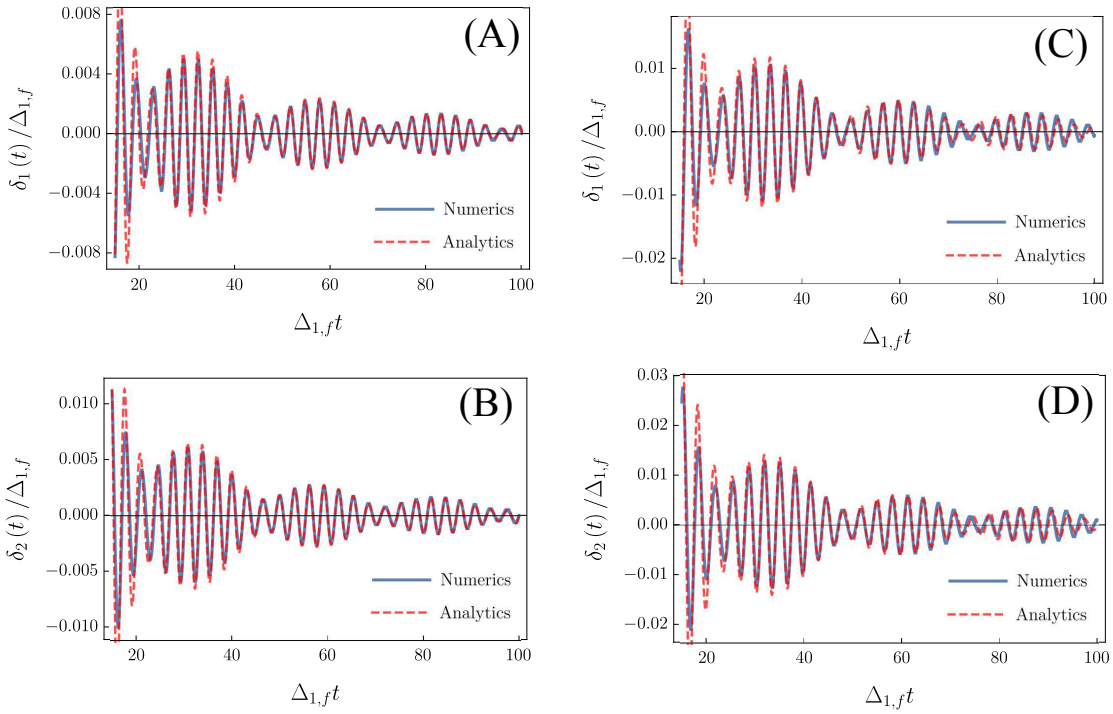

Figure 4.5: Comparison between numerical solution of the gap dynamics and the analytical approximation in Eqs. (4.41a) and (4.41b). (A) and (B) correspond to a interaction quench from $v_i = 0.19$ to $v_f = 0.2$. (C) and (D) correspond to interaction quench from $v_i = 0.18$ to $v_f = 0.2$. The ratio of density of states between the two bands is set to be $\eta = 0.8$ for all the panels.

4.7 Conclusions

In this chapter, we develop a generalization of the Volkov-Kogan Laplace space analysis of post-quench dynamics in s-wave BCS superconductors in the collisionless regime [25], and apply it to quenches of the inter-band interaction in two-band BCS models. We show that the two-band model is fundamentally different from the single-band model if inter-band interactions are present and the density of states at the Fermi energy in the two bands is different. This manifests as a different, faster power-law decay of the post-quench oscillations, which vanish as $t^{-3/2}$ as opposed to the $t^{-1/2}$ law found in the single-band case. For weak quenches, our analytical results for perfectly match numerical results in the long-time limit. This shows that the dynamics in multi-band systems cannot be simply decomposed into a sum of multiple single-band dynamical terms. From a physical viewpoint, the Cooper pairs in two-band models do not only dephase between different energy states, but also between the two bands via the inter-band interaction. This leads to a faster relaxation of the gap oscillations in the collisionless regime. The dephasing between different bands is intrinsic to multi-band systems and therefore independent on the quench amplitude. Finally, we show how our analytical result merges into the single-band case in case of symmetric density of states of the two bands.

From a methodological viewpoint, our analysis is distinct from the one by Volkov and Kogan [25] (see also the more recent works by Yuzbashyan and co-workers [100, 99]) as we linearize around the asymptotic long-time pseudo-spin state as opposed to the final equilibrium states. This allows us to self-consistently determine the asymptotic long-time steady-state values of the gaps $\Delta_{\alpha,\infty}$ over the full range of quench amplitudes in phase B (and phase C, where they vanish). We explicitly show that the self-consistent equation for the steady-state gap in the single-band case agrees with the exact expression derived within the integrability Lax vector analysis [82, 23, 26]. Like in the two-band model we investigate, our method can be very useful in cases where an exact solution is not (yet) available.

Chapter 5

Impact of damping on the superconducting gap dynamics induced by intense terahertz pulses

This chapter reproduces content published in Physical Review B in the article "Impact of damping on the superconducting gap dynamics induced by intense terahertz pulses", Tianbai Cui, Xu Yang, Chirag Vaswani, Jigang Wang, Rafael M. Fernandes, and Peter P. Orth, Phys. Rev. B **100**, 054504 (2019), ©2019 American Physical Society.

5.1 Introduction

The coherent control of non-equilibrium states of interacting quantum matter promises far-reaching capabilities by turning on (or off) desired electronic material properties. A particular focus in this field has been the manipulation of superconductivity by non-equilibrium probes. While earlier works showed that microwave pulses could be used to enhance the superconducting transition temperature T_c of thin superconducting films [77, 101, 78], recent advances in ultrafast pump-and-probe techniques opened the possibility of investigating superconductivity in the pico- and femto-second timescales

by coherent light pulses [20, 102, 103, 93, 104, 94, 105, 106, 107, 108]. Such coherent pulses have been employed to manipulate the electronic and lattice properties of quantum materials, resulting in transient behaviors that are consistent with the onset of non-equilibrium superconductivity above T_c [109, 110, 111]. Alternatively, coherent pulses have also been employed to assess the coherent dynamics of the superconducting state [92, 93, 94, 79, 112, 96, 81, 113, 114, 115, 91, 116].

In Ref. [93], a single-cycle intense THz pulse resonant with the superconducting gap Δ was applied to a thin film of the conventional s-wave superconductor NbN, reporting coherent gap oscillations with frequency 2Δ. This was followed by a slow decrease of the gap, possibly associated with thermalization of the energy absorbed from components of the pump with frequencies larger than 2Δ. To maintain coherence and avoid excess heating, it is thus advantageous to apply longer, multi-cycle pulses with exclusively sub-gap frequency components [104, 94], where Cooper pairs cannot be broken into quasi-particle Bogoliubov excitations via single photon absorption processes. In the absence of pair-breaking and on sufficiently short timescales before thermalization effects with the environment set in, the electronic state is then expected to evolve in the manifold of Bardeen-Cooper-Schrieffer (BCS) states. This coherent time evolution can be conveniently recast in terms of Anderson pseudospins [75] precessing around a pseudo-magnetic field that is modified by the optical pulse.

Here, we report such an experimental study of superconducting gap dynamics in thin films of NbN and Nb_3Sn using intense, multi-cycle sub-gap THz pulses in a hitherto unexplored regime of large THz field amplitudes of up to 109 kV/cm. This allows for substantial light-control of the gap, even for initial temperatures far below the superconducting transition temperature T_c, where initial thermal quasi-particle excitations are absent. We focus our study on the regime of coherent gap dynamics, which occurs on timescales less than 20 picoseconds. This is complementary to an interesting earlier study by Beck *et al.* in Ref. [104] using ultra-narrow sub-gap terahertz pulses with GHz linewidths that focused on longer timescales of hundreds of picoseconds. That study reported an enhancement of the gap at intermediate temperatures due to a redistribution of thermally excited quasi-particles.

We complement our experimental work with detailed theoretical modeling that can

phenomenologically capture all the salient features observed experimentally. This includes damping and decoherence effects that arise from residual, integrability-breaking interactions within the electronic system, which are not captured within the BCS approximation. In particular, our results shed light on the two different relaxation timescales that are inherent to the observed dynamics. We show that these are markedly shorter than lattice relaxation rates, but consistent with rapid relaxation that occurs within the electronic subsystem.

Specifically, we study superconducting gap dynamics in thin films of NbN and Nb_3Sn subjected to intense THz fields with sub-gap spectra. Our data reveals that while the pump is on, the gap oscillates at a frequency equal to twice the pump frequency. This previously observed behavior is well-described by the solution to the time-dependent BCS equation, which naturally gives rise to gap oscillations [25, 117, 118, 23, 27, 119, 118, 120, 82, 79, 112, 96, 81, 121, 122, 123, 124, 125]. When the pump is turned off, however, the gap oscillations quickly disappear in the experiment, yet the gap amplitude continues to be suppressed, while remaining finite. These behaviors, particularly the latter one, are at odds with the non-equilibrium BCS dynamics, which predicts the gap to display coherent oscillation with slow collisionless relaxation around a constant average value [25, 27, 23, 79, 126]. We want to emphasize that our experimental observations are consistent with previous studies [93] employing single-cycle pulses, but they are more pronounced at the large pump fluences that we employ.

To elucidate this behavior, we develop a semi-phenomenological model that captures not only the coherent evolution of the gap function in the picosecond time scale, but also damping and decoherence effects in the time scale of tens of picoseconds. Because this time scale precedes the thermalization with the lattice degrees of freedom, the relevant relaxation processes must arise solely within the electronic subsystem from effects not captured by BCS. These include interactions between Bogoliubov quasi-particles and the coupling between the Higgs (amplitude) mode and the continuum. In the pseudospin notation, we identify two types of relaxation process: the longitudinal relaxation T_1, corresponding to relaxation of quasi-particles, and the transverse relaxation T_2, corresponding to relaxation of the gap. While the main effect of T_2 is to suppress the gap oscillations after the pump is turned off, the main impact of T_1 in this regime is to decrease the average gap value. We show that the previously observed gap dynamics in

NbN for single-cycle pulses, reported in Ref. [93], can also be quantitatively described within our semi-phenomenological model. To get similar quantitative agreement for multi-cycle pulse experiments in both NbN and Nb_3Sn, we need to introduce an additional phenomenological parameter η that describes the dissipation of heat out of the electronic subsystem into the environment. We find that for off-resonant multi-cycle pump pulses, where the amount of energy that is deposited by the pump is large, about 30% of the energy is rapidly dissipated to the environment.

The paper is organized as follows: we first summarize the experimental results in Sec. 5.2. Then, we introduce our theoretical modeling and present a thorough analysis it in Sec. 5.3. In Sec. 5.4, we perform a detailed theory-experiment comparison, before drawing our conclusions in Sec. 5.5. Details about the experimental setup and pseudospin formalism are provided in Appendices C.1 and C.2, respectively.

The experimental results shown in this chapter were carried out by the group of Prof. Jigang Wang in the Ames Laboratory and Iowa State University.

5.2 Experimental results

We probe the superconducting gap dynamics in NbN and Nb_3Sn using intense THz pump, weak THz probe ultrafast spectroscopy. Our NbN sample is a 120 nm thick NbN film grown on (100)-oriented MgO single crystalline substrates via pulsed laser deposition, as previously reported in Ref. [127]. An interesting study of the non-linear optical response in NbN can also be found in Ref. [128]. The Nb_3Sn sample is a thinner film that is only 20 nm thick and was grown by magnetron sputtering on a 1 mm Al_2O_3 (100) substrate [105]. The superconducting transition temperatures in equilibrium are $T_c(\mathrm{NbN}) \approx 13$ K and $T_c(Nb_3Sn) \approx 16$ K, respectively. We extract the optical conductivity in equilibrium and non-equilibrium from the complex transmission using a scanning gate pulse delay t_{gate}. By varying the optical delay t_{pp} between the pump and the probe pulses, we track the ultrafast dynamics of the superconducting gap $\Delta(t)$ on picosecond timescales. Additional experimental details are given in Appendix C.1.

Let us first discuss the experimental results for NbN. The behavior of the real and imaginary parts of the optical conductivity, $\sigma_1(\omega)$ and $\sigma_2(\omega)$, of NbN is shown in Fig. 5.1 (A)-(B). In equilibrium (gray curves), the onset of superconductivity below

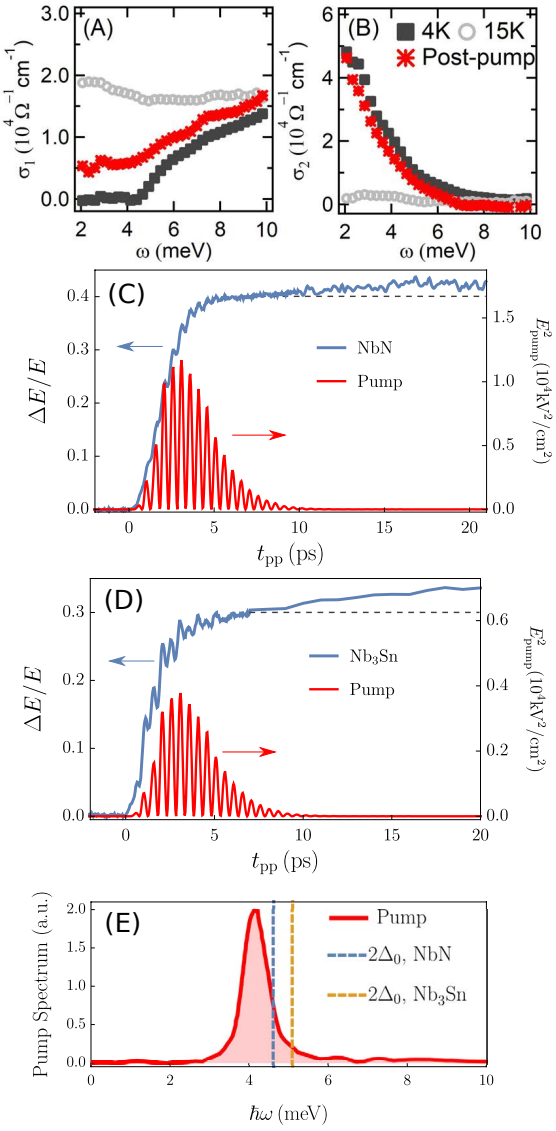

Figure 5.1: (Color online) Experimental results of time-domain THz pump-probe spectroscopy on NbN and Nb_3Sn thin films. Panels (A) and (B) show the real and imaginary parts of the optical conductivity σ_1 and σ_2 in NbN. Gray curves are equilibrium results at $T = 4$ K $< T_c = 13$ K (dark gray), and $T = 15$ K $> T_c$ (light gray). The red curve is taken $t_{\rm pp} = 10$ ps after a strong multi-cycle THz pump with peak electric field $E_{\rm pump} = 109$ kV/cm and duration $\tau = 10$ ps (shown in panel (C)). (C) Relative pump-induced change of transmitted probe field strength $\Delta E/E$ (blue curve) in NbN at fixed $t_{\rm gate}$. The red curve shows the pump profile. (D) $\Delta E/E$ versus t_{pp} at fixed $t_{\rm gate}$ in Nb_3Sn (blue curve). The red curve shows the pump profile, with a peak electric field of $E_{\rm pump} = 62$ kV/cm. (E) Frequency spectrum of the multi-cycle pump pulses. Most of the spectral weight lies below the optical gap in both NbN and Nb_3Sn (vertical lines). The weight at Δ_0, corresponding to the frequency of the Higgs (amplitude) mode, is also small.

$T_c(\mathrm{NbN}) \approx 13$ K is signaled by the opening of an optical gap in $\sigma_1(\omega)$ and by a $1/\omega$ dependence of $\sigma_2(\omega)$ at low frequencies. The gap reaches a low-temperature value of $2\Delta(\mathrm{NbN}) \approx 4.6$ meV at $T \ll T_c$ [127]. We then expose the sample to an intense, multi-cycle THz pump shown in Fig. 5.1 (C), whose spectral weight lies mostly below the optical gap (see Fig. 5.1 (E)). The post-pump state (red curve in panels (A, B)) exhibits larger values of $\sigma_1(\omega)$ within the 2Δ range, and slightly reduced values of $\sigma_2(\omega)$, due to the quench of the SC condensate.

To extract the ultrafast dynamics of the gap function $\Delta(t_{pp})$, we prepare the system in equilibrium at $T = 4$ K, expose it to an intense multi-cycle THz pump pulse and measure the relative change of the transmitted electric field amplitude of a delayed THz probe pulse due to the presence of the pump

$$\Delta E(t_{pp})/E \equiv \big[E(\text{pump on}, t_{pp}) - E(\text{off})\big]/E(\text{off}) \tag{5.1}$$

at a fixed gate time t_{gate}. In equilibrium, the relative change of the probe field transmission $\Delta E(T)/E \equiv [E(T) - E(T_0)]/E(T_0)$ with fixed (variable) temperature T_0 (T) was shown to faithfully reflect the behavior of the superconducting gap $\Delta E(T)/E \propto [\Delta(T) - \Delta_0]/\Delta_0$ [94, 103], where $\Delta_0 \equiv \Delta(T_0)$ and we use $T_0 = 4$ K. It was shown that this relationship also holds in non-equilibrium [103]. We determine the numerical value of the proportionality factor α in $\Delta E(t_{pp})/E = \alpha\big[1 - \Delta(t)/\Delta_0\big]$ by extracting the superconducting gap $\Delta(t)$ in non-equilibrium at $t_{pp} = 10$ ps from a fit of the optical conductivity in Figs. 5.1(A, B) to a generalized Mattis-Bardeen theory [129]. We find a numerical value of $\alpha_{\mathrm{NbN}} = 2.7$.

In Fig. 5.1(C), we show the observed ultrafast time evolution of $\Delta E/E = \alpha_{\mathrm{NbN}}[1 - |\Delta(t)|/\Delta_0]$ (blue curve), with initial state $\Delta_0 \equiv \Delta(T_0 = 4\ \mathrm{K}, t = 0)$ well inside the superconducting state. We also plot the applied pump pulse (red curve) in order to show that the gap $\Delta(t)$ oscillates with twice the pump frequency while the pump pulse is on. Interestingly, after the pump is turned off, the oscillations disappear quickly, and, most importantly, $\Delta(t)$ continues to decrease on the time scale of tens of picoseconds. This behavior continues before the gap eventually returns to its initial equilibrium value on nanosecond time scales *via* equilibration with phonons. This latter regime is not discussed in this paper.

Let us now describe our experimental results of Nb_3Sn, which are shown in Fig. 5.1(D). We expose the 20 nm thick Nb_3Sn films, that are initially prepared at low temperatures $T_0 = 4$ K$\ll T_c$ well inside the superconducting phase, to the same intense, multi-cycle THz pulse that we used for NbN. As the optical gap in Nb_3Sn is even larger $2\Delta(Nb_3Sn) = 5.1$ meV [105], the spectral weight of the pump pulse lies almost fully inside the gap (see Fig. 5.1 (E)). As a result, pair-breaking (by single photons) can be safely neglected. As shown in Fig. 5.1(D), we observe the same salient features as for NbN, which were described above. The suppression of the gap oscillations and the decrease of the average gap after the pulse has passed, however, are now even more pronounced. We note that we determine α_{Nb_3Sn} from $\Delta E(T)/E$ and find $\alpha_{Nb_3Sn} = 0.75$.

We would like to emphasize that although the pump pulse we used has a temporal width of the order of the inverse gap, the non-equilibrium dynamics is still far from the adiabatic regime. This is due to the fact that, for multi-cycle pulses, the characteristic time scale of the perturbation is determined by the period of the cycle, and the width of the pulse is less relevant. This is in sharp contrast to single-cycle pulses, where the characteristic time scale is determined by the pulse width [79]. We will theoretically analyze this issue systematically in the next section.

We note that, although the $\Delta E/E$ curve in Fig. 5.1(C) remains above the dashed line after the pump is off, the data displays noticeable noise. Such a noise likely arises from the high intensity of the pump used. Note, however, that using similarly high-intensity pumps, the data on Nb_3Sn shown in Fig. 5.1(D) is much less noisy, and displays the same decrease of the gap after the pump is turned off. Importantly, a similar behavior was reported previously in Ref. [93] for less intense single-cycle THz pulse experiments on NbN films. Notably, after the single-cycle pulse has passed, the average gap was reported to continue to decrease, an observation that was already mentioned explicitly in Ref. [93]. Thus, the suppression of the gap after the pump is turned off seems to be a much more generic occurrence in pump-and-probe experiments

5.3 Theoretical model and analysis

To model and understand the experimental results presented in Sec. 5.2, we first resort to standard time-dependent BCS theory. As shown in detail below, this fully coherent

approach, however, is unable to properly describe the experimental results. In particular, it cannot account for the rapid suppression of the gap oscillations and the continuing decrease of the average gap after the pump has passed. This motivates our new phenomenological approach that introduces two relaxation timescales T_1 and T_2 to include additional damping. This yields a much more accurate, quantitative description of the gap dynamics, for single-cycle pump pulses. To obtain quantitative agreement between theory and experiment for (off-resonant) multi-cycle pulses, we introduce an additional parameter η describing dissipation of energy out of the electronic subsystem into the environment. The timescales $T_{1,2}$ we extract from our "fit" turn out to be of the order of the pulse width, consistent with relaxation processes that occur within the electronic subsystem.

5.3.1 Coherent dynamics from the BCS model

Let us now explain our theoretical modeling in more detail. The starting point of our theoretical analysis is the BCS Hamiltonian

$$H_{\mathrm{BCS}} = \sum_{\boldsymbol{k},\sigma} \xi_{\boldsymbol{k}+e\boldsymbol{A}} c^\dagger_{\boldsymbol{k},\sigma} c_{\boldsymbol{k},\sigma} + \sum_{\boldsymbol{k}} \left(\Delta c^\dagger_{\boldsymbol{k},\uparrow} c^\dagger_{-\boldsymbol{k},\downarrow} + \mathrm{h.c.}\right) + \frac{|\Delta|^2}{V_0} \tag{5.2}$$

with square-lattice dispersion $\varepsilon_{\boldsymbol{k}} = -2J(\cos k_x + \cos k_y)$. Here, we have defined $\xi_{\boldsymbol{k}} = \varepsilon_{\boldsymbol{k}} - \mu$, and the chemical potential is set to $\mu = -1.18J$, corresponding to approximately quarter-filling. We note that the precise form of the energy dispersion is not important in the following, as we choose a filling sufficiently far away from the van Hove point and a generic light polarization. The superconducting order parameter obeys the self-consistency equation

$$\Delta = -V_0 \sum_{\boldsymbol{k}} \langle c_{-\boldsymbol{k},\downarrow} c_{\boldsymbol{k},\uparrow} \rangle \,, \tag{5.3}$$

where $V_0 > 0$ denotes an attractive interaction. Note that here we chose a new convention for the gap comparing to the previous chapters (Eq. 3.2), leading to an overall sign difference. In NbN and Nb_3Sn its origin is presumably rooted in electron-phonon interactions. For the calculations in this paper, we set $V_0 = 3J$ and the Debye frequency $\omega_{\mathrm{D}} = J/2$, yielding $\Delta_0 = 0.08J$ and $T_c = 0.048J$. The electronic density of states is almost constant in a window of size of the Debye frequency around the Fermi energy.

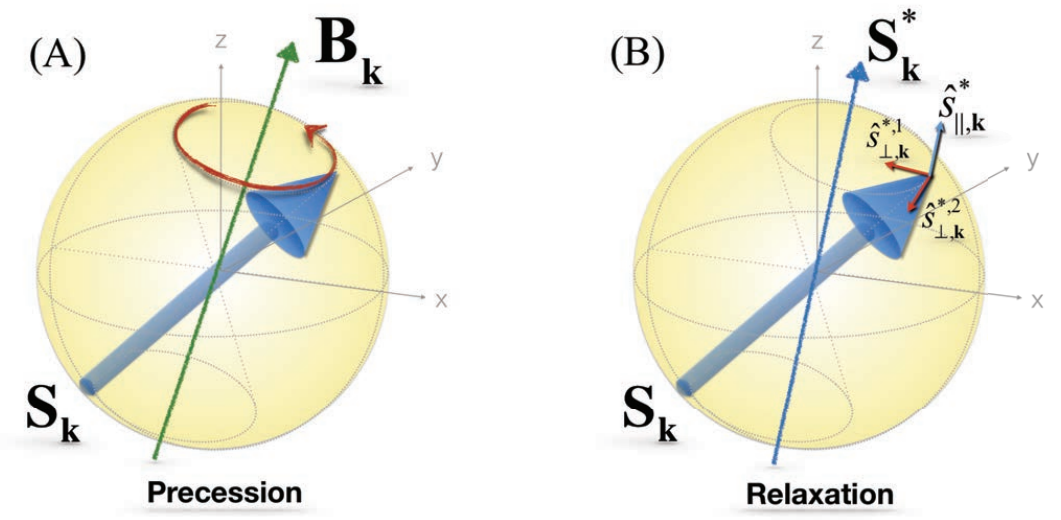

Figure 5.2: (A) Schematics of fully coherent pseudospin precession under the time-dependent pseudo-magnetic field $\boldsymbol{B_k}$ (green). (B) Schematics of the pseudospin relaxation towards the thermalized configuration $\boldsymbol{S}^*_{\boldsymbol{k}}$ showing the different effects of T_1 and T_2 processes.

The pump laser field is included in the Hamiltonian via the vector potential $\boldsymbol{A}(t)$. In our experiment, it takes the form

$$\boldsymbol{A}(t) = \hat{\boldsymbol{e}}_{\mathrm{p}} A_0 \theta(t)\theta(\tau - t) \exp\left[-\frac{(t-\tau/2)^2}{2\sigma^2}\right] \cos(\omega_{\mathrm{p}} t) \tag{5.4}$$

with linear polarization vector $\hat{\boldsymbol{e}}_{\mathrm{p}}$, center frequency ω_{p}, temporal width σ, and duration τ. The values of these parameters in the various simulations we perform are given in the figure captions.

To describe the gap dynamics, we introduce Anderson pseudospins [75]

$$\boldsymbol{S_k} = \psi^\dagger_{\boldsymbol{k}} \frac{\boldsymbol{\sigma}}{2} \psi_{\boldsymbol{k}} \tag{5.5}$$

with $\psi^\dagger_{\boldsymbol{k}} = (c^\dagger_{\boldsymbol{k},\uparrow}, c_{-\boldsymbol{k},\downarrow})$ being a Nambu spinor and $\boldsymbol{\sigma}$ a vector of Pauli matrices. The

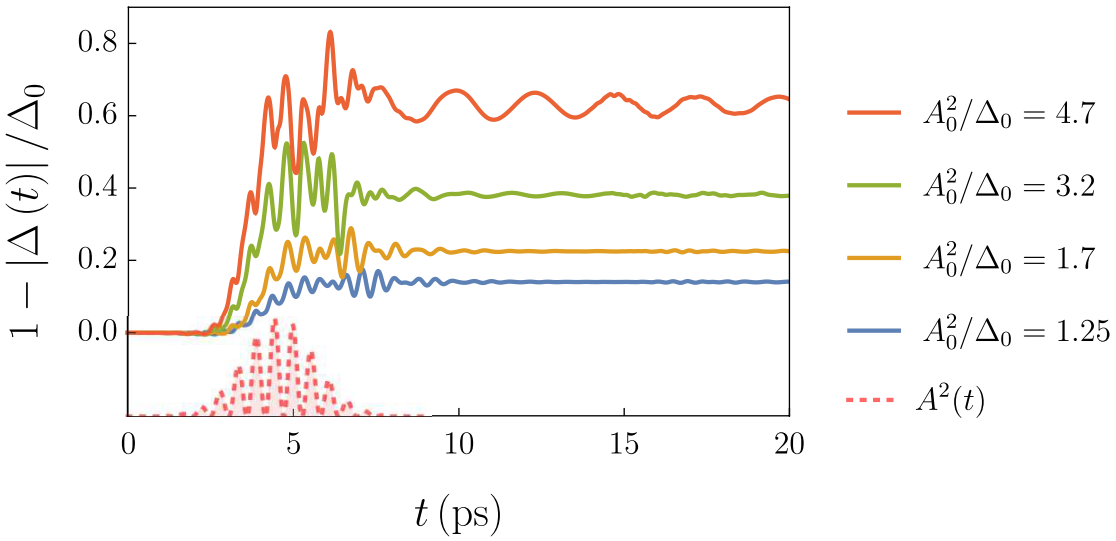

Figure 5.3: (Color online) Undamped BCS gap dynamics induced by multi-cycle THz pulses of various amplitude A_0^2/Δ_0. The pump pulse has duration $\tau = 10\pi/\Delta_0 = 8$ ps, width $\sigma = \tau/6$, center frequency $\omega_p = 1.65\Delta_0$ with $\Delta_0 = 2.55$ meV $= 2\pi \times 0.62$ THz. Its profile is shown at the bottom (red dashed). During the pump, the gap exhibits oscillations with multiples of $2n\omega_p$. While at lower amplitudes the $n = 1$ component is dominant, higher order $n > 1$ components (mainly $n = 2$) are non-zero for larger amplitudes $A_0^2/\Delta_0 = 3.2, 4.7$. After the pump, the gap exhibits slowly (algebraically) damped oscillations with frequency $2\Delta_\infty$ and increasing amplitude for increasing pump amplitude A_0.

Hamiltonian (5.2) then reads

$$H_{\mathrm{BCS}} = -\sum_{\boldsymbol{k}} \boldsymbol{B}_{\boldsymbol{k}} \cdot \boldsymbol{S}_{\boldsymbol{k}} + \frac{|\Delta|^2}{V_0} + \sum_{\boldsymbol{k}} \bar{\xi}_{\boldsymbol{k},\boldsymbol{A}} \tag{5.6}$$

with pseudo-magnetic field

$$\boldsymbol{B}_{\boldsymbol{k}} = -2(\Delta', -\Delta'', \bar{\xi}_{\boldsymbol{k},\boldsymbol{A}}) \tag{5.7}$$

where $\Delta = \Delta' + i\Delta''$, and $\bar{\xi}_{\boldsymbol{k},\boldsymbol{A}} = \frac{1}{2}(\varepsilon_{\boldsymbol{k}+e\boldsymbol{A}} + \varepsilon_{\boldsymbol{k}-e\boldsymbol{A}}) - \mu$. Note that the pseudo-magnetic field depends on the state of the pseudospins via the gap equation: $\Delta = -V_0 \sum_{\boldsymbol{k}} \langle S_{\boldsymbol{k}}^- \rangle$ (see Eq. (5.3)).

In the initial equilibrium state, all pseudospins are aligned with the field direction

$\boldsymbol{B}_{\boldsymbol{k}}$. Explicit expressions of the equilibrium spin state, and further details on the calculation are provided in Appendix C.2. The pump pulse $\boldsymbol{A}(t)$ then drives the system out of equilibrium by changing the band dispersion term via $B^z_{\boldsymbol{k}}$. Considering the time evolution governed by the standard BCS Hamiltonian (5.6) only, the pseudospins coherently precess around the new field direction $\boldsymbol{B}_{\boldsymbol{k}}(t)$ according to the Bloch equation (see also [25, 27, 119, 118, 82, 79, 121, 122, 123]):

$$\frac{d\langle \boldsymbol{S}_{\boldsymbol{k}} \rangle}{dt} = \langle \boldsymbol{S}_{\boldsymbol{k}} \rangle \times \boldsymbol{B}_{\boldsymbol{k}} \,. \tag{5.8}$$

We schematically depict the resulting coherent pseudospin dynamics in Fig. 5.2(A). Importantly, the pseudospin dynamics is immediately fed back into the pseudo-magnetic field via the gap equation (5.3). Due to parity symmetry, only even-order terms of $\boldsymbol{A}(t)$ appear [72, 75], and the oscillation frequency of the gap during the pump is a multiple of $2\omega_{\mathrm{p}}$. This can be clearly seen in Fig. 5.3, which shows a numerical solution of $\Delta(t)$ for different amplitudes A_0. The dynamical behavior while the pulse is turned on is in agreement with our experimental results in Fig. 5.1, except for the highest amplitudes.

While the gap oscillations with frequency $2\omega_{\mathrm{p}}$ in the presence of the pump are correctly captured, there are crucial, qualitative differences between the BCS-theoretical and the experimental gap dynamics in Fig. 5.1. One difference is that while the BCS-theoretical gap displays coherent, slowly decaying oscillations with an amplitude that is increasing with increasing A_0, experimentally the gap oscillations are absent once the pump is off in our multi-cycle experiments.

The most important *qualitative* difference, however, is that the average BCS-theoretical gap is completely flat after the pump pulse has passed, while the gap amplitude continues to decrease in the experiment. The long-time average (theoretical) gap is often denoted Δ_∞, and its value depends on the fluence A_0 of the pulse. The discrepancy between the theory and the data occurs for both NbN and Nb_3Sn thin films, which have different thicknesses, driven by either multi- or single-cycle pump pulses [93], and for different values of the pump intensity (for instance, the pump intensity is one order of magnitude smaller in the case of single-cycle pulses). Given that the Nb_3Sn sample is far cleaner than the NbN films (elastic low-temperature scattering rates are $\Gamma_{\mathrm{dis,\ Nb_3Sn}} \approx 7$ meV [105] and $\Gamma_{\mathrm{dis,\ NbN}} \approx 70$ meV), it is rather unlikely that the origin

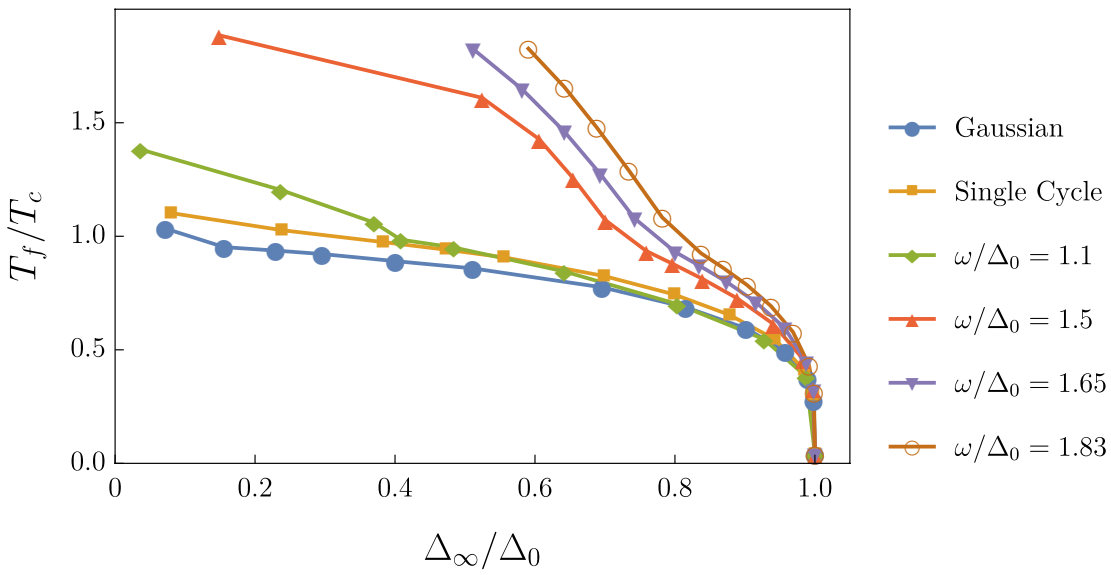

Figure 5.4: (Color online) Final equilibrium temperature T_f (normalized to T_c) as a function of gap quench amplitude Δ_∞/Δ_0 for undamped BCS model ($T_1 = T_2 = \infty$). Temperature T_f is obtained from the energy deposited by the pulse [see Eq. (5.11)], and different Δ_∞ are obtained by changing A_0. The different pulse types are parametrized by $(\tau, \sigma, \omega_p) = (2\pi/\Delta_0, \tau/8, 0)$ for the Gaussian pulse, $(10\pi/\Delta_0, \tau/5, 1.3\Delta_0)$ for the single-cycle pulse, and $(10\pi/\Delta_0, \tau/6, \omega_p)$ with ω_p given in the figure for the multi-cycle pulses. The polarization of the electric field is along $\hat{x}$.

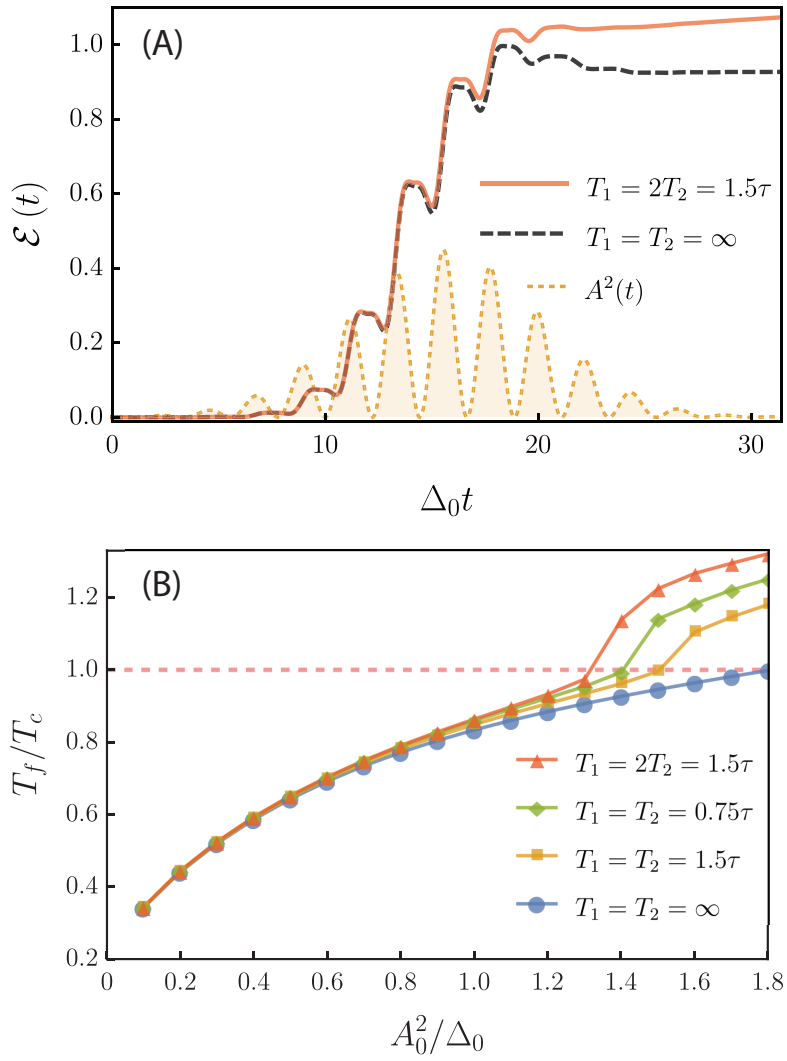

Figure 5.5: (Color online) (A) Time evolution of the internal energy $\mathcal{E}$ of the electronic system arising from the energy deposited by a multi-cycle pump pulse $A^2(t)$ (orange dashed) with amplitude $A_0^2/\Delta_0 = 1.1$, duration $\tau = 10\pi/\Delta_0$, width $\sigma = \tau/5$, and center frequency $\omega_p = 1.41\Delta_0$. The polarization of the electric field is along $\hat{x}$ and we set $\eta = 1$. Different curves correspond to $T_1 = T_2 = \infty$ (black dashed) and $T_1 = 2T_2 = 1.5\tau$ (orange solid) as indicated. The energy is normalized by $N_f\Delta_0^2$, where N_f is the density of states at the Fermi level. (B) The effective temperature after the pump is turned off, $T_f \equiv T^*(\tau)$, normalized by T_c, as a function of the pump intensity A_0^2 for various T_1 and T_2. For finite $T_{1,2}$, the system will relax to the normal state once $T_f > T_c$, which leads to an increased energy absorption, as indicated by the change of slope of T_f when crossing the red dashed line. The pulse parameters are identical to the ones in panel (A).

of the described phenomena lies in disorder-induced spatial gap inhomogeneities in the post-pump state. In addition, we do not observe the characteristic overshoot of the real part of the optical conductivity σ_1 in the post-pump state over the normal state, that is associated with spatial inhomogeneities and can be reproduced using Brggemann's effective medium theory [92].

The diversity of experimental setups showing the same effect suggests that it may have a common origin. One possible culprit is pair-breaking promoted by the pump, which is not included in the formalism above and would naturally lead to a suppression of the gap. While one cannot completely rule out this mechanism, particularly in the single-cycle case, where the pump frequency is comparable to 2Δ, our Fig. 5.1(E) shows that in the multi-cycle experiments nearly all the spectral weight of the pump is below 2Δ. As a result, we search for a different mechanism that does not require pair-breaking.

5.3.2 Phenomenological account of damping in pseudo-spin dynamics

To account for the experimental observations, we thus go beyond the standard BCS description and include phenomenologically damping in the pseudospin equations of motion. The microscopic origin of these terms will be discussed below. In analogy with the general problem of spin precession, we introduce longitudinal (T_1) and transverse (T_2) relaxation rates:

$$\begin{aligned}\frac{d\langle \boldsymbol{S_k}\rangle}{dt} =&\langle \boldsymbol{S_k}\rangle \times \boldsymbol{B_k} - \frac{\langle \boldsymbol{S_k}\rangle \cdot \hat{\boldsymbol{s}}^*_{\parallel,\boldsymbol{k}} - |\langle \boldsymbol{S^*_k}\rangle|}{T_1}\hat{\boldsymbol{s}}^*_{\parallel,\boldsymbol{k}} \\ &- \sum_{i=1}^{2} \frac{\langle \boldsymbol{S_k}\rangle \cdot \hat{\boldsymbol{s}}^{*,i}_{\perp,\boldsymbol{k}}}{T_2}\hat{\boldsymbol{s}}^{*,i}_{\perp,\boldsymbol{k}}\,. \end{aligned} \tag{5.9}$$

Here,

$$\langle \boldsymbol{S^*_k}\rangle\big[T^*(t)\big] = \frac{1}{2}\hat{\boldsymbol{s}}^*_{\parallel,\boldsymbol{k}}\big[T^*(t)\big]\tanh\Big(\frac{\sqrt{\xi^2_{\boldsymbol{k}}+\Delta^2_*}}{2T^*(t)}\Big) \tag{5.10}$$

is the thermalized pseudospin configuration at time t at an effective temperature T^* with gap value $\Delta_* \equiv \Delta(T^*)$. The two vectors $\hat{\boldsymbol{s}}^{*,i}_{\perp,\boldsymbol{k}}$ with $i = 1, 2$ span the plane perpendicular to the equilibrium pseudospin direction $\hat{\boldsymbol{s}}^*_{\parallel,\boldsymbol{k}}\big[T^*(t)\big]$. This is schematically depicted in Fig. 5.2(B) (see also Appendix C.2). Physically, the time scale T_1 is related to a redistribution of the quasi-particles, whereas the time scale T_2 is related to the

dephasing of the off-diagonal quasi-particle coherence, which governs the damping of the gap oscillations. We note that the notion of quasi-particles depends on the choice of Bogoliubov transformation that one performs as the gap evolves in time. Here, we refer to the transformation that diagonalizes the Hamiltonian for the thermalized gap value $\Delta(T^*)$ at effective temperature T^*.

To compute $\hat{\boldsymbol{s}}^*_{\parallel,\boldsymbol{k}}$ and the effective temperature T^*, we first consider that all the energy deposited in the electronic subsystem by the pump is converted into a change in the internal energy (see also Ref. [126]):

$$\mathcal{E}(t) = \langle H_{\mathrm{BCS}}(t)\rangle_{A=0} - \langle H_{\mathrm{BCS}}\rangle_{\mathrm{init}}\,. \tag{5.11}$$

Here, the expectation value is calculated in the time-evolved BCS state according to Eq. (5.9) and $\langle H_{\mathrm{BCS}}\rangle_{\mathrm{init}}$ is the initial ground state energy. From $\mathcal{E}(t)$, we extract both $T^*(t)$ and $\Delta_*(t) \equiv \Delta[T^*(t)]$, which are themselves function of time while the pump is turned on. Specifically, we use that the energy of the BCS state at temperature T is given by

$$\mathcal{E}(T) = \sum_{\boldsymbol{k}} \Big[\xi_{\boldsymbol{k}} - \big(1 - 2n_F[E_{\boldsymbol{k}}(T)]\big)E_{\boldsymbol{k}}(T)\Big] + \frac{|\Delta(T)|^2}{V_0}\,, \tag{5.12}$$

where $n_F(E) = 1/(\exp(E/T)+1)$ is the Fermi function, $E_{\boldsymbol{k}}(T) = \sqrt{\xi^2_{\boldsymbol{k}} + |\Delta(T)|^2}$ is the quasi-particle energy and the equilibrium gap $\Delta(T)$ is determined from the finite temperature gap equation $1 = V_0 \sum_{\boldsymbol{k}} \frac{\tanh(E_{\boldsymbol{k}}/2T)}{2E_{\boldsymbol{k}}}$. We then obtain Δ_* and T^* by setting $\mathcal{E}(t) = \mathcal{E}(T^*) - \mathcal{E}(T=0)$ and solving for these variables [23]. Here we used that $\langle H_{\mathrm{BCS}}\rangle_{\mathrm{init}} \equiv \mathcal{E}(T=0)$ in our simulation. Once the pump is turned off, energy is no longer deposited in the electronic subsystem, and thus $T^*(t>\tau) = T^*(\tau) \equiv T_f$, and $\Delta_*(t>\tau) \equiv \Delta_f$.

We have calculated T_f for a variety of Gaussian pulse shapes parametrized by τ, σ, ω_p and amplitudes A_0. In Fig. 5.4, we present the resulting T_f/T_c as a function of the long-time (average) non-equilibrium value of the gap Δ_∞/Δ_0 for different pulse shapes. Clearly, the amount of energy that is deposited into the system for a given quench amplitude of the gap $(1 - \Delta_\infty/\Delta_0)$ strongly depends on the pulse shape. Less energy is deposited if the pulse is resonant with the Higgs (amplitude) mode, which occurs if it

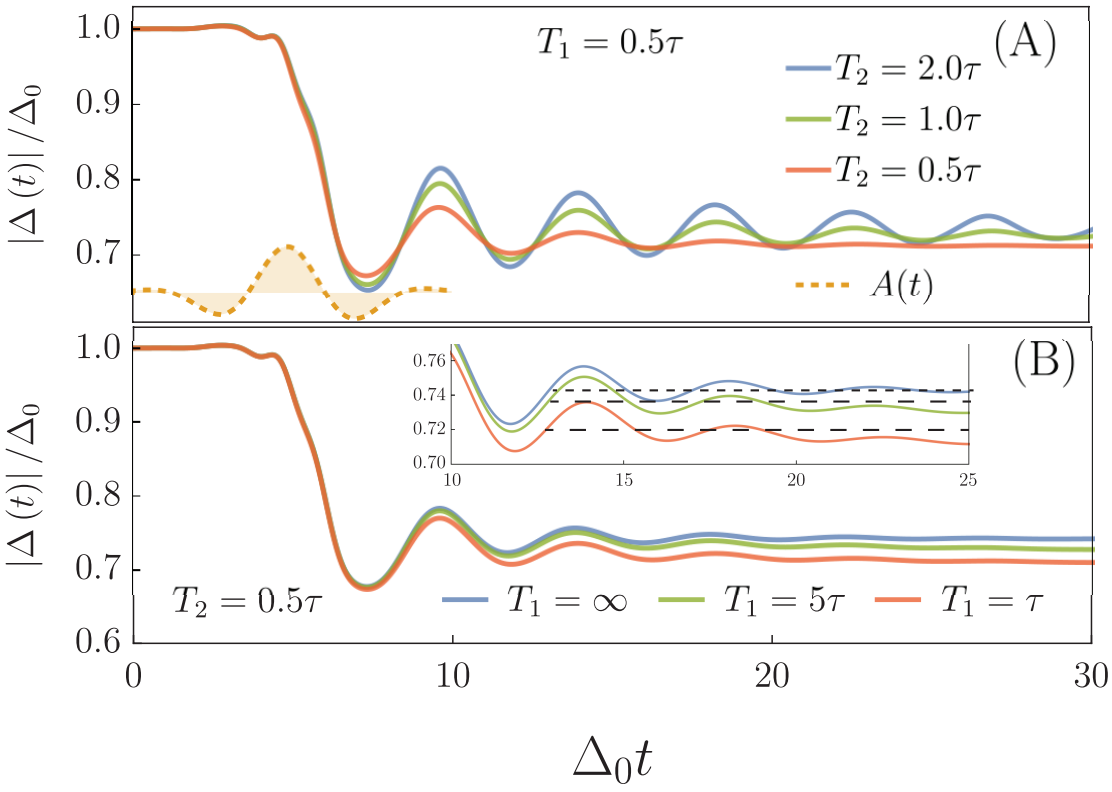

Figure 5.6: (Color online) Theoretical results for the gap dynamics $\Delta(t)/\Delta_0$ for short single-cycle Gaussian pump pulses with duration $\tau = 10/\Delta_0$ and width $\sigma = \tau/5$. Here, Δ_0 denotes the initial equilibrium gap value at $t = 0$. In panel (A), we keep $T_1 = 0.5\tau$ fixed and change T_2, whereas in panel (B) we set $T_2 = 0.5\tau$ and vary T_1. The pump pulse shape $A(t)$ is shown at the bottom of panel (A) (dashed). We set the pump amplitude to be $A_0 = \sqrt{1.12\Delta_0}$ in both panels. Inset in panel (B) highlights the post-pump behavior of the gap. One clearly observes deviations of the average gap value from the horizontal black dashed lines for finite T_1.

contains frequency components $\omega_p \approx \Delta_0$. The different behaviors can thus be grouped into two classes corresponding to resonant and off-resonant driving. Resonant pulses are short Gaussian pulses and single-cycle pulses with $\Delta_0\sigma \lesssim 1$, where σ is the width of the pulse, and longer multi-cycle pulses with center frequency $\omega_p \approx \Delta_0$. On the other hand, if the center frequency of the multi-cycle pulse is not resonant with the Higgs (amplitude) mode, the deposited energy is much larger. In order to quantitatively describe experimental data for off-resonant multi-cycle pulses, we will therefore introduce a third phenomenological parameter $0 < \eta \leq 1$, where $1 - \eta$ describes the fraction of energy that is dissipated from the electronic system into the environment. Thus, η describes the fraction of the energy that remains within the electronic subsystem. On short timescales, this energy loss can occur via scattering with electronic quasi-particles that are located outside the volume excited by the pump pulse. We found this time scale to be consistent with T_1.

Interestingly, the presence of relaxation also affects the amount of energy that is deposited into the electronic system during a pulse. In Fig. 5.5(A), we show the electronic energy $\mathcal{E}(t)$ for a multi-cycle pulse with center frequency $\omega_p = 1.4\Delta_0$ with and without relaxation, *i.e.*, for finite and infinite T_1 and T_2. We observe that more energy is deposited for finite $T_{1,2}$. This occurs as the faster damping of the Higgs (amplitude) mode generates excess quasi-particles that directly couple with light, which leads to greater energy absorption. In Fig. 5.5(B), we show how the final temperature T_f depends on the pump fluence A_0^2. As expected, for sufficiently strong pump pulses, the superconducting state can be completely melted by heating and $T_f > T_c$. Once this threshold is reached, the slope of the curves $T_f(A_0)$ becomes steeper, corresponding to a more rapid increase of T_f with increasing fluence in the normal state.

To elucidate how T_1 and T_2 affect the gap dynamics, and disentangle the contributions from these two relaxation processes, we systematically explore their effects in Fig. 5.6. For concreteness and to make connection to earlier experiments using single-cycle pulses [93], we consider a resonant single-cycle Gaussian-shaped pulse of duration $\tau = 10/\Delta_0 \approx 3$ ps, width $\sigma = \tau/5$ and center frequency $\omega_p = 1.3\Delta_0$. In Fig. 5.6(A), we fix $T_1 = 0.5\tau$ and vary T_2. It is apparent that the main effect of T_2 is to suppress the post-pump gap oscillations, while the decay of the average gap value after the pump is off is largely unaffected by changing T_2. Conversely, in Fig. 5.6(B), we keep $T_2 = 0.5\tau$

constant and vary T_1. While for $T_1 = \infty$ the average gap value is essentially constant after the pump is off, when $T_1 \sim \tau$ the average gap shows a clear and continuous suppression at long times. This behavior is highlighted in the inset. Note also that the amplitude of the post-pump gap oscillations are little affected by changing T_1.

5.4 Application to experimental results

We now apply our semi-phenomenological approach to describe experimental results for both single and multi-cycle experiments, and extract the damping timescales T_1 and T_2 from experiment. The values of T_1 and T_2 describe characteristic timescales of integrability-breaking interactions within the electronic subsystem. Using the equations of motion (5.9), we are able to quantitatively describe the experimentally observed gap dynamics in NbN for resonant single-cycle pulses. In order to reach a quantitative description for experiments on NbN and Nb_3Sn using slightly off-resonant multi-cycle pulses, we introduce an additional phenomenological parameter η, describing rapid energy dissipation out of the electronic subsystem into the environment on picosecond timescales. Technically, we use $\eta\mathcal{E}(t)$ to calculate Δ^* and T^* and let the system relax towards the corresponding pseudospin configuration according to Eq. (5.10).

5.4.1 Comparison to resonant single-cycle pulse experiments

In Fig. 5.7, we demonstrate that our theory can quantitatively describe experimental results on NbN for short single-cycle pulses that were published in Ref. [93]. Both the rapid damping of the oscillations and the continuing decrease of the average gap after the pump is off (shown by the increasing deviation from the dashed gray lines in the figure) can be quantitatively described by $T_1 = 1.5\tau$ and $T_2 = 0.3\tau$. These timescales are thus of the order of the pump duration which is approximately $\tau \approx 3$ ps. We do not need the additional parameter η, which is set to $\eta = 1$ here.

To make this comparison, we have rescaled the time axis using the equilibrium gap value $\Delta_0 = 0.36$ THz in the experiment. The experimental y axis in Ref. [93], $\Delta E_{\text{probe}} \propto 1 - \Delta(t)/\Delta_0$, is given in arbitrary units, and we have rescaled it by a factor of 0.345 (0.341) for the two lowest (the highest) pump fluence. We note that these rescaling factors yield the correct Δ_∞ within error bars, which were independently

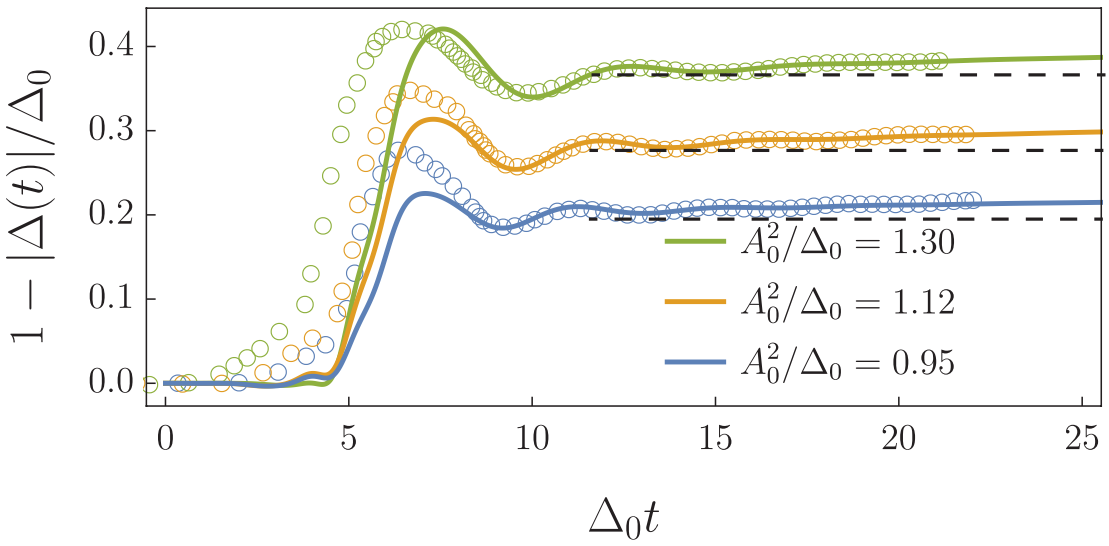

Figure 5.7: (Color online) Comparison between theory (solid lines) and single-cycle pump experiments on NbN published in Ref. [93](data points are for fluences 5.6, 6.4, and 7.2 nJ/cm^2). We set $\tau = 10/\Delta_0$, $\sigma = \tau/5$ for the two lowest pump fluences and $\sigma = \tau/7$ for the highest one. We find good agreement using the phenomenological parameters $T_1 = 1.5\tau$ and $T_2 = 0.3\tau$. The horizontal and vertical experimental axes were rescaled as explained in the main text. Note that the average gap value decreases after the pulse is off, which is clearly seen by the deviation from the dashed horizontal lines.

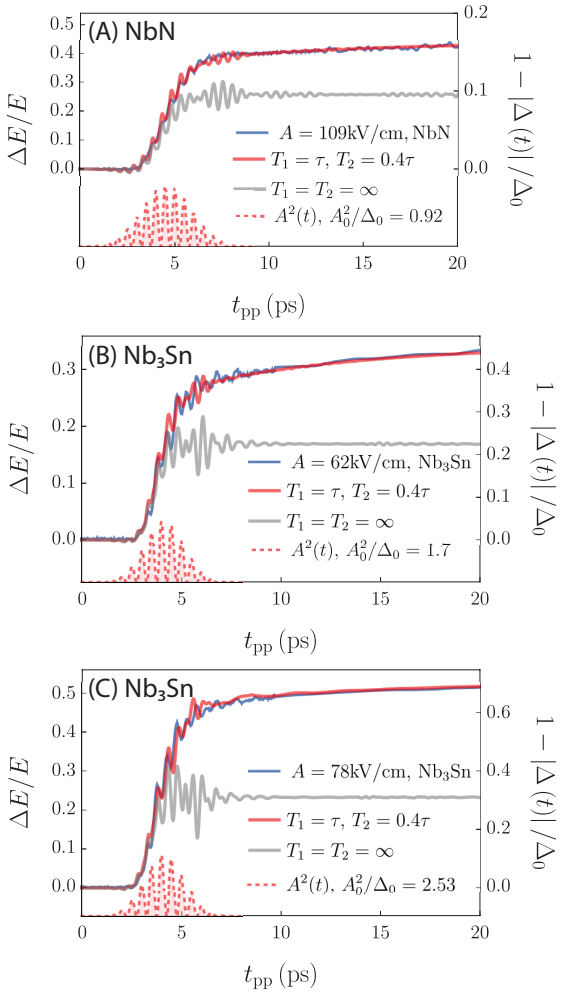

Figure 5.8: (Color online) Theory-experiment comparison for slightly off-resonant multi-cycle pulses. Panel (A) is for NbN and panels (B, C) are for Nb_3Sn. The experimental trace of $\Delta E(t)/E$ is shown in blue and converted into $1-|\Delta(t)|/\Delta_0 = \alpha^{-1}\Delta E/E$ using the procedure described in Sec. 5.2 with $\alpha_{\rm NbN} = 2.7$ and $\alpha_{\rm Nb_3Sn} = 0.75$. The gray line is obtained using pure BCS theory without any relaxation terms, and the red line is our phenomenological theory parametrized by relaxation parameters T_1, T_2 and η. In order to make quantitative comparison, the experimental traces are shifted to the right by 2.73 ps for NbN and 2.7 ps for Nb_3Sn to compensate the differences between the experimentally determined and the theoretically determined $t_{\rm pp}$. The duration and width of the Gaussian pump pulses (shown at the bottom) are $\tau = 10\pi/\Delta_0$ and $\sigma = \tau/5$ ($\tau/6$) for NbN (Nb_3Sn), and the center frequencies are $\omega_p = 1.83\Delta_0$ ($1.65\Delta_0$) for NbN (Nb_3Sn), which are taken from experiment. The polarization used in the theoretical calculation is along $\hat{x}$. We used an energy dissipation factor $\eta = 0.66, 0.72, 0.6$ for panels A, B, C. The other parameters $T_{1,2}$ and pump amplitude A_0^2 are given in the figure. We notice that the thermalized gap value $\Delta(T_f)$ is much smaller than the non-thermal BCS steady-state value Δ_∞, even though we use $\eta < 1$ [23]. Note that we find good quantitative agreement between the phenomenological theory and experiment both during and after the pump pulse.

measured in the experiment. We note that Ref. [93] includes results for ΔE, while we report $\Delta E/E$ in our experiments to measure the gap. There is thus a proportionality factor between the two procedures, and we do not expect to find the same numerical value for α_{NbN} in the two cases. Finally, we have shifted the origin of the experimental time t_{pp} axis by 1.73 ps, 1.68 ps and 1.36 ps for the three pump fluences 5.6, 6.4 and 7.2 nJ/cm^2, respectively, with respect to our simulations. This reflects the fact that t_{pp} is measured from the peak of the approximately 3 ps broad pump pulse, which occurs about halfway through the pulse [93].

5.4.2 Comparison to slightly off-resonant multi-cycle pulse experiments

A direct comparison of our theory to experimental results for the gap dynamics induced by multi-cycle THz pump pulses in NbN and Nb_3Sn is shown in Figs. 5.8 and 5.9. The pulse parameters are set to their experimental values. Specifically, pulse durations and widths are $\tau = 10\pi/\Delta_0$ and $\sigma = \tau/5$ ($\tau/6$) and the center frequencies are $\omega_p = 1.83\Delta_0$ ($1.65\Delta_0$) for NbN (Nb_3Sn). The pump pulses are therefore slightly off-resonant with the Higgs (amplitude) mode, which occurs at $\omega = \Delta_0$. Here, $\Delta_0 = 2.3$ meV $= 2\pi \times 0.55$ THz for NbN, and $\Delta_0 = 2.55$ meV$=2\pi \times 0.62$ THz for Nb_3Sn. This results in a pump duration of $\tau = 9$ ps (8 ps) for NbN (Nb_3Sn). The pump profiles are shown in the figures. The pump pulse spectra are shown in Fig. 5.1(E), demonstrating that both pulses only carry small spectral weight at Δ_0 and above the optical gap $2\Delta_0$. As shown in Fig. 5.4, the amount of energy that is deposited in such an off-resonant multi-cycle pulse within BCS theory increases rapidly with an increasing gap quench amplitude $1 - \Delta_\infty/\Delta_0$. It exceeds the condensation energy (such that $T_f > T_c$) for $1 - \Delta_\infty/\Delta_0 \gtrsim 0.75$. In our theoretical analysis, we initially prepare the system in the equilibrium state at the initial experimental temperature $T = 4$ K, which is much smaller than T_c of both NbN and Nb_3Sn samples. The redistribution of initially present thermal quasi-particles due to the pump pulse, which was shown to be an important factor at intermediate temperatures [104], is fully taken into account, but plays a minor role in our case as $T \ll T_c$.

We can fit the gap dynamics for multi-cycle pulses within our phenomenological model in two ways: (i) we introduce an additional parameter $\eta < 1$, which describes

the fraction of the internal energy that remains in the electronic subsystem pumped by the laser. In this case, we find that the data can be well described using relaxation timescales T_1 and T_2 that are of the order of the pulse duration τ. This is just like in the fit to the resonant single-cycle pulses in Fig. 5.7, for which $\eta = 1$. Alternatively, we (ii) enforce energy conservation within the electronic subsystem and set $\eta = 1$. To describe the data, we have to then use values of T_1 and T_2 that are about one order of magnitude larger than in the case of the resonant pulse.

In Fig. 5.8, we show theory-experiment comparison including the parameter $\eta < 1$. Besides the Nb_3Sn data shown in Fig. 5.1 (C), we also include data taken at a higher pump fluence. We find excellent quantitative agreement over the complete time interval and for all pump strengths. In contrast to the case with no damping, $T_1 = T_2 = \infty$ (gray lines), we find that the oscillations of $|\Delta(t)|$ are quickly suppressed after the pulse is turned off, and, more importantly, that a continuous and slow increase of $1 - |\Delta(t)|/\Delta_0$ takes place over the time scale of tens of picoseconds. The numerical values we obtain from comparing to the data are $\eta \approx 0.6 - 0.7$, and damping parameters that are of the order of the pulse width: $T_1 = \tau \approx 2T_2$, where $\tau \approx 10$ ps. The amplitude of the pulse is adjusted such that the final value of the gap matches the experimental one. Since the timescales $T_1, T_2 \lesssim \tau$, thermalization sets in while the pulse is on, and the undamped BCS result converges to a much smaller gap value at long times than the solution in the presence of relaxation.

In Fig. 5.9, we enforce energy conservation within the electronic subsystem by setting $\eta = 1$. Agreement is then limited to the time after the pump pulse is off and for not too large fluences. During the pulse and for large fluence, our phenomenological theory with $\eta = 1$ predicts gap oscillations with an amplitude that is larger than is observed experimentally. As $T_1, T_2 \gg \tau$, there is only a small difference between the damped and undamped gap dynamics while the pump is on. After the pulse, the damped solution slowly approaches the thermalized gap with a slope dictated by T_1, while the undamped solution is completely flat.

5.4.3 Summary of theory-experiment comparison

To summarize, using our phenomenological extension of BCS theory, we can quantitatively describe gap dynamics in resonant single-cycle experiments, both during and after

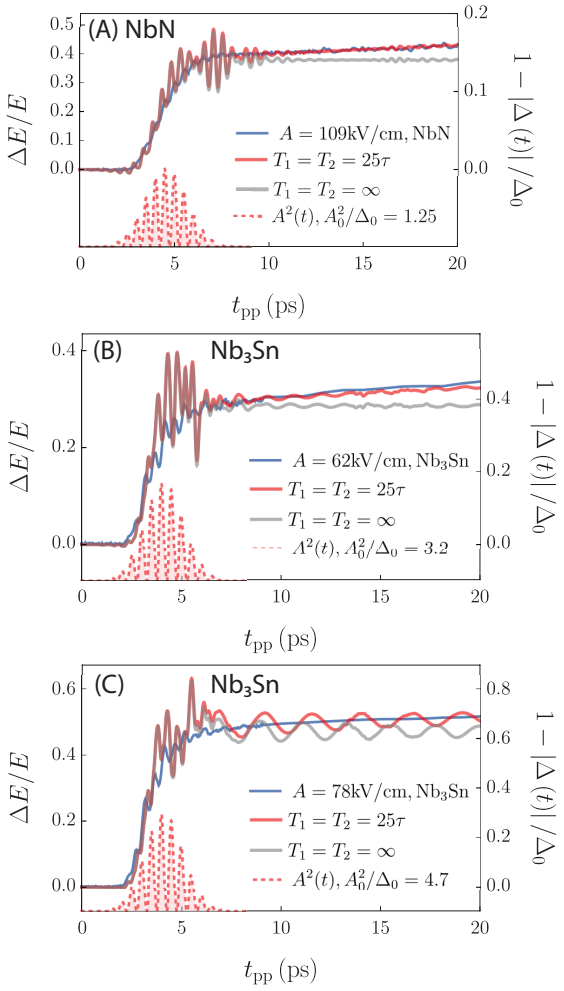

Figure 5.9: (Color online) Theory-experiment comparison for slightly off-resonant multi-cycle pulses, enforcing energy conservation in the electronic subsystem by setting $\eta = 1$. Panel (A) is for NbN and panels (B, C) are for Nb_3Sn. Blue line corresponds to experimental data (see Fig. 5.8 for details), red line is the fit to the phenomenological theory with values for T_1 and T_2 given in the panels and $\eta = 1$. Gray line is the undamped BCS result. In order to make quantitative comparison, the experimental traces are shifted to the right by 2.41 ps for NbN and 2.1 ps for Nb_3Sn to compensate the differences between the experimentally determined and the theoretically determined t_{pp}. The values for the center frequency ω_p, pulse width σ and duration τ are equal to the ones in the corresponding panels of Fig. 5.8. For $\eta = 1$, the relaxation parameters T_1 and T_2 have to be chosen much larger than in Fig. 5.8, and the pump amplitude A_0 has to be also adjusted to a larger value. Good agreement between theory and experiment is limited to times after the pump pulse is off and to lower gap quench amplitudes (panels A and B). During the pulse and for larger quench amplitudes, the theory with $\eta = 1$ predicts gap oscillations that are too large compared to our experimental observations. The fact that T_1 and T_2 have to be set to much larger values than in Figs. 5.7 and 5.8 signals the need to include the dissipation parameter η in our theory to quantitatively describe gap dynamics for off-resonant multi-cycle pulses.

the pump pulse (up to ≈ 20 ps, when additional relaxation mechanisms with the lattice set in). The extracted relaxation timescales T_1 and T_2 are found to have comparable values, which are of the order of the pulse duration $\tau = 10/\Delta_0 = 3$ ps. This is consistent with our assumption that the relaxation processes responsible for the behaviors observed experimentally take place within the electronic subsystem and are associated with the energy deposited in this subsystem while the pump is on. Our theory accounts both for the absence of gap oscillations after the pump pulse, and the overall decay of the average gap after the pump pulse has passed.

To describe off-resonant multi-cycle pulse experiments, we have performed two different fitting procedures: (i) by introducing an additional energy dissipation parameter $\eta < 1$, we can quantitatively describe the experimental gap dynamics using $T_1 \approx 2T_2 \approx \tau$ that are again of the order of the pulse duration $\tau \approx 8$ ps. The dissipation parameter takes values of $\eta \approx 0.6 - 0.7$ corresponding to the fact that about 30% of the energy deposited by the pump pulse is dissipated to the environment on a timescales of τ. Alternatively, (ii) we have enforced energy conservation within the electronic subsystem by setting $\eta = 1$. In this case, we find that $T_1 = T_2 = 25\tau$ need to be chosen about an order of magnitude larger than before, and we find a reasonable but less quantitative description of the data. This suggests that rapid energy dissipation out of the electronic subsystem occurs in the experiment when off-resonant pumps are used, which must be taken into account theoretically.

Although T_1, T_2 and η are phenomenological quantities, it is important to discuss their possible microscopic origins. The key point is that the $T_{1,2}$ processes arise within the electronic subsystem, before equilibration with the lattice sets in. Because the BCS Hamiltonian is integrable [91, 27, 26, 100, 130], any thermalization must arise from non-BCS effects. Residual interactions between the Bogoliubov quasi-particles, which are neglected in the mean-field BCS approach, could provide a mechanism for quasi-particle relaxation, which affects T_1. Moreover, the Higgs (amplitude) mode excited resonantly by the laser pump disperses into the quasi-particle continuum [131, 132]. As a result, one expects damping of the amplitude mode, which should affect the T_2 process. The parameter η describes rapid dissipation of energy out of the electronic subsystem. One possible origin of this process is electronic scattering with electronic degrees of freedom that are outside of the pump excitation volume. The lateral focal size of the pump is

1.2 mm. Future work should address a more microscopic derivation of damping effects in non-equilibrium superconductors.

Our theory accounts both for the absence of gap oscillations after the pump pulse, and the overall decay of the average gap after the pump pulse has passed. As shown in Figs. 5.8 and 5.9, although the behavior after the pump is off is very well captured quantitatively by our model, there are discrepancies between the theoretical and experimental curves while the pump is on. They are more pronounced for stronger pump intensities. Whether they originate from interference effects between the external drive (with centering frequency ω_0) and the tendency of the (closed) system to oscillate with frequency Δ_∞, or are caused by a different non-linear effect, deserves further attention. Here, our focus is on the behavior after the pump pulse has passed.

5.5 Conclusions

In this paper, we established a semi-phenomenological framework that allows one to incorporate damping beyond BCS theory in the picosecond time-evolution of the gap function of an s-wave superconductor subject to an intense THz pulse. In the pseudospin language, damping arises from a longitudinal process T_1, which is related to quasi-particle relaxation, and from a transverse process T_2, which is related to dephasing of off-diagonal quasi-particle coherence. We have found that T_1 mainly affects the post-pump average gap value, while T_2 mainly affects the post-pump gap oscillations. In addition, to account for rapid dissipation of energy, which is deposited by the pump, out of the electronic subsystem, we introduce a third parameter η. We find that dissipation processes become important for off-resonant multi-cycle pulses, where the pump necessarily deposits a significant amount of energy in order to quench the gap.

We apply our theory to resonant single-cycle pump pulse experiments on NbN thin films, and to off-resonant multi-cycle pulse experiments on NbN and Nb_3Sn films. We find excellent quantitative agreement for T_1 and T_2 values that are comparable to the duration of the pump pulse, $\tau = 3(8)$ ps for single-cycle (multi-cycle) experiments. For off-resonant pump pulses, where the energy deposited exceeds the condensation energy, we find that about 30% of the energy is rapidly dissipated out of the electronic subsystem. Possible microscopic origins of these phenomenologically introduced processes are

scattering of quasi-particles, interaction of the Higgs (amplitude) mode with the quasi-particle continuum, and interactions between quasi-particles inside and outside the focal region of the pump pulse. Future work should develop a microscopic underpinning of this phenomenological framework.

While the picosecond evolution of the gap function in NbN and Nb_3Sn is different than that expected for coherent BCS-like dynamics, we show that it is consistent with relaxation processes that arise within the electronic subsystem and have a time scale much shorter than lattice relaxation rates. Future application of this approach to different superconductors will shed light on the relevance of the distinct types of relaxation and dissipation processes for each system.

Chapter 6

Conclusion

Strongly correlated materials are such fascinating electronic systems that researchers keep getting surprises by discovering new phases in their already rich phase diagrams. In my thesis, I explored the phase diagram in two additional axes: the amount of quench disorder and the distance away from equilibrium. Since most strongly correlated materials are complex chemical compounds with various types of doping, it is fundamental to investigate how robust the clean phase diagram is against the effects of random disorders. In addition, recent developments in ultra-fast optical techniques bring a whole new possibility on experimentally investigating the non-equilibrium properties at femtosecond time scales. Thus, it is important to have a better theoretical understanding of the transient dynamics of strongly correlated electrons.

In Chapter 2, I investigated the nematic quantum phase transitions in inhomogeneous systems. Particularly, I showed that the effects of isolated clean droplets in the system with quench disorder can dramatically change the critical behavior of the nematic transition. The first-order nematic transition is not only smeared due to the presence of the isolated clean droplets but also behaves like a continuous transition since the moderate size droplets can undergo second-order nematic quantum phase transitions before the rest of the system. These findings have potential applications on explaining experimental results in iron-based systems.

In Chapter 3, I discussed the non-equilibrium dynamics of the superconducting gap in conventional single-band systems after an interaction quench. I showed the integrability of the BCS model and the subtleties associated with the conservation laws. I also

proposed a self-consistent perturbative approach to extract the asymptotic dynamics of the superconducting gap. By comparing it with the exact solution, I showed that the perturbative approach works with very high accuracy in the weak quench limit. Moreover, it is capable to correctly capture the asymptotic value of the gap for arbitrary quench strengths.

In Chapter 4, I showed the distinct transient dynamics of the superconducting gap in multi-band systems, comparing it with the single-band cases. In multi-band system, the gap exhibits beating oscillations due to multiple oscillation frequencies associated with multiple superconducting gaps. By applying the self-consistent perturbative approach proposed in Chapter 3, I was able to obtain the analytical expression for the gap oscillations and showed that the oscillations are damped as $t^{-3/2}$. This indicates that multi-band superconductors can host exotic non-equilibrium properties.

In Chapter 5, I incorporated damping effects to the gap oscillations in conventional superconductors to explain the THz pump-probe experiments on NbN and Nb_3Sn thin films. Using a semi-phenomenological model that incorporates damping within the electronic subsystem, we were able to achieve quantitative agreements with various experimental results with different pulse shapes of the pump. We argued that the interplay between the amplitude mode of the gap and the quasiparticle continuum is responsible for the rapid damping of the gap oscillation at the picosecond time scale. Therefore, a microscopic theory on the relaxation and damping processes within the electronic subsystem at non-equilibrium states requires physics beyond the classic BCS model.

References

[1] The rise of quantum materials. *Nature Physics*, 12:105, Feb 2016.

[2] B Keimer and J E Moore. The physics of quantum materials. *Nature Physics*, 13:1045, Oct 2017.

[3] Yoshinori Tokura, Masashi Kawasaki, and Naoto Nagaosa. Emergent functions of quantum materials. *Nature Physics*, 13:1056, Sep 2017.

[4] B Keimer, S A Kivelson, M R Norman, S Uchida, and J Zaanen. From quantum matter to high-temperature superconductivity in copper oxides. *Nature*, 518:179, Feb 2015.

[5] Pierre-Gilles de. Gennes. *The physics of liquid crystals*. Clarendon Press, Oxford [England], 1993.

[6] Paul M Chaikin and Tom C Lubensky. *Principles of condensed matter physics*, volume 1. Cambridge university press Cambridge, 2000.

[7] Eduardo Fradkin, Steven A. Kivelson, Michael J. Lawler, James P. Eisenstein, and Andrew P. Mackenzie. Nematic Fermi fluids in condensed matter physics. *Annual Review of Condensed Matter Physics*, 1(1):153–178, 2010.

[8] R. M. Fernandes, a. V. Chubukov, and J. Schmalian. What drives nematic order in iron-based superconductors? *Nature Physics*, 10(2):97–104, 2014.

[9] Rafael M. Fernandes, Peter P. Orth, and Jörg Schmalian. Intertwined vestigial order in quantum materials: Nematicity and beyond. *Annual Review of Condensed Matter Physics*, 10(1):133–154, 2019.

[10] M. M. Fogler, A. A. Koulakov, and B. I. Shklovskii. Ground state of a two-dimensional electron liquid in a weak magnetic field. *Phys. Rev. B*, 54:1853–1871, Jul 1996.

[11] S A Kivelson, E Fradkin, and V J Emery. Electronic liquid-crystal phases of a doped Mott insulator. *Nature*, 393(6685):550–553, Jun 1998.

[12] Chen Fang, Hong Yao, Wei-Feng Tsai, JiangPing Hu, and Steven A. Kivelson. Theory of electron nematic order in LaFeAsO. *Phys. Rev. B*, 77:224509, Jun 2008.

[13] Cenke Xu, Markus Müller, and Subir Sachdev. Ising and spin orders in the iron-based superconductors. *Phys. Rev. B*, 78:020501, Jul 2008.

[14] R. M. Fernandes, A. V. Chubukov, J. Knolle, I. Eremin, and J. Schmalian. Preemptive nematic order, pseudogap, and orbital order in the iron pnictides. *Physical Review B*, 85(2):024534, Jan 2012.

[15] VL Ginzburg and LD Landau. Phenomenological theory. *J. Exp. Theor. Phys. USSR*, 20:1064, 1950.

[16] A B Harris. Effect of random defects on the critical behavior of Ising models. *Journal of Physics C: Solid State Physics*, 7(9):1671–1692, May 1974.

[17] Thomas Vojta and Rastko Sknepnek. Critical points and quenched disorder: From Harris criterion to rare regions and smearing. *physica status solidi (b)*, 241(9):2118–2127, June 2004.

[18] John A. Hertz. Quantum critical phenomena. *Phys. Rev. B*, 14:1165–1184, Aug 1976.

[19] Thomas Vojta. Rare region effects at classical, quantum and nonequilibrium phase transitions. *Journal of Physics A: Mathematical and General*, 39(22):R143, 2006.

[20] Claudio Giannetti, Massimo Capone, Daniele Fausti, Michele Fabrizio, Fulvio Parmigiani, and Dragan Mihailovic. Ultrafast optical spectroscopy of strongly correlated materials and high-temperature superconductors: a non-equilibrium approach. *Adv. Phys.*, 65(2):58–238, 2016.

[21] A. F. Kemper, M. A. Sentef, B. Moritz, J. K. Freericks, and T. P. Devereaux. Direct observation of Higgs mode oscillations in the pump-probe photoemission spectra of electron-phonon mediated superconductors. *Phys. Rev. B*, 92:224517, Dec 2015.

[22] Ryusuke Matsunaga and Ryo Shimano. Nonlinear terahertz spectroscopy of Higgs mode in s-wave superconductors. *Physica Scripta*, 92(2):024003, Jan 2017.

[23] R. A. Barankov and L. S. Levitov. Synchronization in the BCS pairing dynamics as a critical phenomenon. *Phys. Rev. Lett.*, 96:230403, Jun 2006.

[24] Tianbai Cui and Rafael M. Fernandes. Smeared nematic quantum phase transitions due to rare-region effects in inhomogeneous systems. *Phys. Rev. B*, 98:085117, Aug 2018.

[25] A F Volkov and Sh M Kogan. Collisionless relaxation of the energy gap in superconductors. *J. Exp. Theor. Phys.*, 38(5):1018, 1974.

[26] Emil A. Yuzbashyan, Oleksandr Tsyplyatyev, and Boris L. Altshuler. Relaxation and persistent oscillations of the order parameter in fermionic condensates. *Phys. Rev. Lett.*, 96:097005, Mar 2006.

[27] Emil A Yuzbashyan, Boris L Altshuler, Vadim B Kuznetsov, and Victor Z Enolskii. Solution for the dynamics of the BCS and central spin problems. *J. Phys. A: Math. Gen.*, 38(36):7831–7849, Aug 2005.

[28] Emil A. Yuzbashyan, Vadim B. Kuznetsov, and Boris L. Altshuler. Integrable dynamics of coupled Fermi-Bose condensates. *Phys. Rev. B*, 72:144524, Oct 2005.

[29] Tianbai Cui, Michael Schütt, Peter P. Orth, and Rafael M. Fernandes. Post-quench gap dynamics of two-band superconductors. *arXiv e-prints*, page arXiv:1908.06125, Aug 2019.

[30] Tianbai Cui, Xu Yang, Chirag Vaswani, Jigang Wang, Rafael M. Fernandes, and Peter P. Orth. Impact of damping on the superconducting gap dynamics induced by intense terahertz pulses. *Phys. Rev. B*, 100:054504, Aug 2019.

[31] S A Kivelson, E Fradkin, and V J Emery. Electronic liquid-crystal phases of a doped Mott insulator. *Nature*, 393(6685):550–553, Jun 1998.

[32] Matthias Vojta. Lattice symmetry breaking in cuprate superconductors: stripes, nematics, and superconductivity. *Advances in Physics*, 58(6):699–820, 2009.

[33] Yuxuan Wang and Andrey Chubukov. Charge-density-wave order with momentum $(2Q, 0)$ and $(0, 2Q)$ within the spin-fermion model: Continuous and discrete symmetry breaking, preemptive composite order, and relation to pseudogap in hole-doped cuprates. *Phys. Rev. B*, 90:035149, Jul 2014.

[34] Michael Schütt and Rafael M. Fernandes. Antagonistic in-plane resistivity anisotropies from competing fluctuations in underdoped cuprates. *Phys. Rev. Lett.*, 115:027005, Jul 2015.

[35] Laimei Nie, Akash V. Maharaj, Eduardo Fradkin, and Steven A. Kivelson. Vestigial nematicity from spin and/or charge order in the cuprates. *Phys. Rev. B*, 96:085142, Aug 2017.

[36] K. Hashimoto, K. Cho, T. Shibauchi, S. Kasahara, Y. Mizukami, R. Katsumata, Y. Tsuruhara, T. Terashima, H. Ikeda, M. A. Tanatar, H. Kitano, N. Salovich, R. W. Giannetta, P. Walmsley, A. Carrington, R. Prozorov, and Y. Matsuda. A sharp peak of the zero-temperature penetration depth at optimal composition in $BaFe_2(As_{1-x}P_x)_2$. *Science*, 336(6088):1554–1557, Jun 2012.

[37] B. J. Ramshaw, S. E. Sebastian, R. D. McDonald, James Day, B. S. Tan, Z. Zhu, J. B. Betts, Ruixing Liang, D. A. Bonn, W. N. Hardy, and N. Harrison. Quasiparticle mass enhancement approaching optimal doping in a high-Tc superconductor. *Science*, 348(6232):317–320, Apr 2015.

[38] Ian M Hayes, Ross D McDonald, Nicholas P Breznay, Toni Helm, Philip J W Moll, Mark Wartenbe, Arkady Shekhter, and James G Analytis. Scaling between magnetic field and temperature in the high-temperature superconductor $BaFe_2(As_{1-x}P_x)_2$. *Nature Physics*, 12:916, May 2016.

[39] Yoni Schattner, Samuel Lederer, Steven A. Kivelson, and Erez Berg. Ising nematic quantum critical point in a metal: A Monte Carlo study. *Phys. Rev. X*, 6:031028, Aug 2016.

[40] Yang Qi and Cenke Xu. Global phase diagram for magnetism and lattice distortion of iron-pnictide materials. *Phys. Rev. B*, 80:094402, Sep 2009.

[41] A. J. Millis. Fluctuation-driven first-order behavior near the $T = 0$ two-dimensional stripe to Fermi liquid transition. *Phys. Rev. B*, 81:035117, Jan 2010.

[42] Y. Kamiya, N. Kawashima, and C. D. Batista. Dimensional crossover in the quasi-two-dimensional Ising-O(3) model. *Phys. Rev. B*, 84:214429, Dec 2011.

[43] A. H. Castro Neto, G. Castilla, and B. A. Jones. Non-Fermi liquid behavior and Griffiths phase in f-electron compounds. *Phys. Rev. Lett.*, 81:3531–3534, Oct 1998.

[44] Subir Sachdev, Chiranjeeb Buragohain, and Matthias Vojta. Quantum impurity in a nearly critical two-dimensional antiferromagnet. *Science*, 286(5449):2479–2482, Dec 1999.

[45] A. J. Millis, D. K. Morr, and J. Schmalian. Local defect in metallic quantum critical systems. *Phys. Rev. Lett.*, 87:167202, Oct 2001.

[46] H. Maebashi, K. Miyake, and C. M. Varma. Singular effects of impurities near the ferromagnetic quantum-critical point. *Phys. Rev. Lett.*, 88:226403, May 2002.

[47] Thomas Vojta. Disorder-induced rounding of certain quantum phase transitions. *Phys. Rev. Lett.*, 90:107202, Mar 2003.

[48] V. Dobrosavljević and E. Miranda. Absence of conventional quantum phase transitions in itinerant systems with disorder. *Phys. Rev. Lett.*, 94:187203, May 2005.

[49] Thomas Vojta and Jörg Schmalian. Percolation quantum phase transitions in diluted magnets. *Phys. Rev. Lett.*, 95(23):237206, Nov 2005.

[50] H. Alloul, J. Bobroff, M. Gabay, and P. J. Hirschfeld. Defects in correlated metals and superconductors. *Rev. Mod. Phys.*, 81:45–108, Jan 2009.

[51] Brian M. Andersen, Siegfried Graser, and P. J. Hirschfeld. Disorder-induced freezing of dynamical spin fluctuations in underdoped cuprate superconductors. *Phys. Rev. Lett.*, 105:147002, Sep 2010.

[52] E. C. Andrade, E. Miranda, and V. Dobrosavljević. Quantum ripples in strongly correlated metals. *Phys. Rev. Lett.*, 104:236401, Jun 2010.

[53] E. W. Carlson, K. A. Dahmen, E. Fradkin, and S. A. Kivelson. Hysteresis and noise from electronic nematicity in high-temperature superconductors. *Phys. Rev. Lett.*, 96:097003, Mar 2006.

[54] Kyungmin Lee, Steven A. Kivelson, and Eun-Ah Kim. Cold-spots and glassy nematicity in underdoped cuprates. *Phys. Rev. B*, 94:014204, Jul 2016.

[55] V Mishra and P J Hirschfeld. Effect of disorder on the competition between nematic and superconducting order in FeSe. *New Journal of Physics*, 18(10):103001, 2016.

[56] Hsueh-Hui Kuo, Jiun-Haw Chu, Johanna C. Palmstrom, Steven A. Kivelson, and Ian R. Fisher. Ubiquitous signatures of nematic quantum criticality in optimally doped Fe-based superconductors. *Science*, 352(6288):958–962, 2016.

[57] Laimei Nie, Gilles Tarjus, and Steven Allan Kivelson. Quenched disorder and vestigial nematicity in the pseudogap regime of the cuprates. *Proceedings of the National Academy of Sciences*, 111(22):7980–7985, 2014.

[58] Mareike Hoyer, Rafael M. Fernandes, Alex Levchenko, and Jörg Schmalian. Disorder-promoted C_4-symmetric magnetic order in iron-based superconductors. *Phys. Rev. B*, 93:144414, Apr 2016.

[59] Barry M McCoy and Tai Tsun Wu. Theory of a two-dimensional Ising model with random impurities. i. Thermodynamics. *Phys. Rev.*, 176(2):631–643, Dec 1968.

[60] Robert B. Griffiths. Nonanalytic behavior above the critical point in a random Ising ferromagnet. *Phys. Rev. Lett.*, 23(1):17–19, 1969.

[61] Rastko Sknepnek and Thomas Vojta. Smeared phase transition in a three-dimensional Ising model with planar defects: Monte Carlo simulations. *Phys. Rev. B*, 69:174410, May 2004.

[62] Thomas Vojta and Jörg Schmalian. Quantum Griffiths effects in itinerant Heisenberg magnets. *Phys. Rev. B*, 72(4):045438, Jul 2005.

[63] José A. Hoyos and Thomas Vojta. Percolation transition and dissipation in quantum Ising magnets. *Phys. Rev. B*, 74:140401, Oct 2006.

[64] José A. Hoyos and Thomas Vojta. Theory of smeared quantum phase transitions. *Phys. Rev. Lett.*, 100:240601, Jun 2008.

[65] Manal Al-Ali, José A. Hoyos, and Thomas Vojta. Percolation transition in quantum Ising and rotor models with sub-Ohmic dissipation. *Phys. Rev. B*, 86:075119, Aug 2012.

[66] Amnon Aharony and Dietrich Stauffer. *Introduction to percolation theory*. Taylor & Francis, 2003.

[67] Thomas Vojta. Quantum Griffiths effects and smeared phase transitions in metals: Theory and experiment. *Journal of Low Temperature Physics*, 161(1):299–323, Oct 2010.

[68] G. Lang, H.-J. Grafe, D. Paar, F. Hammerath, K. Manthey, G. Behr, J. Werner, and B. Büchner. Nanoscale electronic order in iron pnictides. *Phys. Rev. Lett.*, 104:097001, Mar 2010.

[69] A. P. Dioguardi, T. Kissikov, C. H. Lin, K. R. Shirer, M. M. Lawson, H.-J. Grafe, J.-H. Chu, I. R. Fisher, R. M. Fernandes, and N. J. Curro. NMR evidence for inhomogeneous nematic fluctuations in $BaFe_2(As_{1-x}P_x)_2$. *Phys. Rev. Lett.*, 116:107202, Mar 2016.

[70] D. S. Inosov, G. Friemel, J. T. Park, A. C. Walters, Y. Texier, Y. Laplace, J. Bobroff, V. Hinkov, D. L. Sun, Y. Liu, R. Khasanov, K. Sedlak, Ph. Bourges, Y. Sidis,

A. Ivanov, C. T. Lin, T. Keller, and B. Keimer. Possible realization of an antiferromagnetic Griffiths phase in $Ba(Fe_{1-x}Mn_x)_2As_2$. *Phys. Rev. B*, 87:224425, Jun 2013.

[71] Maria N. Gastiasoro and Brian M. Andersen. Enhancement of magnetic stripe order in iron-pnictide superconductors from the interaction between conduction electrons and magnetic impurities. *Phys. Rev. Lett.*, 113:067002, Aug 2014.

[72] J. Bardeen, L. N. Cooper, and J. R. Schrieffer. Theory of superconductivity. *Phys. Rev.*, 108:1175–1204, Dec 1957.

[73] Leon N. Cooper. Bound electron pairs in a degenerate Fermi gas. *Phys. Rev.*, 104:1189–1190, Nov 1956.

[74] N. N. Bogoljubov. On a new method in the theory of superconductivity. *Il Nuovo Cimento (1955-1965)*, 7(6):794–805, Mar 1958.

[75] P. W. Anderson. Random-phase approximation in the theory of superconductivity. *Phys. Rev.*, 112:1900–1916, Dec 1958.

[76] Lev P. Gor'kov. On the energy spectrum of superconductors. *JETP*, 34(3):505–508, Mar 1958.

[77] G. M. Eliashberg. Film superconductivity stimulated by a high-frequency field. *JETP Letters*, 11:114, 1970.

[78] B. I. Ivlev, S. G. Lisitsyn, and G. M. Eliashberg. Nonequilibrium excitations in superconductors in high-frequency fields. *J. Low Temp. Phys.*, 10(3):449–468, Feb 1973.

[79] T. Papenkort, V. M. Axt, and T. Kuhn. Coherent dynamics and pump-probe spectra of BCS superconductors. *Phys. Rev. B*, 76:224522, Dec 2007.

[80] Andreas P. Schnyder, Dirk Manske, and Adolfo Avella. Resonant generation of coherent phonons in a superconductor by ultrafast optical pump pulses. *Phys. Rev. B*, 84:214513, Dec 2011.

[81] Alireza Akbari, Andreas P. Schnyder, Dirk Manske, and Ilya Eremin. Theory of nonequilibrium dynamics of multiband superconductors. *EPL (Europhysics Letters)*, 101(1):17002, Jan 2013.

[82] Emil A. Yuzbashyan, Boris L. Altshuler, Vadim B. Kuznetsov, and Victor Z. Enolskii. Nonequilibrium Cooper pairing in the nonadiabatic regime. *Phys. Rev. B*, 72:220503, Dec 2005.

[83] Francesco Peronaci, Marco Schiró, and Massimo Capone. Transient dynamics of d-wave superconductors after a sudden excitation. *Phys. Rev. Lett.*, 115:257001, Dec 2015.

[84] F Hunte, J Jaroszynski, A Gurevich, D C Larbalestier, R Jin, A S Sefat, M A McGuire, B C Sales, D K Christen, and D Mandrus. Two-band superconductivity in $LaFeAsO_0.89F_0.11$ at very high magnetic fields. *Nature*, 453:903, may 2008.

[85] Shuji NishiZaki, Yoshiteru Maeno, and Zhiqiang Mao. Changes in the superconducting state of Sr_2RuO_4 under magnetic fields probed by specific heat. *Journal of the Physical Society of Japan*, 69(2):572–578, 2000.

[86] I. A. Firmo, S. Lederer, C. Lupien, A. P. Mackenzie, J. C. Davis, and S. A. Kivelson. Evidence from tunneling spectroscopy for a quasi-one-dimensional origin of superconductivity in Sr_2RuO_4. *Phys. Rev. B*, 88:134521, Oct 2013.

[87] M. Jourdan, A. Zakharov, M. Foerster, and H. Adrian. Evidence for multiband superconductivity in the heavy fermion compound UNi_2Al_3. *Phys. Rev. Lett.*, 93:097001, Aug 2004.

[88] G. Seyfarth, J. P. Brison, M.-A. Méasson, J. Flouquet, K. Izawa, Y. Matsuda, H. Sugawara, and H. Sato. Multiband superconductivity in the heavy fermion compound $PrOs_4Sb_{12}$. *Phys. Rev. Lett.*, 95:107004, Sep 2005.

[89] Hidekazu Mukuda, Sachihiro Nishide, Atsushi Harada, Kaori Iwasaki, Mamoru Yogi, Mitsuharu Yashima, Yoshio Kitaoka, Masahiko Tsujino, Tetsuya Takeuchi, Rikio Settai, Yoshichika nuki, Ernst Bauer, Kohei M. Itoh, and Eugene E. Haller.

Multiband superconductivity in heavy fermion compound $CePt_3Si$ without inversion symmetry: An NMR study on a high-quality single crystal. *Journal of the Physical Society of Japan*, 78(1):014705, 2009.

[90] A. V. Chubukov, D. V. Efremov, and I. Eremin. Magnetism, superconductivity, and pairing symmetry in iron-based superconductors. *Phys. Rev. B*, 78:134512, Oct 2008.

[91] H Krull, N Bittner, G S Uhrig, D Manske, and A P Schnyder. Coupling of Higgs and Leggett modes in non-equilibrium superconductors. *Nat. Commun.*, 7:11921, Jun 2016.

[92] Ryusuke Matsunaga and Ryo Shimano. Nonequilibrium BCS state dynamics induced by intense terahertz pulses in a superconducting NbN film. *Phys. Rev. Lett.*, 109:187002, Oct 2012.

[93] Ryusuke Matsunaga, Yuki I. Hamada, Kazumasa Makise, Yoshinori Uzawa, Hirotaka Terai, Zhen Wang, and Ryo Shimano. Higgs amplitude mode in the BCS superconductors $Nb_{1-x}Ti_xN$ induced by terahertz pulse excitation. *Phys. Rev. Lett.*, 111:057002, Jul 2013.

[94] R. Matsunaga, N. Tsuji, H. Fujita, A. Sugioka, K. Makise, Y. Uzawa, H. Terai, Z. Wang, H. Aoki, and R. Shimano. Light-induced collective pseudospin precession resonating with Higgs mode in a superconductor. *Science*, 345(6201):1145, 2014.

[95] Ryusuke Matsunaga, Naoto Tsuji, Kazumasa Makise, Hirotaka Terai, Hideo Aoki, and Ryo Shimano. Polarization-resolved terahertz third-harmonic generation in a single-crystal superconductor NbN: Dominance of the Higgs mode beyond the BCS approximation. *Phys. Rev. B*, 96:020505, Jul 2017.

[96] M Zachmann, M D Croitoru, A Vagov, V M Axt, T Papenkort, and T Kuhn. Ultrafast terahertz-field-induced dynamics of superconducting bulk and quasi-1d samples. *New J. Phys.*, 15(5):055016, May 2013.

[97] R.W. Richardson and N. Sherman. Exact eigenstates of the pairing-force Hamiltonian. *Nucl. Phys.*, 52:221–238, Mar 1964.

[98] J. Dukelsky, S. Pittel, and G. Sierra. Colloquium: Exactly solvable Richardson-Gaudin models for many-body quantum systems. *Rev. Mod. Phys.*, 76:643–662, Aug 2004.

[99] E. A. Yuzbashyan, M. Dzero, V. Gurarie, and M. S. Foster. Quantum quench phase diagrams of an s-wave BCS-BEC condensate. *Phys. Rev. A*, 91:033628, Mar 2015.

[100] Emil A. Yuzbashyan and Maxim Dzero. Dynamical vanishing of the order parameter in a fermionic condensate. *Phys. Rev. Lett.*, 96:230404, Jun 2006.

[101] J. A. Pals, K. Weiss, P. M. T. M. van Attekum, R. E. Horstman, and J. Wolter. Non-equilibrium superconductivity in homogeneous thin films. *Phys. Rep.*, 89:323, 1982.

[102] Tobias Kampfrath, Koichiro Tanaka, and Keith A. Nelson. Resonant and nonresonant control over matter and light by intense terahertz transients. *Nat. Photon.*, 7(9):680–690, Sep 2013.

[103] M. Beck, M. Klammer, S. Lang, P. Leiderer, V. V. Kabanov, G. N. Gol'tsman, and J. Demsar. Energy-gap dynamics of superconducting NbN thin films studied by time-resolved terahertz spectroscopy. *Phys. Rev. Lett.*, 107:177007, Oct 2011.

[104] M. Beck, I. Rousseau, M. Klammer, P. Leiderer, M. Mittendorff, S. Winnerl, M. Helm, G. N. Gol'tsman, and J. Demsar. Transient increase of the energy gap of superconducting NbN thin films excited by resonant narrow-band terahertz pulses. *Phys. Rev. Lett.*, 110:267003, Jun 2013.

[105] X. Yang, C. Vaswani, C. Sundahl, M. Mootz, P. Gagel, L. Luo, J. H. Kang, P. P. Orth, I. E. Perakis, C. B. Eom, and J. Wang. Terahertz-light quantum tuning of a metastable emergent phase hidden by superconductivity. *Nat. Mater.*, 17(7):586–591, Jun 2018.

[106] X. Yang, X. Zhao, C. Vaswani, C. Sundahl, B. Song, Y. Yao, D. Cheng, Z. Liu, P. P. Orth, M. Mootz, J. H. Kang, I. E. Perakis, C.-Z. Wang, K.-M. Ho, C. B. Eom, and J. Wang. Ultrafast nonthermal terahertz electrodynamics and possible

quantum energy transfer in the Nb_3Sn superconductor. *Phys. Rev. B*, 99:094504, Mar 2019.

[107] Flavio Giorgianni, Tommaso Cea, Carlo Vicario, Christoph P Hauri, Wenura K Withanage, Xiaoxing Xi, and Lara Benfatto. Leggett mode controlled by light pulses. *Nat. Phys.*, 15(4):341–346, 2019.

[108] M. Šindler, C. Kadlec, P. Kužel, K. Ilin, M. Siegel, and H. Němec. Departure from BCS response in photoexcited superconducting NbN films observed by terahertz spectroscopy. *Phys. Rev. B*, 97:054507, Feb 2018.

[109] R. Mankowsky, A. Subedi, M. Forst, S. O. Mariager, M. Chollet, H. T. Lemke, J. S. Robinson, J. M. Glownia, M. P. Minitti, A. Frano, M. Fechner, N. A. Spaldin, T. Loew, B. Keimer, A. Georges, and A. Cavalleri. Nonlinear lattice dynamics as a basis for enhanced superconductivity in $YBa_2Cu_3O_{6.5}$. *Nature*, 516(7529):71–73, Dec 2014.

[110] W. Hu, S. Kaiser, D. Nicoletti, C. R. Hunt, I. Gierz, M. C. Hoffmann, M. Le Tacon, T. Loew, B. Keimer, and A. Cavalleri. Optically enhanced coherent transport in $YBa_2Cu_3O_{6.5}$ by ultrafast redistribution of interlayer coupling. *Nat. Mater.*, 13(7):705–711, July 2014.

[111] M. Mitrano, A. Cantaluppi, D. Nicoletti, S. Kaiser, A. Perucchi, S. Lupi, P. Di Pietro, D. Pontiroli, M. Ricc, S. R. Clark, D. Jaksch, and A. Cavalleri. Possible light-induced superconductivity in K_3C_{60} at high temperature. *Nature*, 530(7591):461–464, Feb 2016.

[112] T Papenkort, T Kuhn, and V M Axt. Nonequilibrium dynamics and coherent control of BCS superconductors driven by ultrashort THz pulses. *J. Phys.*, 193:012050, Nov 2009.

[113] Maxim Dzero, Maxim Khodas, and Alex Levchenko. Amplitude modes and dynamic coexistence of competing orders in multicomponent superconductors. *Phys. Rev. B*, 91:214505, Jun 2015.

[114] Yuta Murakami, Philipp Werner, Naoto Tsuji, and Hideo Aoki. Multiple amplitude modes in strongly coupled phonon-mediated superconductors. *Phys. Rev. B*, 93:094509, Mar 2016.

[115] V. Gurarie. Nonequilibrium dynamics of weakly and strongly paired superconductors. *Phys. Rev. Lett.*, 103:075301, Aug 2009.

[116] Kota Katsumi, Naoto Tsuji, Yuki I. Hamada, Ryusuke Matsunaga, John Schneeloch, Ruidan D. Zhong, Genda D. Gu, Hideo Aoki, Yann Gallais, and Ryo Shimano. Higgs mode in the d-wave superconductor $Bi_2Sr_2CaCu_2O_{8+x}$ driven by an intense terahertz pulse. *Phys. Rev. Lett.*, 120:117001, Mar 2018.

[117] M. H. S. Amin, E. V. Bezuglyi, A. S. Kijko, and A. N. Omelyanchouk. Wigner distribution function formalism for superconductors and collisionless dynamics of the superconducting order parameter. *Low Temp. Phys.*, 30(7):661–666, 2004.

[118] R. A. Barankov, L. S. Levitov, and B. Z. Spivak. Collective Rabi oscillations and solitons in a time-dependent BCS pairing problem. *Phys. Rev. Lett.*, 93:160401, Oct 2004.

[119] G. L. Warner and A. J. Leggett. Quench dynamics of a superfluid Fermi gas. *Phys. Rev. B*, 71:134514, Apr 2005.

[120] A. V. Andreev, V. Gurarie, and L. Radzihovsky. Nonequilibrium dynamics and thermodynamics of a degenerate Fermi gas across a Feshbach resonance. *Phys. Rev. Lett.*, 93:130402, Sep 2004.

[121] A. F. Kemper, M. A. Sentef, B. Moritz, J. K. Freericks, and T. P. Devereaux. Direct observation of Higgs mode oscillations in the pump-probe photoemission spectra of electron-phonon mediated superconductors. *Phys. Rev. B*, 92:224517, Dec 2015.

[122] H. Krull, D. Manske, G. S. Uhrig, and A. P. Schnyder. Signatures of nonadiabatic BCS state dynamics in pump-probe conductivity. *Phys. Rev. B*, 90:014515, Jul 2014.

[123] B. Fauseweh, L. Schwarz, N. Tsuji, N. Cheng, N. Bittner, H. Krull, M. Berciu, G. S. Uhrig, A. P. Schnyder, S. Kaiser, and D. Manske. Higgs spectroscopy of superconductors in nonequilibrium. *arXiv e-prints*, page arXiv:1712.07989, Dec 2017.

[124] Marvin A. Müller, Pengtao Shen, Maxim Dzero, and Ilya Eremin. Short-time dynamics in $s + is$-wave superconductor with incipient bands. *Phys. Rev. B*, 98:024522, Jul 2018.

[125] Jasen A. Scaramazza, Pietro Smacchia, and Emil A. Yuzbashyan. Consequences of integrability breaking in quench dynamics of pairing Hamiltonians. *Phys. Rev. B*, 99:054520, Feb 2019.

[126] Yang-Zhi Chou, Yunxiang Liao, and Matthew S. Foster. Twisting Anderson pseudospins with light: Quench dynamics in terahertz-pumped BCS superconductors. *Phys. Rev. B*, 95:104507, Mar 2017.

[127] Bing Cheng, Liang Wu, N. J. Laurita, Harkirat Singh, Madhavi Chand, Pratap Raychaudhuri, and N. P. Armitage. Anomalous gap-edge dissipation in disordered superconductors on the brink of localization. *Phys. Rev. B*, 93:180511(R), May 2016.

[128] Caihong Zhang, Biaobing Jin, Jiaguang Han, Iwao Kawayama, Hironaru Murakami, Xiaoqing Jia, Lanju Liang, Lin Kang, Jian Chen, Peiheng Wu, and Masayoshi Tonouchi. Nonlinear response of superconducting NbN thin film and NbN metamaterial induced by intense terahertz pulses. *New Journal of Physics*, 15(5):055017, May 2013.

[129] U. S. Pracht, E. Heintze, C. Clauss, D. Hafner, R. Bek, D. Werner, S. Gelhorn, M. Scheffler, M. Dressel, D. Sherman, B. Gorshunov, K. S. Il'in, D. Henrich, and M. Siegel. Electrodynamics of the superconducting state in ultra-thin films at THz frequencies. *IEEE Transactions on Terahertz Science and Technology*, 3(3):269, May 2013.

[130] Nikolai A. Sinitsyn, Emil A. Yuzbashyan, Vladimir Y. Chernyak, Aniket Patra,

and Chen Sun. Integrable time-dependent quantum Hamiltonians. *Phys. Rev. Lett.*, 120:190402, May 2018.

[131] T. Cea, C. Castellani, G. Seibold, and L. Benfatto. Nonrelativistic dynamics of the amplitude (Higgs) mode in superconductors. *Phys. Rev. Lett.*, 115:157002, Oct 2015.

[132] Naoto Tsuji and Hideo Aoki. Theory of Anderson pseudospin resonance with Higgs mode in superconductors. *Phys. Rev. B*, 92:064508, Aug 2015.

Appendix A

Technical Details for Chapter 2

A.1 Derivation of the saddle-point equations for a droplet

We start by rewriting the effective large-N rescaled action for a droplet with linear size L, as given in the main text:

$$S_{\text{eff}}\left[\psi,\phi\right]=\frac{1}{L^2}\sum_{\mathbf{q}}\int\frac{d\omega}{2\pi}\left\{\frac{\phi^2}{2g}-\frac{\psi^2}{2u}+\frac{1}{2}\ln\left[\left(\chi_{\mathbf{q},\omega}^{-1}+\psi\right)^2-\phi^2\right]\right\} \tag{A.1}$$

where ϕ is the Ising-nematic order parameter and ψ is the DW fluctuation field. Here, $\chi_{\mathbf{q},\omega}=\left(r_0+\mathbf{q}^2+\gamma\left|\omega\right|\right)^{-1}$ is the bare DW susceptibility with Landau damping γ and $\mathbf{q}=\frac{2\pi}{L}\mathbf{n}$ is the discretized momentum with $\mathbf{n}=(n_x,\,n_y)$ and $n_x,\,n_y\in\mathbb{Z}$. The saddle-point of the effective action is given by setting $\frac{\delta S_{\text{eff}}}{\delta\psi}=\frac{\delta S_{\text{eff}}}{\delta\phi}=0$, which corresponds to the following coupled equations,

$$\frac{r-r_0}{u} \;=\; \frac{1}{2L^2}\sum_{\mathbf{q}}\int\frac{d\omega}{2\pi}\left(\frac{1}{r+q^2+\gamma\left|\omega\right|-\phi}+\frac{1}{r+q^2+\gamma\left|\omega\right|+\phi}\right) \tag{A.2}$$

$$\frac{\phi}{g} \;=\; \frac{1}{2L^2}\sum_{\mathbf{q}}\int\frac{d\omega}{2\pi}\left(\frac{1}{r+q^2+\gamma\left|\omega\right|-\phi}-\frac{1}{r+q^2+\gamma\left|\omega\right|+\phi}\right) \tag{A.3}$$

where $r\equiv r_0+\psi$. To tackle the discrete momentum summation, we apply the Poisson summation formula [62]:

$$\frac{1}{L^d}\sum_{\mathbf{q}} f(\mathbf{q}) = \int \frac{d^d q}{(2\pi)^d} f(\mathbf{q}) + \sum_{\mathbf{n}\neq\mathbf{0}} \int \frac{d^d q}{(2\pi)^d} f(\mathbf{q})\, e^{i\mathbf{q}\cdot\mathbf{n}L} \tag{A.4}$$

The integrals appearing in the equations above can be evaluated analytically:

$$\int \frac{d^2 q d\omega}{(2\pi)^3} \frac{1}{A + q^2 + \gamma|\omega|} = \int \frac{d^2 q d\omega}{(2\pi)^3} \frac{1}{q^2 + \gamma|\omega|} - \frac{A}{4\pi^2\gamma}\left[\ln\left(\frac{\Lambda^2}{A}\right) + 1\right]$$

and:

$$\int \frac{d^2 q d\omega}{(2\pi)^3} \frac{e^{i\mathbf{q}\cdot\mathbf{n}L}}{A + q^2 + \gamma|\omega|} = \frac{2\sqrt{A}}{L|\mathbf{n}|} K_1\left(\sqrt{A}L|\mathbf{n}|\right) \tag{A.5}$$

where we used the fact that the momentum cutoff is such that $\Lambda^2 \gg r \pm \phi$. We verified that this condition is met for the parameters u and g used in the main text. Defining $\tilde{r}_0 = r_0 + u\int \frac{d^2 q d\omega}{(2\pi)^3} \frac{1}{q^2+\gamma|\omega|}$, $\tilde{u} = u/\left(4\pi^2\gamma\right)$, and $\tilde{g} = g/\left(4\pi^2\gamma\right)$, we arrive at the equations displayed in the main text:

$$\begin{aligned} r &= \tilde{r}_0 - \tilde{u} r \left(\ln\frac{\Lambda^2}{\sqrt{r^2-\phi^2}} + 1 - \frac{\phi}{r}\tanh^{-1}\frac{\phi}{r}\right) \\ &\quad + \frac{2\pi\tilde{u}}{L^2}\left(\mathcal{F}\left[(r-\phi)L^2\right] + \mathcal{F}\left[(r+\phi)L^2\right]\right) \end{aligned} \tag{A.6}$$

$$\begin{aligned} \phi &= \phi\tilde{g}\left(\ln\frac{\Lambda^2}{\sqrt{r^2-\phi^2}} + 1 - \frac{r}{\phi}\tanh^{-1}\frac{\phi}{r}\right) \\ &\quad + \frac{2\pi\tilde{g}}{L^2}\left(\mathcal{F}\left[(r-\phi)L^2\right] - \mathcal{F}\left[(r+\phi)L^2\right]\right) \end{aligned} \tag{A.7}$$

where we defined the function:

$$\mathcal{F}(y) \equiv \frac{1}{\pi}\sum_{\mathbf{n}\neq\mathbf{0}} \frac{\sqrt{y}}{|\mathbf{n}|} K_1\left(|\mathbf{n}|\sqrt{y}\right) \tag{A.8}$$

Note that, for $\phi = 0$, we recover the self-consistent equations of Ref. [62] for an itinerant antiferromagnet. Using the fact that:

$$\frac{\sqrt{y}}{|\mathbf{n}|} K_1\left(|\mathbf{n}|\sqrt{y}\right) = \frac{1}{4}\int_0^\infty du\, u^{-2} e^{-yu - \frac{|\mathbf{n}|^2}{4u}} \tag{A.9}$$

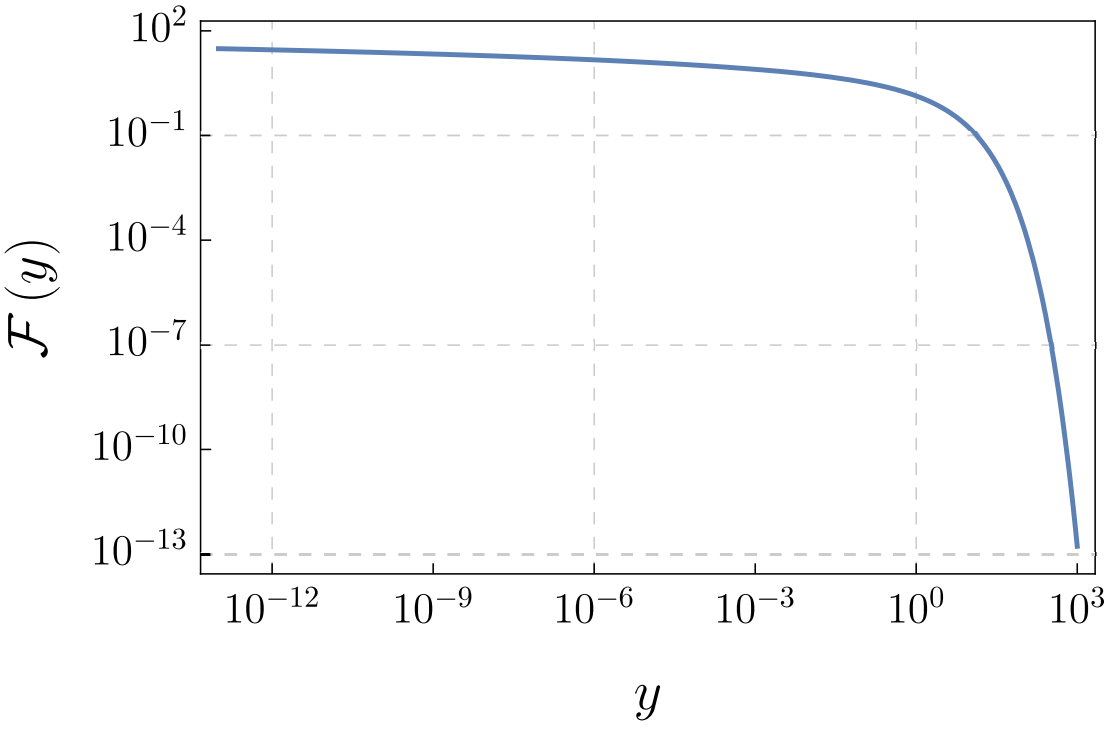

Figure A.1: Function $\mathcal{F}(y)$ defined in Eq. (A.8).

we can evaluate the sum and express the function as an integral:

$$\mathcal{F}(y) = \frac{1}{4\pi}\int_0^\infty du\, u^{-2} e^{-yu}\left[\theta_3^2\left(0, e^{-\frac{1}{4u}}\right) - 1\right] \tag{A.10}$$

where $\theta_3(a,b)$ is the elliptic theta function. The asymptotic behavior of $\mathcal{F}(y)$ follows from Eqs. (A.8) and (A.10). For $y \gg 1$, the sum in Eq. (A.8) is dominated by the $|\mathbf{n}| = 1$ contribution, and we obtain:

$$\mathcal{F}(y \gg 1) \simeq \frac{2y^{1/4}\,\mathrm{e}^{-\sqrt{y}}}{\sqrt{2\pi}} \tag{A.11}$$

For $y \ll 1$, it is more convenient to use the integral representation (A.10). Following the same steps as Ref. [62], it follows that the function has a logarithmic divergence:

$$\mathcal{F}(y \ll 1) \simeq -\ln\left(\frac{y\,\mathrm{e}^{\gamma+1}}{4\pi}\right) \tag{A.12}$$

where γ is the Euler number. Equations (A.6) and (A.7) are solved numerically to yield $\phi(r_0, L)$. In the numerical calculation, we use an interpolation function for $\mathcal{F}(y)$ that interpolates between Eq. (A.8) with 80×80 terms in the sum and the asymptotic behavior in Eq. (A.12). The resulting function is shown in Fig. A.1. We checked that the error with respect to the exact function $\mathcal{F}$ is no more than 2%.

Before proceeding, we rederive the solutions of the self-consistent equations in the clean limit (i.e. $L \to \infty$, which makes $\mathcal{F}(y) \to 0$). In this case, the solution of Eqs. (A.6) and (A.7) shows that r_0 is maximum for $\phi = r$. However, $\phi = r$ implies a DW transition, since the renormalized DW susceptibility is $(r - \phi)^{-1}$. Thus, one has to go back to the action (A.1) and consider the possibility of a finite DW order parameter Δ. In the large-N limit, this corresponds to adding the term $\Delta^2 (r - \phi)$ in the action (see for instance [14]). Minimizing with respect to Δ, it is clear that only when $\phi = r$ is that we obtain $\Delta \neq 0$. In this case, the self-consistent equations become:

$$\phi = r_0 - \phi u \left(\ln \frac{\Lambda^2}{2\phi} + 1 \right) + u\Delta^2 \tag{A.13}$$

$$\phi = \phi g \left(\ln \frac{\Lambda^2}{2\phi} + 1 \right) + g\Delta^2 \tag{A.14}$$

where unimportant constants have been absorbed in Δ. We can now eliminate Δ to find r_0 as function of ϕ:

$$\frac{r_0}{u} = \phi \left(\frac{1}{u} - \frac{1}{g} \right) + 2\phi \left(\ln \frac{\Lambda^2}{2\phi} + 1 \right) \tag{A.15}$$

The first-order transition therefore takes place at:

$$\frac{r^*_{0,\text{clean}}}{\Lambda^2} = u \exp\left(\frac{1}{2u} - \frac{1}{2g} \right) \tag{A.16}$$

and the jump in ϕ is given by:

$$\phi^*_{\text{clean}} = \frac{r^*_{0,\text{clean}}}{2u} \tag{A.17}$$

For the parameters used in the main text, $u = 0.9$ and $g = 0.25u$, we find $\frac{r^*_{0,\text{clean}}}{\Lambda^2} \approx 0.17$ and $\frac{\phi^*_{\text{clean}}}{\Lambda^2} \approx 0.09$. Note that, inside the finite size droplets, $r > \phi$ always. Therefore,

we do not need to add the DW field Δ in the self-consistent equations.

A.2 Properties of the Ising-nematic order as function of the size of the droplets

Here we discuss how two properties of the Ising-nematic order depend on the size L of the droplet: the character of the transition and the value of the tuning parameter r_0 for which the quantum transition takes place. We consider here the two self-consistent equations (A.6) and (A.7) with reduced variables $(r_0,\, r,\, \phi) \to (r_0,\, r,\, \phi)\,/\Lambda^2$. Furthermore, the size L of the droplet is measured in units of $1/\Lambda \approx a$, where a is the lattice constant. For convenience, we drop the tilde notation of Eqs. (A.6) and (A.7) in this section.

The condition for a droplet of size L to undergo a continuous Ising-nematic quantum phase transition is that

$$\left.\frac{dr_0}{d\phi}\right|_{\phi\to 0} \leq 0 \tag{A.18}$$

where r_0 is the tuning parameter. Taking derivatives with respect to ϕ for the self-consistent equations (A.6) and (A.7), we find:

$$\begin{aligned}\frac{1}{u}\frac{dr_0}{d\phi} \;=\; & \left(\frac{1}{u} + \ln\frac{1}{\sqrt{r^2-\phi^2}}\right)\frac{dr}{d\phi} - u\,\tanh^{-1}\frac{\phi}{r} \\ & -2\pi\left\{\mathcal{F}'\left[(r+\phi)\,L^2\right]\left(1+\frac{dr}{d\phi}\right) - \mathcal{F}'\left[(r-\phi)\,L^2\right]\left(1-\frac{dr}{d\phi}\right)\right\}\end{aligned} \tag{A.19}$$

$$\frac{dr}{d\phi} = \frac{-\frac{1}{g} + \ln\frac{1}{\sqrt{r^2-\phi^2}} - 2\pi\left(\mathcal{F}'\left[(r+\phi)\,L^2\right] + \mathcal{F}'\left[(r-\phi)\,L^2\right]\right)}{\tanh^{-1}\left(\frac{\phi}{r}\right) + 2\pi\left(\mathcal{F}'\left[(r+\phi)\,L^2\right] - \mathcal{F}'\left[(r-\phi)\,L^2\right]\right)} \tag{A.20}$$

We can eliminate the logarithms by noting that the second self-consistent equation gives:

$$\frac{1}{g} = \ln\frac{1}{\sqrt{r^2-\phi^2}} + 1 - \frac{r}{\phi}\tanh^{-1}\left(\frac{\phi}{r}\right) - \frac{2\pi}{\phi L^2}\left(\mathcal{F}\left[(r+\phi)\,L^2\right] - \mathcal{F}\left[(r-\phi)\,L^2\right]\right) \tag{A.21}$$

Substituting Eq. (A.21) in Eqs. (A.19)-(A.20), and then expanding for small ϕ, we find:

$$\left.\frac{dr_0}{d\phi}\right|_{\phi\to 0} = \frac{u}{\lambda}\frac{\phi}{3r^{(0)}}\frac{1-4\pi\zeta^2\mathcal{F}'''(\zeta)-3\lambda\left[1+4\pi\zeta\mathcal{F}''(\zeta)\right]^2}{1+4\pi\zeta\mathcal{F}''(\zeta)} \tag{A.22}$$

where we defined, for convenience, $\zeta = r^{(0)}L^2$ and $\frac{1}{\lambda} = \frac{1}{u}+\frac{1}{g}$. From (A.22), the condition for a droplet to undergo a continuous Ising-nematic quantum phase transition is:

$$(1-3\lambda) - 4\pi\zeta^2\mathcal{F}'''(\zeta) - 24\pi\lambda\zeta\mathcal{F}''(\zeta) - 48\pi^2\lambda\zeta^2\left[\mathcal{F}''(\zeta)\right]^2 \leq 0 \tag{A.23}$$

Note that, here, $r^{(0)}$ is a shorthand notation for $r^{(0)} \equiv r(\phi = 0)$. Thus, its value, as well as the corresponding r_0, are determined by taking the limit $\phi = 0$ in the self-consistent equations (A.6) and (A.7):

$$r_0 = ur^{(0)}\left[\frac{1}{u} + 1 - \ln r^{(0)} - \frac{4\pi}{\zeta}\mathcal{F}(\zeta)\right] \tag{A.24}$$

$$\frac{1}{g} = -\ln r^{(0)} - 4\pi\,\mathcal{F}'(\zeta) \tag{A.25}$$

Therefore, for given g and u, we can find the critical size of the droplet L_{c1} beyond which it undergoes a first-order transition by solving Eqs. (A.23) and (A.25) simultaneously:

$$L_{c1}^2 = \zeta_{c1}\exp\left[\frac{1}{g} + 4\pi\mathcal{F}'(\zeta_{c1})\right] \tag{A.26}$$

where ζ_{c1} is the value for which Eq. (A.23) satisfies the identity. For the parameters used in the main text, $u = 0.9$ and $g/u = 0.25$, we find $L_{c1}^2 \approx 58$.

Next, we analyze which of the droplets undergoing a second-order phase transition orders at the highest value of the tuning parameter r_0, i.e. we look for the critical droplet area L_{c2}^2 for which: $\frac{dr_0}{dL^2} = 0$.

Taking the derivative with respect to L^2 on Eqs. (A.24) and (A.25), we find:

$$\frac{1}{u}\frac{dr_0}{dL^2} = \frac{dr^{(0)}}{dL^2}\left[\frac{1}{\lambda} + 4\pi\mathcal{F}'\left(r^{(0)}L^2\right)\right] + \frac{4\pi}{L^4}\mathcal{F}\left(r^{(0)}L^2\right) - \frac{4\pi}{L^2}\mathcal{F}'\left(r^{(0)}L^2\right)\left(r^{(0)} + L^2\frac{dr^{(0)}}{dL^2}\right) \tag{A.27}$$

$$0 = -\frac{1}{r^{(0)}}\frac{dr^{(0)}}{dL^2} - 4\pi\mathcal{F}''\left(r^{(0)}L^2\right)\left(r^{(0)} + L^2\frac{dr^{(0)}}{dL^2}\right) \tag{A.28}$$

Solving for $\frac{dr_0}{dL^2}$, we obtain

$$\begin{aligned}\frac{dr_0}{dL^2} =& \frac{u}{\lambda}\frac{4\pi\exp\left(-\frac{2}{g} - 8\pi\mathcal{F}'(\zeta)\right)}{\zeta + 4\pi\zeta^2\mathcal{F}''(\zeta)} \\ &\times\left\{\lambda\left[\mathcal{F}(\zeta) - \zeta\mathcal{F}'(\zeta)\right]\left[\frac{1}{\zeta} + 4\pi\mathcal{F}''(\zeta)\right] - \zeta\mathcal{F}''(\zeta)\right\}\end{aligned} \tag{A.29}$$

Therefore, the first droplet that undergoes a continuous Ising-nematic quantum phase transition satisfies

$$\left[\mathcal{F}(\zeta_{c2}) - \zeta_{c2}\mathcal{F}'(\zeta_{c2})\right]\left[\frac{1}{\zeta_{c2}} + 4\pi\mathcal{F}''(\zeta_{c2})\right] = \frac{1}{\lambda}\zeta_{c2}\mathcal{F}''(\zeta_{c2}) \tag{A.30}$$

and its area is given by:

$$L_{c2}^2 = \zeta_{c2}\exp\left[\frac{1}{g} + 4\pi\mathcal{F}'(\zeta_{c2})\right] \tag{A.31}$$

Using Eqs. (A.24) and (A.25), we can find the corresponding value of the control parameter $r_0^*(L_{c2})$ at which this happens:

$$r_0^*(L_{c2}) = u\exp\left(-\frac{1}{g} - 4\pi\mathcal{F}'(\zeta_{c2})\right)\left[\frac{1}{\lambda} + 1 + 4\pi\mathcal{F}'(\zeta_{c2}) - \frac{4\pi}{\zeta_{c2}}\mathcal{F}(\zeta_{c2})\right] \tag{A.32}$$

It is instructive to compare it with the value $r_{0,\text{clean}}^*$ for which the first-order transition of the clean system takes place, see Eq. (A.16):

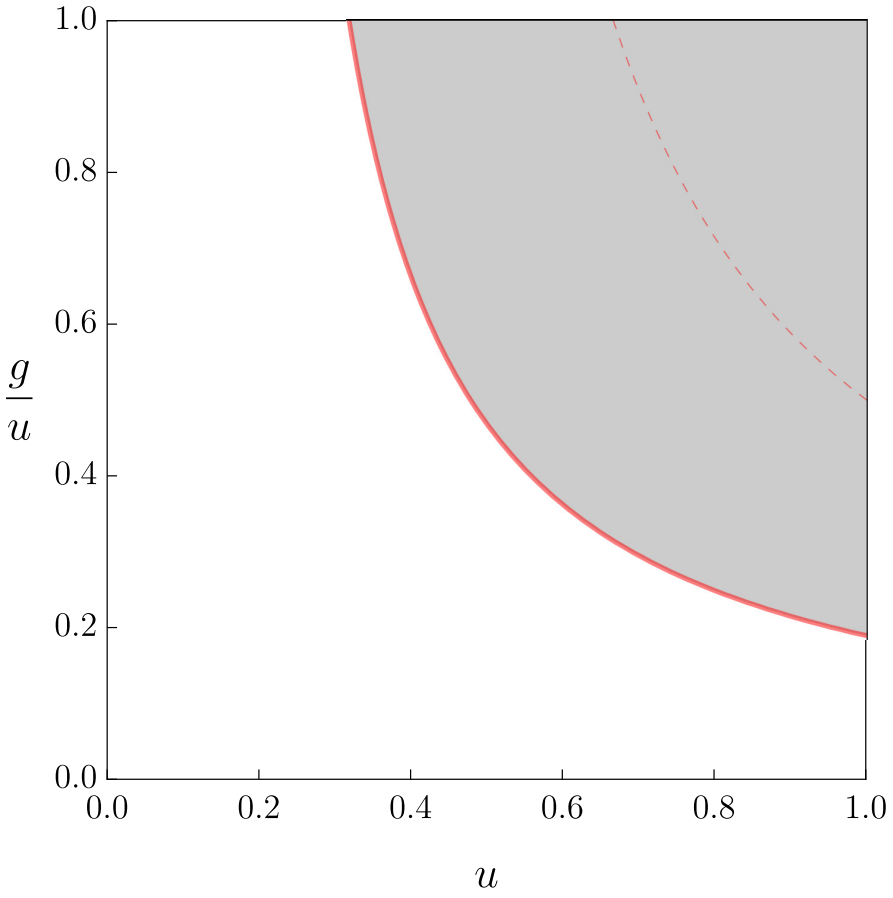

Figure A.2: Region in the (u, g) parameter space in which the droplet that orders first does so before the transition of the clean system, i.e, $r_0^*(L_{c2}) > r_{0,\text{clean}}^*$.

$$\frac{r_0^*(L_{c2})}{r_{0,\text{clean}}^*} = \exp\left(-\frac{1}{2\lambda} - 4\pi\mathcal{F}'(\zeta_{c2})\right)\left[\frac{1}{\lambda} + 1 + 4\pi\mathcal{F}'(\zeta_{c2}) - \frac{4\pi}{\zeta_{c2}}\mathcal{F}(\zeta_{c2})\right] \tag{A.33}$$

For the parameters used in the main text, $u = 0.9$ and $g = 0.25u$, we find $L_{c2}^2 \approx 40$ and $\frac{r_0^*(L_{c2})}{r_{0,\text{clean}}^*} \approx 1.08$. More generally, as a function of the two parameters u and g, there is a wide region in parameter space in which $\frac{r_0^*(L_{c2})}{r_{0,\text{clean}}^*} > 1$, shown as the shaded area in Fig. A.2.

A.3 Derivation of the probability distribution for the droplets sizes

In this section, we use results from percolation theory to derive the approximate probability distribution function $P(V)$ of finding a finite droplet with "volume" $V = L^2$ that is devoid of impurities. We consider that a local site-impurity completely suppresses both DW and nematic orders. The concentration of impurities is $1 - p$, i.e. the concentration of clean sites is p. From percolation theory, the number of finite-size "clean" clusters (droplets) containing s sites, denoted n_s, satisfies the scaling relation [66]:

$$n_s = \mathcal{N}_0 s^{-\tau} f\left(s/s_0\right) \tag{A.34}$$

where s_0, the typical cluster size, diverges at the percolation threshold p_c, τ is a critical exponent, and $\mathcal{N}_0$ is a normalization constant. The precise form of the scaling function $f(x)$ can only be obtained numerically. However, an often used approximation is an exponential decay:

$$n_s = \mathcal{N}_0 s^{-\tau} \exp\left(-s/s_0\right) \tag{A.35}$$

Now, the total number of clusters of size s is given by Nn_s, where N is the total number of sites. This implies that the total number of sites that belong to a cluster of size s is Nsn_s. Therefore, the probability $P(s)$ that a given site belong to a cluster of size s is:

$$P(s) \equiv \frac{Nsn_s}{N} = \mathcal{N}_0 s^{1-\tau} \exp\left(-s/s_0\right) \tag{A.36}$$

The constant $\mathcal{N}_0$ is given by the normalization condition on n_s:

$$\sum_s sn_s = p - P\left(p\right) \tag{A.37}$$

where $P(p)$ is the number of sites belonging to the infinite cluster (divided by the total number of sites). Thus, we obtain:

$$\mathcal{N}_0 = \frac{p - P\left(p\right)}{\sum\limits_s s^{1-\tau} \mathrm{e}^{-s/s_0}} \tag{A.38}$$

Importantly, $p - P(p)$ vanishes for both $p = 0$ and $p = 1$, and has a maximum near the percolation threshold p_c. If we are not too far from the percolation threshold, we can then approximate $p - P(p)$ by p_c, as the quantity that changes more strongly upon approaching the percolation threshold is s_0, which diverges at p_c. We then obtain:

$$P(s) \approx \frac{p_c \, s^{1-\tau} \mathrm{e}^{-s/s_0}}{\sum\limits_s s^{1-\tau} \mathrm{e}^{-s/s_0}} \tag{A.39}$$

The fact that $P(s)$ is not necessarily normalized to 1 is due to the fact that not all sites belong to a finite cluster.

The relationship between s and the linear size L of the cluster that enters the self-consistent equations (A.6) and (A.7) is $s = L^2/a^2$, where a is the lattice constant. In our problem, as explained above, L is given in units of the inverse momentum cutoff, $L = \tilde{L}/\Lambda$. Thus, we arrive at $\tilde{L}^2 = s\left(\Lambda a\right)^2$, with integer s. For concreteness, in our calculations we set $\Lambda = 1/a$.

Appendix B

Technical Details for Chapter 4

B.1 Initial conditions for the interaction quench

The system is at equilibrium before the interaction quench. For systems with only inter-band repulsion, at the superconducting gap is given by

$$\Delta_{1,i} = -v_i \eta \int d\varepsilon \frac{\Delta_{2,i}}{2\sqrt{\varepsilon^2 + \Delta_{2,i}^2}} \tag{B.1a}$$

$$\Delta_{2,i} = -v_i \int d\varepsilon \frac{\Delta_{1,i}}{2\sqrt{\varepsilon^2 + \Delta_{1,i}^2}} \tag{B.1b}$$

where $v_i = V\mathcal{N}_1$ is the dimensionless inter-band repulsion, and $\eta = \frac{\mathcal{N}_2}{\mathcal{N}_1}$ is the ratio between the density of states near the Fermi level of the two bands. The pseudospins are

$$S_{\alpha,i}^x = \frac{\Delta_{\alpha,i}}{2\sqrt{\varepsilon^2 + \Delta_{\alpha,i}^2}} \tag{B.2a}$$

$$S_{\alpha,i}^y = 0 \tag{B.2b}$$

$$S_{\alpha,i}^z = \frac{-\varepsilon}{2\sqrt{\varepsilon^2 + \Delta_{\alpha,i}^2}} \tag{B.2c}$$

After the interaction quench, the inter-band repulsion is suddenly changed to a different value, v_f. The interaction quench does not directly affect the electronic states, however,

changes their "velocities" (first order time derivatives). On the contrary, in optical pump-probe experiments, the pump pulse directly couples to the electronic states, while leaving the bare electron-electron interaction unchanged. The instantaneous electronic states right after the quench are still given by their equilibrium values (Eq. (B.2a)-(B.2c)), but their "velocities". The initial conditions of the post-quench dynamics of the superconducting gaps are giving by replacing the inter-band repulsion with its post-quench value v_f.

$$\Delta_1\left(0^+\right) = -v_f\eta\int d\varepsilon\frac{\Delta_{2,i}}{2\sqrt{\varepsilon^2+\Delta_{2,i}^2}} = \frac{v_f}{v_i}\Delta_{1,i} \tag{B.3a}$$

$$\Delta_2\left(0^+\right) = -v_f\int d\varepsilon\frac{\Delta_{1,i}}{2\sqrt{\varepsilon^2+\Delta_{1,i}^2}} = \frac{v_f}{v_i}\Delta_{2,i} \tag{B.3b}$$

According to the linearization, Eq. (4.13), the initial conditions of the deviations of the pseudospins relative to the asymptotic values are given by

$$f''_{\alpha,0} = 0 \tag{B.4a}$$

$$\dot{f}''_{\alpha,0} = -\frac{\varepsilon\left(\Delta_{\alpha,i}-\Delta_{\alpha,\infty}\right)}{\sqrt{\varepsilon^2+\Delta_{\alpha,i}^2}} - 2\delta_{\alpha,0}S^z_{\alpha,\infty} \tag{B.4b}$$

$f''_{\alpha,0}$ and $\dot{f}''_{\alpha,0}$ are related to the dynamics of the superconducting gap in Laplace space via $I_\alpha(s) = \left\langle \frac{2\varepsilon\left[sf'_{\alpha,0}+\dot{f}''_{\alpha,0}\right]}{s^2+4E^2_{\alpha,\infty}} \right\rangle$, which yields to Eq. (4.21).

B.2 Asymptotic analysis of the superconducting gap in Laplace space

In this appendix, we analyze the asymptotic behaviors of the gap in Laplace space near the branch points. From Eq. (4.38), there are 7 terms determine the analytic behavior of the gap. The branch point all come from the function $\Upsilon(\Delta, z)$, which opens branch cuts at at $(-i\infty,\ -i)$ and $(i,\ i\infty)$, as shown in Fig. B.1. Let $z = iy$, then, around

$y=1$, we have

$$\Upsilon\left(\Delta,y\right)\simeq\begin{cases}\frac{v_f\pi}{|\Delta|}\sqrt{\frac{1-y}{2}}+\mathcal{O}\left(1-y\right) & ,\ y\to1-\epsilon\\ i\frac{v_f\pi}{|\Delta|}\sqrt{\frac{y-1}{2}}+\mathcal{O}\left(y-1\right) & ,\ y\to1+\epsilon\end{cases}\tag{B.5}$$

where ϵ is an infinitesimal positive number.

We use the asymptotic behavior of $\Upsilon\left(\Delta,y\right)$ to expand all the terms in Eq. (4.38), and get the following results.

$$\mathrm{Im}\left[\frac{1}{D\left(y\right)}\right]\simeq\begin{cases}-\kappa^2\frac{\Upsilon\left(\tilde{\Delta}_{2,f},\kappa\right)+\frac{\kappa}{\eta}}{\Upsilon^2\left(\tilde{\Delta}_{2,f},\kappa\right)}\frac{v_f\pi}{|\tilde{\Delta}_{1,f}|}\sqrt{\frac{y-1}{2}} & ,\ y\to1+\epsilon\\ \frac{\eta}{\kappa}\mathrm{Im}\left[\frac{1}{\Upsilon\left(\tilde{\Delta}_{1,f},\frac{1}{\kappa}\right)}\right]-\left(\frac{\eta}{\kappa}\right)^2\mathrm{Im}\left[\frac{\Upsilon\left(\tilde{\Delta}_{1,f},\frac{1}{\kappa}\right)+\frac{1}{\kappa}}{\Upsilon^2\left(\tilde{\Delta}_{1,f},\frac{1}{\kappa}\right)}\right]\frac{v_f\pi}{|\tilde{\Delta}_{1,f}|}\sqrt{\frac{1-|\kappa|y}{2}} & ,\ y\to\frac{1}{|\kappa|}-\epsilon\\ \frac{\eta}{\kappa}\mathrm{Im}\left[\frac{1}{\Upsilon\left(\tilde{\Delta}_{1,f},\frac{1}{\kappa}\right)}\right]-\left(\frac{\eta}{\kappa}\right)^2\mathrm{Re}\left[\frac{\Upsilon\left(\tilde{\Delta}_{1,f},\frac{1}{\kappa}\right)+\frac{1}{\kappa}}{\Upsilon^2\left(\tilde{\Delta}_{1,f},\frac{1}{\kappa}\right)}\right]\frac{v_f\pi}{|\tilde{\Delta}_{1,f}|}\sqrt{\frac{|\kappa|y-1}{2}} & ,\ y\to\frac{1}{|\kappa|}+\epsilon\end{cases}\tag{B.6}$$

$$\mathrm{Im}\left[\frac{\Upsilon\left(\tilde{\Delta}_{1,f},y\right)}{D\left(y\right)}\right]\simeq\begin{cases}\kappa\frac{1}{\Upsilon\left(\tilde{\Delta}_{2,f},\kappa\right)}\frac{v_f\pi}{|\tilde{\Delta}_{1,f}|}\sqrt{\frac{y-1}{2}} & ,\ y\to1+\epsilon\\ -\left(\frac{\eta}{\kappa}\right)^2\frac{1}{\kappa}\mathrm{Im}\left[\frac{1}{\Upsilon\left(\tilde{\Delta}_{1,f},\frac{1}{\kappa}\right)}\right]\frac{v_f\pi}{|\tilde{\Delta}_{1,f}|}\sqrt{\frac{1-|\kappa|y}{2}} & ,\ y\to\frac{1}{|\kappa|}-\epsilon\\ -\left(\frac{\eta}{\kappa}\right)^2\left(1+\frac{1}{\kappa}\mathrm{Re}\left[\frac{1}{\Upsilon\left(\tilde{\Delta}_{1,f},\frac{1}{\kappa}\right)}\right]\right)\frac{v_f\pi}{|\tilde{\Delta}_{1,f}|}\sqrt{\frac{|\kappa|y-1}{2}} & ,\ y\to\frac{1}{|\kappa|}+\epsilon\end{cases}\tag{B.7}$$

$$\mathrm{Im}\left[\frac{\Upsilon\left(\tilde{\Delta}_{1,i},y\right)}{D\left(y\right)}\right]\simeq\begin{cases}\kappa\frac{1}{\Upsilon\left(\tilde{\Delta}_{2,f},\kappa\right)}\frac{v_f\pi}{|\tilde{\Delta}_{1,i}|}\sqrt{\frac{y-1}{2}} & ,\ y\to1+\epsilon\\ \frac{\eta}{\kappa}\mathrm{Im}\left[\frac{\Upsilon\left(\tilde{\Delta}_{1,i},\frac{1}{\kappa}\right)}{\Upsilon\left(\tilde{\Delta}_{1,f},\frac{1}{\kappa}\right)}\right]\\ -\left(\frac{\eta}{\kappa}\right)^2\mathrm{Im}\left[\frac{\Upsilon\left(\tilde{\Delta}_{1,i},\frac{1}{\kappa}\right)}{\Upsilon\left(\tilde{\Delta}_{1,f},\frac{1}{\kappa}\right)}+\frac{\frac{1}{\kappa}\Upsilon\left(\tilde{\Delta}_{1,i},\frac{1}{\kappa}\right)}{\Upsilon^2\left(\tilde{\Delta}_{1,f},\frac{1}{\kappa}\right)}\right]\frac{v_f\pi}{|\tilde{\Delta}_{1,f}|}\sqrt{\frac{1-|\kappa|y}{2}} & ,\ y\to\frac{1}{|\kappa|}-\epsilon\\ \frac{\eta}{\kappa}\mathrm{Im}\left[\frac{\Upsilon\left(\tilde{\Delta}_{1,i},\frac{1}{\kappa}\right)}{\Upsilon\left(\tilde{\Delta}_{1,f},\frac{1}{\kappa}\right)}\right]\\ -\left(\frac{\eta}{\kappa}\right)^2\mathrm{Re}\left[\frac{\Upsilon\left(\tilde{\Delta}_{1,i},\frac{1}{\kappa}\right)}{\Upsilon\left(\tilde{\Delta}_{1,f},\frac{1}{\kappa}\right)}+\frac{\frac{1}{\kappa}\Upsilon\left(\tilde{\Delta}_{1,i},\frac{1}{\kappa}\right)}{\Upsilon^2\left(\tilde{\Delta}_{1,f},\frac{1}{\kappa}\right)}\right]\frac{v_f\pi}{|\tilde{\Delta}_{1,f}|}\sqrt{\frac{|\kappa|y-1}{2}} & ,\ y\to\frac{1}{|\kappa|}+\epsilon\end{cases}\tag{B.8}$$

$$\mathrm{Im}\left[\frac{\Upsilon\left(\tilde{\Delta}_{2,f},\kappa y\right)}{D\left(y\right)}\right]\simeq\begin{cases}\Upsilon\left(\tilde{\Delta}_{2,f},\kappa\right)\mathrm{Im}\left[\frac{1}{D(y)}\right] & ,\ y\to1+\epsilon\\ \frac{\eta}{\kappa}\mathrm{Im}\left[\frac{1}{\Upsilon\left(\tilde{\Delta}_{1,f},\frac{1}{\kappa}\right)}\right]\frac{v_f\pi}{\left|\tilde{\Delta}_{1,f}\right|}\sqrt{\frac{1-|\kappa|y}{2}} & ,\ y\to\frac{1}{|\kappa|}-\epsilon\\ \frac{\eta}{\kappa}\mathrm{Re}\left[\frac{1}{\Upsilon\left(\tilde{\Delta}_{1,f},\frac{1}{\kappa}\right)}\right]\frac{v_f\pi}{\left|\tilde{\Delta}_{1,f}\right|}\sqrt{\frac{|\kappa|y-1}{2}} & ,\ y\to\frac{1}{|\kappa|}+\epsilon\end{cases}\tag{B.9}$$

$$\mathrm{Im}\left[\frac{\Upsilon\left(\tilde{\Delta}_{2,i},\kappa y\right)}{D\left(y\right)}\right]\simeq\begin{cases}\Upsilon\left(\tilde{\Delta}_{2,i},\kappa\right)\mathrm{Im}\left[\frac{1}{D(y)}\right] & ,\ y\to1+\epsilon\\ \frac{\eta}{\kappa}\mathrm{Im}\left[\frac{1}{\Upsilon\left(\tilde{\Delta}_{1,f},\frac{1}{\kappa}\right)}\right]\frac{v_f\pi}{\left|\tilde{\Delta}_{2,i}\right|}\sqrt{\frac{1-|\kappa|y}{2}} & ,\ y\to\frac{1}{|\kappa|}-\epsilon\\ \frac{\eta}{\kappa}\mathrm{Re}\left[\frac{1}{\Upsilon\left(\tilde{\Delta}_{1,f},\frac{1}{\kappa}\right)}\right]\frac{v_f\pi}{\left|\tilde{\Delta}_{2,i}\right|}\sqrt{\frac{|\kappa|y-1}{2}} & ,\ y\to\frac{1}{|\kappa|}+\epsilon\end{cases}\tag{B.10}$$

$$\mathrm{Im}\left[\frac{\Upsilon\left(\tilde{\Delta}_{1,f},y\right)\Upsilon\left(\tilde{\Delta}_{2,i},\kappa y\right)}{D\left(y\right)}\right]\simeq\begin{cases}\kappa\frac{\Upsilon\left(\tilde{\Delta}_{2,i},\kappa\right)}{\Upsilon\left(\tilde{\Delta}_{2,f},\kappa\right)}\frac{v_f\pi}{\left|\tilde{\Delta}_{1,f}\right|}\sqrt{\frac{y-1}{2}} & ,\ y\to1+\epsilon\\ \mathcal{O}\left(\epsilon\right) & ,\ y\to\frac{1}{|\kappa|}-\epsilon\\ \frac{\eta}{\kappa}\frac{v_f\pi}{\left|\tilde{\Delta}_{2,i}\right|}\sqrt{\frac{|\kappa|y-1}{2}} & ,\ y\to\frac{1}{|\kappa|}+\epsilon\end{cases}\tag{B.11}$$

$$\mathrm{Im}\left[\frac{\Upsilon\left(\tilde{\Delta}_{2,f},\kappa y\right)\Upsilon\left(\tilde{\Delta}_{1,i},y\right)}{D\left(y\right)}\right]\simeq\begin{cases}\kappa\frac{v_f\pi}{\left|\tilde{\Delta}_{1,i}\right|}\sqrt{\frac{y-1}{2}} & ,\ y\to1+\epsilon\\ \frac{\eta}{\kappa}\mathrm{Im}\left[\frac{\Upsilon\left(\tilde{\Delta}_{1,i},\frac{1}{\kappa}\right)}{\Upsilon\left(\tilde{\Delta}_{1,f},\frac{1}{\kappa}\right)}\right]\frac{v_f\pi}{\left|\tilde{\Delta}_{1,f}\right|}\sqrt{\frac{1-|\kappa|y}{2}} & ,\ y\to\frac{1}{|\kappa|}-\epsilon\\ \frac{\eta}{\kappa}\mathrm{Re}\left[\frac{\Upsilon\left(\tilde{\Delta}_{1,i},\frac{1}{\kappa}\right)}{\Upsilon\left(\tilde{\Delta}_{1,f},\frac{1}{\kappa}\right)}\right]\frac{v_f\pi}{\left|\tilde{\Delta}_{1,f}\right|}\sqrt{\frac{|\kappa|y-1}{2}} & ,\ y\to\frac{1}{|\kappa|}+\epsilon\end{cases}\tag{B.12}$$

B.3 Inverse Laplace transform and useful integrals

The inverse-Laplace transform is given by the Bromwich integral:

$$y\left(t\right)=\mathcal{L}^{-1}\left\{Y\right\}\left(t\right)=\frac{1}{2\pi i}\int_{\sigma-i\infty}^{\sigma+i\infty}Y\left(s\right)e^{st}ds\tag{B.13}$$

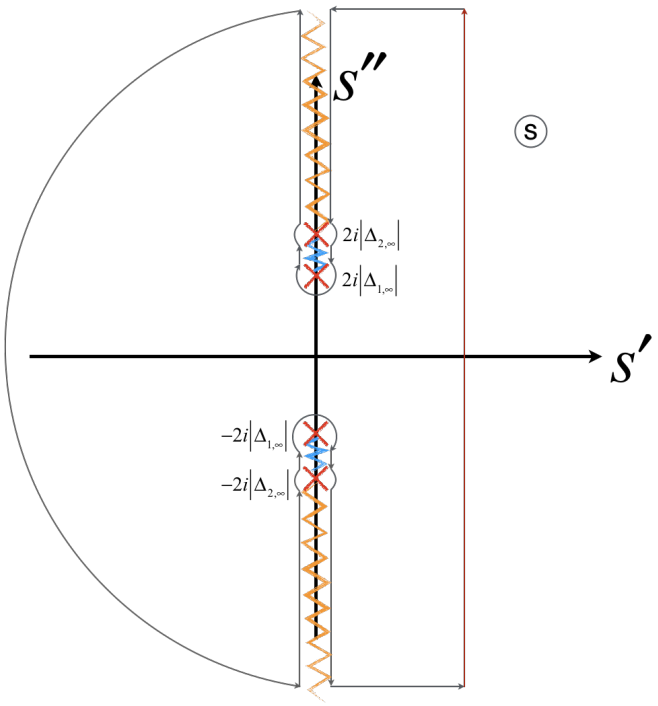

Figure B.1: Integration contour in the complex Laplace space

where σ is a real number that is larger than the real parts of all the singularities of $Y(s)$.

All the asymptotic behaviors of the gap in Laplace space are square root like. Consequently, transforming back to real time domain leads to a $t^{-3/2}$ decay.

$$\begin{aligned}\int_1^\infty \frac{\sqrt{y-1}}{y}\cos\left(2\Delta_{1,\infty}yt\right)dy &= \sqrt{\frac{\pi}{4\Delta_{1,\infty}t}}\left[\cos\left(2\Delta_{1,\infty}t\right)-\sin\left(2\Delta_{1,\infty}t\right)\right] \\ &\quad +\pi\left[C\left(\sqrt{\frac{4\Delta_{1,\infty}t}{\pi}}\right)+S\left(\sqrt{\frac{4\Delta_{1,\infty}t}{\pi}}\right)-1\right] \\ &\simeq -\frac{\sqrt{\pi}\sin\left(2\Delta_{1,\infty}t+\frac{\pi}{4}\right)}{2\left(2\Delta_{1,\infty}t\right)^{3/2}} \end{aligned} \tag{B.14}$$

for $2\Delta_{1,\infty}t \gg 1$. Similarly, $\int_{\frac{1}{|\kappa|}}^{\infty} \frac{\sqrt{|\kappa|y-1}}{y} \cos\left(2\Delta_{1,\infty}yt\right) dy \simeq -\frac{\sqrt{\pi}\sin\left(2|\Delta_{2,\infty}|t+\frac{\pi}{4}\right)}{2(2|\Delta_{2,\infty}|t)^{3/2}}$, and

$$\begin{aligned}\int_{-\infty}^{\frac{1}{|\kappa|}} \frac{\sqrt{1-|\kappa|\,y}}{y} \cos\left(2\Delta_{1,\infty}yt\right) dy &\simeq \lim_{\Lambda\to\infty} \int_0^{\Lambda} \sqrt{x} \cos\left(2\,|\Delta_{2,\infty}|\,t - 2\,|\Delta_{2,\infty}|\,xt\right) \\ &\simeq \frac{\sqrt{\pi}\sin\left(2\,|\Delta_{2,\infty}|\,t-\frac{\pi}{4}\right)}{2\left(2\,|\Delta_{2,\infty}|\,t\right)^{3/2}} \end{aligned} \tag{B.15}$$

B.4 analytic expressions for the gap oscillation for weak quenches

We wrote the long-time asymptotic expressions of the gap oscillations for relatively weak quenches in Eq. (4.41a) and (4.41b). In this appendix, we provide the expressions for the prefactors $\mathcal{A}_\alpha$, $\mathcal{B}_\alpha$ and $\mathcal{C}_\alpha$ of the two equations.

$$\begin{aligned}\frac{\mathcal{A}_1}{\Delta_{1,\infty}} &= -\frac{\sqrt{\pi}}{4}\left\{\left[\frac{\kappa}{\eta}\left[\frac{v_f}{v_i}\left(\frac{\tilde{\Delta}_{1,i}}{\tilde{\Delta}_{2,i}}+\frac{\tilde{\Delta}_{2,i}}{\tilde{\Delta}_{1,i}}\right)-2\right]+\left(\frac{v_f}{v_i}\frac{\tilde{\Delta}_{2,i}}{\tilde{\Delta}_{1,i}}-1\right)\Upsilon\left(\tilde{\Delta}_{2,f},\kappa\right)\right.\right. \\ &\quad \left.\left.-\left(\tilde{\Delta}_{2,i}-1\right)\Upsilon\left(\tilde{\Delta}_{2,i},\kappa\right)\right]\times\frac{\Upsilon\left(\tilde{\Delta}_{2,f},\kappa\right)+\frac{\kappa}{\eta}}{\Upsilon^2\left(\tilde{\Delta}_{2,f},\kappa\right)}\frac{\kappa v_f}{\left|\tilde{\Delta}_{2,f}\right|}\right. \\ &\quad \left.+\left(1+\frac{\kappa}{\eta}\frac{1}{\Upsilon\left(\tilde{\Delta}_{2,f},\kappa\right)}\right)\left(\tilde{\Delta}_{1,i}-1\right)\frac{\kappa v_f}{\left|\tilde{\Delta}_{1,i}\right|}\right\}\end{aligned} \tag{B.16}$$

$$\begin{aligned}\frac{\mathcal{B}_1}{\Delta_{1,\infty}} &= \frac{\sqrt{\pi}}{4}\left\{\left(\frac{v_f}{v_i}\frac{\Delta_{1,i}}{\Delta_{2,i}}-1+\tilde{\Delta}_{2,f}-\frac{\tilde{\Delta}_{2,f}}{\tilde{\Delta}_{2,i}}\right)\mathrm{Im}\left[\frac{1}{\Upsilon\left(\tilde{\Delta}_{1,f},\frac{1}{\kappa}\right)}\right]\right. \\ &\quad +\left[\frac{v_f}{v_i}\left(\frac{\tilde{\Delta}_{1,i}}{\tilde{\Delta}_{2,i}}+\frac{\tilde{\Delta}_{2,i}}{\tilde{\Delta}_{1,i}}\right)-2\right]\frac{1}{\kappa}\mathrm{Im}\left[\frac{1}{\Upsilon^2\left(\tilde{\Delta}_{1,f},\frac{1}{\kappa}\right)}\right] \\ &\quad \left.-\left(\tilde{\Delta}_{1,i}-1\right)\mathrm{Im}\left[\frac{\Upsilon\left(\tilde{\Delta}_{1,i},\frac{1}{\kappa}\right)}{\Upsilon^2\left(\tilde{\Delta}_{1,f},\frac{1}{\kappa}\right)}\right]\right\}\frac{\eta}{\kappa^2}\frac{v_f}{\left|\tilde{\Delta}_{2,f}\right|}\end{aligned} \tag{B.17}$$

$$\frac{\mathcal{C}_1}{\Delta_{1,\infty}} = -\frac{\sqrt{\pi}}{4}\left\{\left(\frac{v_f}{v_i}\frac{\Delta_{1,i}}{\Delta_{2,i}} - 1 + \tilde{\Delta}_{1,f} - \frac{\tilde{\Delta}_{1,f}}{\tilde{\Delta}_{2,i}}\right)\mathrm{Re}\left[\frac{1}{\Upsilon\left(\tilde{\Delta}_{1,f},\frac{1}{\kappa}\right)}\right] + \left[\frac{v_f}{v_i}\left(\frac{\tilde{\Delta}_{1,i}}{\tilde{\Delta}_{2,i}} + \frac{\tilde{\Delta}_{2,i}}{\tilde{\Delta}_{1,i}}\right) - 2\right]\frac{1}{\kappa}\mathrm{Re}\left[\frac{1}{\Upsilon^2\left(\tilde{\Delta}_{1,f},\frac{1}{\kappa}\right)}\right] - \left(\tilde{\Delta}_{1,i} - 1\right)\mathrm{Re}\left[\frac{\Upsilon\left(\tilde{\Delta}_{1,i},\frac{1}{\kappa}\right)}{\Upsilon^2\left(\tilde{\Delta}_{1,f},\frac{1}{\kappa}\right)}\right]\right\}\frac{\eta}{\kappa^2}\frac{v_f}{\left|\tilde{\Delta}_{2,f}\right|} \tag{B.18}$$

$$\frac{\mathcal{A}_2}{\Delta_{2,\infty}} = -\frac{\sqrt{\pi}}{4}\left\{\left(\frac{v_f}{v_i}\frac{\Delta_{1,i}}{\Delta_{2,i}} - 1 + \tilde{\Delta}_{1,f} - \frac{\tilde{\Delta}_{1,f}}{\tilde{\Delta}_{1,i}}\right)\frac{1}{\Upsilon\left(\tilde{\Delta}_{2,f},\kappa\right)} + \frac{\kappa}{\eta}\left[\frac{v_f}{v_i}\left(\frac{\tilde{\Delta}_{1,i}}{\tilde{\Delta}_{2,i}} + \frac{\tilde{\Delta}_{2,i}}{\tilde{\Delta}_{1,i}}\right) - 2\right]\frac{1}{\Upsilon^2\left(\tilde{\Delta}_{2,f},\kappa\right)} - \left(\tilde{\Delta}_{2,i} - 1\right)\frac{\Upsilon\left(\tilde{\Delta}_{2,i},\kappa\right)}{\Upsilon^2\left(\tilde{\Delta}_{2,f},\kappa\right)}\right\}\frac{\kappa^2}{\eta}\frac{v_f}{\left|\tilde{\Delta}_{1,f}\right|} \tag{B.19}$$

$$\frac{\mathcal{B}_2}{\Delta_{2,\infty}} = \frac{\sqrt{\pi}}{4}\left\{\left[\frac{v_f}{v_i}\left(2\frac{\tilde{\Delta}_{1,i}}{\tilde{\Delta}_{2,i}} + \frac{\tilde{\Delta}_{2,i}}{\tilde{\Delta}_{1,i}}\right) - 3 + \tilde{\Delta}_{2,f} - \frac{\tilde{\Delta}_{2,f}}{\tilde{\Delta}_{2,i}}\right]\mathrm{Im}\left[\frac{1}{\Upsilon\left(\tilde{\Delta}_{1,f},\frac{1}{\kappa}\right)}\right] + \left[\frac{v_f}{v_i}\left(\frac{\tilde{\Delta}_{1,i}}{\tilde{\Delta}_{2,i}} + \frac{\tilde{\Delta}_{2,i}}{\tilde{\Delta}_{1,i}}\right) - 2\right]\frac{1}{\kappa}\mathrm{Im}\left[\frac{1}{\Upsilon^2\left(\tilde{\Delta}_{1,f},\frac{1}{\kappa}\right)}\right] - \left(\tilde{\Delta}_{1,i} - 1\right)\times \times\left(\kappa\mathrm{Im}\left[\frac{\Upsilon\left(\tilde{\Delta}_{1,i},\frac{1}{\kappa}\right)}{\Upsilon\left(\tilde{\Delta}_{1,f},\frac{1}{\kappa}\right)}\right] + \mathrm{Im}\left[\frac{\Upsilon\left(\tilde{\Delta}_{1,i},\frac{1}{\kappa}\right)}{\Upsilon^2\left(\tilde{\Delta}_{1,f},\frac{1}{\kappa}\right)}\right]\right)\right\}\frac{\eta}{\kappa^2}\frac{v_f}{\left|\tilde{\Delta}_{2,f}\right|} \tag{B.20}$$

$$\begin{aligned}\frac{\mathcal{C}_2}{\Delta_{2,\infty}} &= -\frac{\sqrt{\pi}}{4}\left\{\left[\frac{v_f}{v_i}\left(\frac{\tilde{\Delta}_{1,i}}{\tilde{\Delta}_{2,i}}+\frac{\tilde{\Delta}_{2,i}}{\tilde{\Delta}_{1,i}}\right)-2\right]\mathrm{Re}\left[\frac{\Upsilon\left(\tilde{\Delta}_{1,f},\frac{1}{\kappa}\right)+\frac{1}{\kappa}}{\Upsilon^2\left(\tilde{\Delta}_{1,f},\frac{1}{\kappa}\right)}\right]\right.\\ &+\left[\frac{v_f}{v_i}\left(\frac{\tilde{\Delta}_{1,i}}{\tilde{\Delta}_{2,i}}+\frac{\tilde{\Delta}_{2,i}}{\tilde{\Delta}_{1,i}}\right)-2+\tilde{\Delta}_{2,f}-\frac{\tilde{\Delta}_{2,f}}{\tilde{\Delta}_{2,i}}\right]\left(\kappa+\mathrm{Re}\left[\frac{1}{\Upsilon\left(\tilde{\Delta}_{1,f},\frac{1}{\kappa}\right)}\right]\right)\\ &\left.-\left(\tilde{\Delta}_{1,i}-1\right)\mathrm{Re}\left[\frac{\kappa\Upsilon\left(\tilde{\Delta}_{1,i},\frac{1}{\kappa}\right)}{\Upsilon\left(\tilde{\Delta}_{1,f},\frac{1}{\kappa}\right)}+\frac{\Upsilon\left(\tilde{\Delta}_{1,i},\frac{1}{\kappa}\right)}{\Upsilon^2\left(\tilde{\Delta}_{1,f},\frac{1}{\kappa}\right)}\right]\right\}\frac{\eta}{\kappa^2}\frac{v_f}{\left|\tilde{\Delta}_{2,f}\right|} \qquad \text{(B.21)}\end{aligned}$$

With these prefactors, we compare our analytic asymptotic behaviors of the gap oscillations with the numerical calculation (see Fig. 4.5).

Appendix C

Technical Details for Chapter 5

C.1 Experimental details

The schematic experimental setup is shown in Fig. C.1. The Ti-sapphire laser with 3 mJ pulse energy, 40 fs pulse duration, 1KHz repetition rate and 800 nm center wavelength is split into three optical paths for the purposes of pumping, probing and sampling, respectively. The terahertz (THz) pump pulse has a larger intensity, which is generated by tilted-pulse-front phase matching through 1.3% MgO doped $LiNbO_3$ crystal. In contrast, the THz probe pulse, generated by optical rectification through 1 mm thick (110)-ZnTe crystal, has a smaller intensity. The pump and probe pulses are at orthogonal polarizations. They focus on the sample at normal incidence and the focal sizes are 1.2 mm and 0.8 mm for the pump and the probe beam, respectively. After the sample, the transmitted pump beam is blocked by a wire grid polarizer while the transmitted probe E-field is measured by the electro-optic sampling. The transmitted E-field signal is integrated by a Boxcar integrator and sent to the DAQ board together with the on-off signal from two synchronized choppers. Further details can be found in Ref. [105], where the same experimental setup and data analysis method were used. Comparing with previous THz-pump-probe experiment on NbN thin film (e.g. Ref. [94]), the peak E-field of narrow band 1THz pump can reach values as high as 109 kV/cm.

The ultrafast dynamics of the superconducting gap $\Delta(t_{pp})$ is tracked by fixing t_{gate}

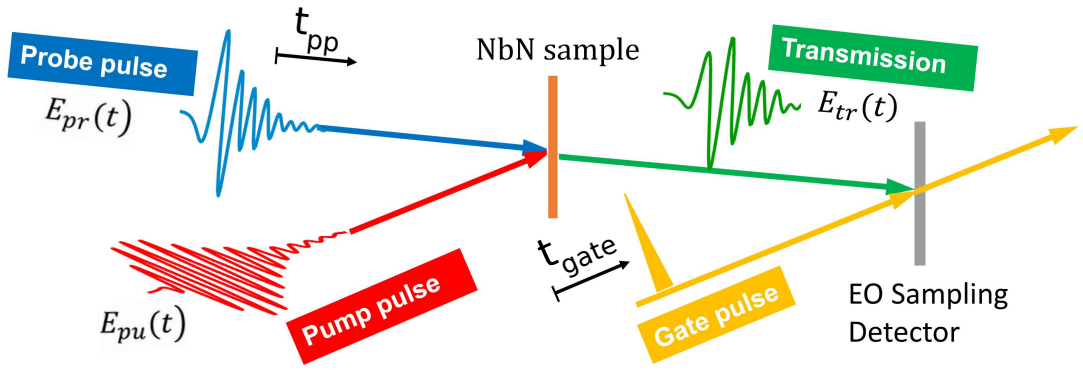

Figure C.1: Schematic of THz-pump-THz-probe measurement. $E_{\mathrm{pu}}(t)$, $E_{\mathrm{pr}}(t)$ and $E_{\mathrm{tr}}(t)$ are the time domain E-fields of the pump beam, the probe beam and the transmitted probe beam, respectively. t_{gate} is the relative time delay between the probe and the gate pulse. t_{pp} is the delay time between the pump and the probe.

at the peak of the pump-induced change of the transmitted probe electric field,

$$\Delta E(t_{pp}) = E(\text{pump on}, t_{pp}, 4\text{ K}) - E(\text{off}, 4\text{ K})\,, \tag{C.1}$$

and scanning the delay time t_{pp} between pump and probe. Here, $E(\text{pump on}, t_{pp}, 4\text{ K})$ corresponds to the transmitted probe electric field amplitude at fixed t_{gate} and variable t_{pp} for a system that was initially prepared at $T = 4$ K before it was exposed to the pump pulse. We note that our choice of t_{gate} corresponds to setting t_{gate} to the position of maximal contrast of the transmitted probe field signal with and without pump. As demonstrated in Refs. [103, 92, 94, 105], the pump-probe signal $\Delta E/E$, where $E \equiv E(\text{off}, 4\text{ K})$, faithfully reflects the transient behavior of superconducting order parameter Δ. In other words, it holds that

$$\frac{\Delta E(t_{pp})}{E(\text{off}, T = 4\text{ K})} = \alpha\Big(1 - \frac{\Delta(t_{pp})}{\Delta(T = 4\text{K})}\Big) \tag{C.2}$$

with approximately temperature-independent proportionality factor α.

We obtain the proportionality constant $\alpha_{\mathrm{NbN}} = 2.7$ for NbN as follows. We independently determine the gap Δ at $t_{pp} = 10$ ps from the optical conductivity $\sigma(t_{pp})$ shown in Fig. 5.1(a, b). We extract the gap $\Delta(t_{pp} = 10\text{ ps}) = 3.9/2 = 1.95$ meV from a

fit of $\sigma_2(t_{pp})$ using the expressions in Ref. [129] derived for a BCS model with general scattering time τ in equilibrium. We first find the scattering rate $\tau_{\mathrm{NbN}}^{-1} = 72.8$ meV from fitting the equilibrium conductivity $\sigma(T = 15\ \mathrm{K})$ in the normal state to the same model. Comparing the value of $\Delta E/E = 0.41$ and $\Delta(t_{pp})/\Delta(4\mathrm{K}) = 3.9/4.6 = 0.85$, we find $\alpha_{\mathrm{NbN}} = 2.7$.

For Nb_3Sn, we find the proportionality constant $\alpha_{\mathrm{Nb_3Sn}} = -0.75$ by first relating the change of the probe field transmission to the change of the gap in equilibrium [103, 92, 94]:

$$\frac{E(T) - E(T_0)}{E(T_0)} = \alpha\Big(1 - \frac{\Delta(T)}{\Delta(T_0)}\Big) \tag{C.3}$$

with $T_0 = 4$ K. We find $E(4\mathrm{K}) = -0.13$ and $E(18\mathrm{K}) = -0.03$, which together with $\Delta(4\mathrm{K}) = 5.1$ meV and $\Delta(18\mathrm{K}) = 0$, yields $\alpha_{\mathrm{Nb_3Sn}} = -0.75$. We assume that the same relation also holds in non-equilibrium, as was shown explicitly for optical pulses [103].

C.2 Pseudospin formalism and non-equilibrium dynamics

We start from the BCS Hamiltonian for superconductivity, which is written as Eq. (1) in the main text:

$$H_{\mathrm{BCS}} = \sum_{\boldsymbol{k},\sigma} \xi_{\boldsymbol{k}+e\boldsymbol{A}} c^\dagger_{\boldsymbol{k},\sigma} c_{\boldsymbol{k},\sigma} + \sum_{\boldsymbol{k}} \big(\Delta c^\dagger_{\boldsymbol{k},\uparrow} c^\dagger_{-\boldsymbol{k},\downarrow} + \mathrm{h.c.}\big) + \frac{|\Delta|^2}{V_0} \tag{C.4}$$

where $\xi_{\boldsymbol{k}} = \varepsilon_{\boldsymbol{k}} - \mu$ is the electronic dispersion near the Fermi level, e is the charge of the electron, which couples to an external electromagnetic field $\boldsymbol{A}$, and $V_0 > 0$ denotes the attractive superconducting interaction. The superconducting gap, Δ, is determined self-consistently via the gap equation:

$$\Delta = -V_0 \sum_{\boldsymbol{k}} \langle c_{-\boldsymbol{k},\downarrow} c_{\boldsymbol{k},\uparrow} \rangle \tag{C.5}$$

In general, $\Delta = \Delta' + i\Delta''$ is a complex number, with Δ' and Δ'' being the real and imaginary part of the gap respectively. The phase is purely a gauge choice. Therefore, in equilibrium, the superconducting gap is usually chosen to be real for convenience.

In the presence of parity symmetry (i.e. $\xi_{\boldsymbol{k}} = \xi_{-\boldsymbol{k}}$ and $n_{\boldsymbol{k}} = n_{-\boldsymbol{k}}$), and using the

pseudospin representation introduced by Anderson [75]

$$\begin{aligned} S^-_{\boldsymbol{k}} &= c_{-\boldsymbol{k},\downarrow} c_{\boldsymbol{k},\uparrow} \\ S^+_{\boldsymbol{k}} &= c^\dagger_{\boldsymbol{k},\uparrow} c^\dagger_{-\boldsymbol{k},\downarrow} \\ S^z_{\boldsymbol{k}} &= n_{\boldsymbol{k}} - \frac{1}{2} \end{aligned} \tag{C.6}$$

with $n_{\boldsymbol{k}} = \frac{1}{2}\left(c^\dagger_{\boldsymbol{k},\uparrow} c_{\boldsymbol{k},\uparrow} + c^\dagger_{\boldsymbol{k},\downarrow} c_{\boldsymbol{k},\downarrow}\right)$, the BCS Hamiltonian can be written as

$$H_{\mathrm{BCS}} = -\sum_{\boldsymbol{k}} \boldsymbol{B}_{\boldsymbol{k}} \cdot \boldsymbol{S}_{\boldsymbol{k}} + \frac{|\Delta|^2}{V_0} + \sum_{\boldsymbol{k}} \bar{\xi}_{\boldsymbol{k},\boldsymbol{A}}\,. \tag{C.7}$$

The gap is self-consistently determined by a collective pseudospin coordinate

$$\Delta = -V_0 \sum_{\boldsymbol{k}} \langle S^-_{\boldsymbol{k}} \rangle \tag{C.8}$$

The pseudo-magnetic field is given by $\boldsymbol{B}_{\boldsymbol{k}} = (-2\Delta', 2\Delta'', -\xi_{\boldsymbol{k}+e\boldsymbol{A}} - \xi_{\boldsymbol{k}-e\boldsymbol{A}})$. In equilibrium ($\boldsymbol{A} = 0$), the pseudospins perfectly align with the pseudo-magnetic field. Consequently, the expectation values of the pseudospins have the following configuration at $T = 0$:

$$\langle \boldsymbol{S}_{\boldsymbol{k}} \rangle_{T=0} = \tfrac{1}{2} \frac{\boldsymbol{B}_{\boldsymbol{k}}}{|\boldsymbol{B}_{\boldsymbol{k}}|} \tag{C.9}$$

We assume this to be the initial state before the THz pump pulse. In equilibrium at finite temperature T, the length of the pseudospins is reduced, but they still point along the pseudo-magnetic field

$$\begin{aligned} \langle S^x_{\boldsymbol{k}} \rangle_T &= \frac{-\Delta'}{2E_{\boldsymbol{k}}} \tanh\left(\frac{E_{\boldsymbol{k}}}{2T}\right) \\ \langle S^y_{\boldsymbol{k}} \rangle_T &= \frac{\Delta''}{2E_{\boldsymbol{k}}} \tanh\left(\frac{E_{\boldsymbol{k}}}{2T}\right) \\ \langle S^z_{\boldsymbol{k}} \rangle_T &= -\frac{\xi_{\boldsymbol{k}}}{2E_{\boldsymbol{k}}} \tanh\left(\frac{E_{\boldsymbol{k}}}{2T}\right) \end{aligned} \tag{C.10}$$

where $E_{\boldsymbol{k}}(T) = \sqrt{\xi_{\boldsymbol{k}}^2 + |\Delta(T)|^2}$ is the quasi-particle dispersion, and the finite temperature gap $\Delta(T) = \Delta' + i\Delta''$ is determined by the gap equation

$$1 = V_0 \sum_{\boldsymbol{k}} \frac{\tanh[E_{\boldsymbol{k}}/(2T)]}{2E_{\boldsymbol{k}}} \,. \tag{C.11}$$

The pseudospin formalism of the BCS model is particularly convenient for the study of non-equilibrium dynamics of the superconducting gap, since the pseudospin dynamics is described by the precession under the pseudo magnetic field:

$$\frac{d}{dt}\boldsymbol{S}_{\boldsymbol{k}} = i\,[H_{\rm BCS}, \boldsymbol{S}_{\boldsymbol{k}}] = \boldsymbol{S}_{\boldsymbol{k}} \times \boldsymbol{B}_{\boldsymbol{k}} \tag{C.12}$$

The complexity, however, is encoded in the self-consistency condition of the pseudo-magnetic field. Since the superconducting gap depends on the pseudospin configuration in $\boldsymbol{k}$-space, the pseudo-magnetic field will also change over time.

The quench dynamics of the superconducting gap has been thoroughly studied under the BCS framework using a topological classification of the spectral polynomial[27, 23, 100]. Recently, such classification has also been applied to the gap dynamics in THz-pump-probe experiments[126].

Once the system is driven out of equilibrium, the internal energy of the electronic system increases. One can calculate the superconducting gap $\Delta_* = |\Delta_*|\, e^{i\phi}$ at the effective temperature T_* corresponding to the internal energy at a given time, which uniquely determines the thermalized pseudospin configuration $\langle \boldsymbol{S}^*_{\boldsymbol{k}} \rangle = \frac{1}{2}\hat{\boldsymbol{s}}^*_{\parallel,\boldsymbol{k}} \tanh\big(\frac{\sqrt{\xi_{\boldsymbol{k}}^2+|\Delta_*|^2}}{2T^*(t)}\big)$, where

$$\hat{\boldsymbol{s}}^*_{\parallel,\boldsymbol{k}} = \left(\frac{-\,|\Delta_*|\cos\phi}{\sqrt{\xi_{\boldsymbol{k}}^2 + |\Delta_*|^2}}, \frac{|\Delta_*|\sin\phi}{\sqrt{\xi_{\boldsymbol{k}}^2 + |\Delta_*|^2}}, \frac{-\xi_{\boldsymbol{k}}}{\sqrt{\xi_{\boldsymbol{k}}^2 + |\Delta_*|^2}} \right) , \tag{C.13}$$

where $\Delta = \Delta' + i\Delta'' = |\Delta| e^{i\phi}$. Note that since the internal energy is changing over time, $\langle \boldsymbol{S}^*_{\boldsymbol{k}} \rangle$ and $\hat{\boldsymbol{s}}^*_{\parallel,\boldsymbol{k}}$ are also time dependent and generally not aligned with the pseudo-magnetic field $\boldsymbol{B}_{\boldsymbol{k}}$. Without damping, the pseudospin will simply precess around the self-consistent pseudo-magnetic field, which itself is also oscillating. Once damping is incorporated, the pseudo-spins tend to relax towards the thermalized configuration $\langle \boldsymbol{S}^*_{\boldsymbol{k}} \rangle$, which is described by Eq. (5.9) in the main text.